

# Initiation of Fault Reactivation

New Insights into the Effect of Differential Compaction

Irene M. Platteeuw

Delft University of Technology



# Initiation of Fault Reactivation

New Insights into the Effect of Differential  
Compaction

by

Irene M. Platteeuw

to obtain the degree of Master of Science in Applied Earth Sciences,  
specialized in Petroleum Engineering and Geoscience  
at the Delft University of Technology,  
to be defended publicly on Wednesday January 31st 2018 at 03:00 PM.

Student number: 4210956  
Project duration: March 13, 2017 – January 31, 2018  
Thesis committee: Dr. ir. F. C. Vossepoel, TU Delft, chair  
Prof. Dr. G. Bertotti, TU Delft  
Dr. ir. R. Brinkgreve, TU Delft  
Dr. M. Hetteema, EBN B.V.  
G. Hoetz, EBN B.V.

An electronic, non-confidential version of the thesis is available at <http://repository.tudelft.nl/>.



"A good decision is based on knowledge,  
not on numbers."

- *Plato*



# Abstract

The production and injection of fluids from and in reservoirs leads to changes in the in-situ stress in the subsurface. This can cause reservoir compaction, subsidence, fault reactivation and / or seismicity. As these effects may greatly influence society it is of importance to find accurate methods to describe them so they can be predicted or even better, mitigated.

This thesis discusses a new analytical approach to calculate stress in the subsurface which incorporates the effects of differential compaction on the initiation of fault reactivation. This new approach is named *Differential Compaction Loading* (DCL) and the reason for its development is due to discrepancies observed between calculations using the *Mohr-Coulomb* failure criterion, also known as *Poro-elastic Loading* (PEL), and field observations.

Geomechanical modelling was performed to assess fault failure sensitivity to a range of geometrical aspects as well as reservoir and fault properties. From this analysis, focusing on the reactivation pressure at which failure first occurs, an empirical sense of sensitivity was established. It was found that for the examined variations in the geometry the fault dip angle resulted in the largest spread in reactivation pressure. For the examined reservoir and fault properties, the friction angle was found to have the largest sensitivity.

With these results it was possible to improve the estimates of essential parameters within the analytical approach, yielding a better fit between analytical and modelled solutions. These solutions lie closer to field observations. Hence, the new method of DCL shows a great improvement in calculation of stresses in the subsurface, compared to the method of PEL. This calibrated analytical approach allows for a quick assessment of the fault stability within a reservoir. Additionally, through the results from the geomechanical model new insights were obtained into the way stresses change and behave when a reservoir is depleted. The rotation of the principal stresses for each level of depletion was quantified and a new definition of the critical fault angle, the dip angle which will fail first, was derived. This links the depletion pressure and related rotation angle directly to a value of the new critical fault angle when DCL is present.

Ultimately, these new insights into fault failure behaviour of boundary faults could be a useful tool in the step towards prediction and mitigation of production or injection related seismicity.



# Acknowledgements

I would like to start with thanking Plaxis and its people for the licence to their software, their support and help with problems I encountered. I greatly appreciate their flexibility on letting me use the software outside of university.

Secondly, I would like to thank EBN for the opportunity of a graduation internship which allowed me to take a look into the company. Most important was the support of the exceptionally bright geomechanical expert and my daily supervisor Dr. Marc Hettema. Besides this, the input from other employees on ideas and results alike helped me a great deal in the development of my work. And not to forget the great facilities, amazing colleagues and good coffee which at times could be more motivation than anything else.

Next, I would like to thank my supervisors from the TU Delft. To mention here is Prof. Giovanni Bertotti who pushed me to think about what exactly I was actually doing and who forced me to really grasp the fundamental aspects of the problem. However, I would especially like to extend my gratitude to Dr. Femke Vossepoel who was there for me every step of the way. One could not wish for a better supervisor, always 110% engaged on both professional as well as personal aspects.

Last but not least many thanks go out to my family and friends on whom I could always fall back in the case things became too turbulent.

I look back on a very pleasant and successful final 10 months of my education.



# Contents

<b>List of Figures</b>	<b>xi</b>
<b>List of Tables</b>	<b>xiii</b>
<b>1 Introduction</b>	<b>1</b>
<b>2 Theory of Geomechanics</b>	<b>5</b>
2.1 Stress and Strain . . . . .	5
2.2 Elastic Moduli. . . . .	7
2.3 Poro-elasticity. . . . .	8
2.4 Initial stress regimes and stresses during depletion . . . . .	8
2.5 Stress and strain on a 2D fault plane . . . . .	10
2.5.1 Differential compaction in producing reservoirs . . . . .	12
2.5.2 Compaction, Subsidence and Vertical Displacement. . . . .	13
2.5.3 Initiation of fault reactivation: The failure criterion and failure reservoir pressure . . . . .	15
<b>3 Geological Background of the Netherlands</b>	<b>17</b>
3.1 Tectonic setting and paleogeographical development. . . . .	17
3.2 Lithologies . . . . .	20
3.2.1 Underburden . . . . .	20
3.2.2 Reservoir. . . . .	21
3.2.3 Overburden . . . . .	21
<b>4 Geomechanical Model</b>	<b>25</b>
4.1 Software - Plaxis 2D 2017 . . . . .	25
4.2 Geometry - Reservoir setting . . . . .	26
4.3 Input Data - Geomechanical, Strength Parameters . . . . .	28
4.4 Boundary conditions, meshing & model validation . . . . .	30
4.5 Execution of the Simulations . . . . .	30
4.6 Uncertainty . . . . .	31
<b>5 Analysis and Interpretation of Fault Failure Behaviour</b>	<b>33</b>
5.1 The depleting reservoir . . . . .	33
5.2 Simulations . . . . .	38
5.2.1 Effect of reservoir radius . . . . .	38
5.2.2 Effect of reservoir thickness . . . . .	38
5.2.3 Effect of fault throw . . . . .	39
5.2.4 Effect of fault angle. . . . .	40
5.2.5 Fault failure sensitivity and the combining of information from various rock and fault properties . . . . .	44
5.3 Comparing of analytical approach and simulations. . . . .	47
5.3.1 Determination of the influence zone. . . . .	47
5.3.2 Tuning of the analytical approach . . . . .	48
5.3.3 Reactivation pressure . . . . .	49
5.3.4 Critical fault angle for reactivation . . . . .	50
5.4 Uncertainty . . . . .	52
<b>6 Conclusions &amp; Recommendations</b>	<b>55</b>
6.1 Simulations . . . . .	55
6.2 Analytical approach. . . . .	56
6.3 General findings . . . . .	57
6.4 Recommendations . . . . .	57

---

<b>Bibliography</b>	<b>59</b>
<b>Appendices</b>	<b>65</b>
<b>A Appendix</b>	<b>65</b>
A.1 Additions to Chapter 2 . . . . .	65
A.2 Additions to Chapter 3 . . . . .	66
A.3 Additions to Chapter 4 . . . . .	67
A.4 Additions to Chapter 5 . . . . .	71

# List of Figures

1.1	A reservoir with a fault and conditions which would allow analytical calculations to be performed correctly when using the method of Poro-elastic Loading. . . . .	3
1.2	A reservoir with a fault and conditions which would allow analytical calculations to be performed correctly when using the method of Differential Compaction Loading but not PEL. . . .	3
2.1	Cross-section through a cylinder and the decomposition of forces. . . . .	5
2.2	a) Initial state before forces are applied b) elongation strain in $y$ -direction c) shear strain . . . .	6
2.4	Mohr-Coulomb diagram for two different depletions situations and their specific stress paths. . .	9
2.5	Forces on a 2-dimensional fault plane in a normal faulting stress regime. . . . .	10
2.6	Mohr-Coulomb diagram . . . . .	12
2.7	Mohr-Coulomb diagram for a fault before and after depletion describing how the maximum and minimum stress change with a decrease in pore pressure. . . . .	12
2.8	Shear stress on a vertical fault plane (modified after Hettema (2017)) . . . . .	13
2.9	Systematic figure of a depleting system to illustrate differences between both fault reactivation criteria. . . . .	16
3.1	Variscan orogeny belt across western Europe . . . . .	18
3.2	Time slices of Europe's tectonic history [20] . . . . .	19
3.3	Stratigraphic column of the lithologies beneath the Groningen high. . . . .	20
3.4	Stratigraphic column of the Carboniferous sediments beneath the Groningen High. . . . .	21
3.5	Stratigraphic column of the Permian sediments beneath the Groningen High. . . . .	22
3.6	Stratigraphic column of the Late Permian Zechstein sediments forming the seal of the Groningen reservoir. . . . .	23
3.7	Time slices of North Western Europe's depositional environments Doornenbal and Pagnier(2004)	24
4.2	Distribution of average fault dips after Kortekaas and Jaarsma (2017). . . . .	26
4.3	Model dimensions with homogeneous rock properties resembling the Slochteren formation. Reservoir top is found at $-2800m$ depth and is crossed by a fault which continues in the over- and underburden for a certain distance . . . . .	27
4.4	Dependency of Young's modulus and Poisson's ratio on porosity. Measured on cores of the Slochteren reservoir. (Lele et al. 2015) . . . . .	29
4.5	Dependency of compaction coefficient on porosity. Measured on cores of the Slochteren reservoir. (Lele et al. (2015)) . . . . .	29
4.6	Change from static to dynamic friction angle. It is unknown if this decrease occurs instantly, linearly of a certain length of displacement or in a non-linear manner. . . . .	31
5.2	Vertical displacements profiles of top, base and center of a reservoir with thickness $h = 100m$ and $h = 200m$ . . . . .	35
5.5	Horizontal displacement of the reservoir and the surrounding formations after $20MPa$ depletion.	36
5.7	Comparison of the relative shear stress for each step of depletion from various simulation runs in which the Poisson's ratio was varied. . . . .	37
5.8	Comparison of three different Radii for three different stages of depletion over the entire length of the fault and a zoomed section of the reservoir top. . . . .	38
5.9	Comparison of the yield pressure for all base case models with varied reservoir thickness. . . .	39
5.11	Comparison of the yield pressure for all base case models with varied throw. . . . .	40
5.13	Comparison of the yield pressure for all base case models with varied fault dip. . . . .	42
5.16	Histogram showing the spread for the values of yield pressure for all the models run. . . . .	44

5.18	Density distribution showing the probability for each value of yield pressure for the various rock / fault parameters in the chosen range. This indicates which parameters have a large effect on failure . . . . .	46
5.20	a) Change of $\Lambda_f$ with depth within the reservoir section of a vertical fault. b) Exact and approximated fitting of the calculated compaction induced shear stress $\tau_{vh}$ from the vertical displacements to the modelled shear stress $\tau_f$ . . . . .	48
5.21	Relationship between $\Lambda$ and the analyzing distance $L$ by formulating the variable constant $C$ . . . . .	48
5.23	The dependency of the factor $c$ on the fault angle and on which value is entered for the radius $R$ in the analytical approach. Note: do not confuse this with the actual value of the reservoir radius. . . . .	50
5.24	Comparison of the analytical and simulated reactivation pressures for different fault angles. . . . .	50
5.25	Comparison of the analytical and simulated reactivation pressures with $\beta_{f,new} = 180^\circ - \beta_f$ for different fault angles. . . . .	51
5.26	Rotation angle varying with depletion. . . . .	52
5.27	Analytically calculated critical angle for faults with various friction angles. . . . .	53
A.1	Relationships among elastic constants in isotropic materials by Mavko et al.(2009) . . . . .	65
A.2	Chronostratigraphic chart by on Stratigraphy . . . . .	66
A.3	Schematics of all varied geometries used in the sensitivity study. . . . .	67
A.4	Model with "infinite" boundaries and zoomed-in section to assess the influence range of horizontal displacement around a depleting reservoir. . . . .	68
A.6	Comparison of an axisymmetrical model with plane strain model. . . . .	70
A.7	Measured subsidence for reservoir pressure in the Groningen gas field after [31] . . . . .	70
A.8	Relative shear stress on a fault with angle of $79^\circ$ . It can be seen that the point of zero shear stress is in the lower half of the reservoir. . . . .	71

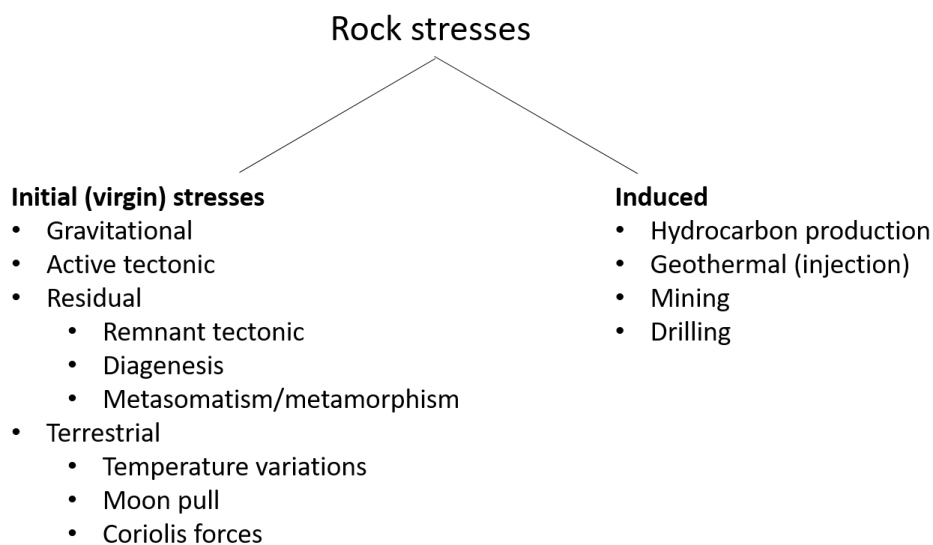
# List of Tables

2.1	Table comparing both reactivation criteria with data from figure 2.9 . . . . .	15
4.1	Range of fault dips, throws and reservoir thickness . . . . .	26
4.2	Differences in varied geometries of the reservoir and fault. . . . .	27
4.3	Range of varied rock and fault strength parameters . . . . .	30
5.1	Amount of runs performed for each parameter . . . . .	44
A.1	Various model dimension to test influence of VIT. . . . .	68



# Introduction

The production or injection of fluids, may they be liquid or gaseous hydrocarbons or just water, change the in-situ stress situation in the subsurface. Not only do these changes affect the subsurface, but they propagate through the overlying rock formations to the surface, where some effects of these stress changes can be seen. This can affect the daily life of the population in areas where production or injection operations are ongoing. The initial/virgin stress situation in the subsurface is mainly created by gravitational and active tectonic stresses. Other factors shown in the list below also play a role. Next to these natural stresses, human activity can lead to induced stress due to injection and extraction of fluids linked to hydrocarbon or geothermal projects such as Enhanced Oil Recovery, stimulation, drilling and storage purposes for natural gas or Carbon Capture and Storage (Orlic et al. 2013, Grasso 1992).



Direct effects of the in-situ stress changes are subsidence of the surface and seismicity within the reservoir. Both these phenomena may lead to damage of property and infrastructure as well as cause safety issues. Less visible to society are the technical difficulties that are faced in the subsurface by the industry. Effects such as wellbore collapse and loss of cap-rock integrity and possibly corresponding fluid leakage through it or along faults<sup>1</sup> are only a few. One difficulty which has the possibility to cause problems to both society and industry is fault reactivation which is the main focus of this thesis (Zoback 2010, Nacht et al. 2010).

<sup>1</sup>Faults are planar or gently curved fractures or discontinuities in a volume of rock. They are naturally created when the Earth's crust is subject to compressional or tensional forces caused by tectonics or other forces. Their length as well as the caused displacement can range from centimetres to hundreds of kilometres. Faults are classified according to their dip angles and relative displacement and show different properties than the surrounding rock. More on this in section 2.4.

In The Netherlands multiple gas fields have shown signs of subsidence and seismicity during the period of production in these reservoirs (Eijs et al., 2006, Roest and Kuilman 1994, Wees et al., 2014). The largest gas field in Europe, the Groningen gas field, lies directly beneath a populated area and is slowly subsiding. After a significant amount of gas production seismic events started occurring in 1991, with the largest event of Magnitude 3.6 on Richter's scale occurring in 2012 near Huizinge, NL (Wassing et al. 2016). In order to predict - or even better mitigate - these seismic events it is necessary to evaluate the factors that play a role in their occurrence.

## Mechanism

The extraction of gas reduces the pore-pressure within the reservoir. A homogeneous decrease in pressure throughout the reservoir and the reduction of the volume of gas causes compaction of the reservoir and vertical and horizontal displacement in the surroundings. Between reservoir compartments separated by faults, or the more extreme case of a reservoir boundary, the decrease in pressure is likely to be different across the fault. This leads to the phenomenon of differential compaction. This means that one part of the reservoir compacts more than the other. As previously mentioned, the main driving force is the pressure difference across the fault. Besides this, the geometry of the reservoir and the rock and fault properties play an influential role. Either way, so with homogeneous reservoir and pressure decrease conditions or not, the stresses in and around the reservoir change. A large enough change can cause initiation of fault reactivation and seismicity to occur (Hettema, 2017)). However, three factors are needed for seismicity: 1) initiation of fault slip 2) propagation of fault slip and 3) seismicity generation (enough energy is set free for the event to be registered). It is important to understand that even though 2) can only happen if 1) has and 3) consequently only if 2) has, it does not mean that it always happens. And in the case it does, it is defining in which manner. To reach the above stated goal of prediction and mitigation we need to start at the beginning, at 1). In this thesis all the work done tries to get a better view and understanding of the process around the initiation of fault reactivation. The link to fault slip propagation and seismicity generation will not be further discussed.

## Previous Research

Compaction and subsidence of depleting gas reservoirs has been mathematically described by Geertsma (1973). Shortly thereafter Van Opstal (1974) extended the model by adding the effect of a rigid basement. It was then further improved by Tempone et al. (2010).

After production-induced seismicity started occurring in producing fields around the world mathematical models were developed to explain the mechanisms responsible. Calculations with simple geometries were able to predict stress perturbations that were consistent with observed earthquake locations and focal mechanisms (Segall (1989)). Including other data from subsidence measurements or rock properties lead to the conclusion that seismicity could often be traced back to the reactivation of faults above, below or within the reservoir (Bourne et al. (2006)).

Many have given insight into what happens before and at the onset of fault reactivation using both numerical simulations as well as the Mohr-Coulomb method for assessing the fault failure criterion.

Some of the numerical simulations were based on real cases such as the Eleveld field (Roest and Kuilman (1994)) or the Roswinkel field (Van Wees et al.(2003)). As not only fields with hydrocarbon production show seismicity, studies were performed on deep geothermal fields (Moeck et al. (2009)) or fields used for underground gas or  $CO_2$  storage (Nagelhout and Roest (1997), Orlic et al. (2013)).

Others were more focused on the general mechanisms behind fault reactivation and used synthetic fields that often mimic the the setting of a typical Rotliegend field in the Dutch subsurface (Mulders (2003)). Building on these simple principles (Orlic and Wassing (2013)) extended the research to include the effect of a visco-elastic cap-rock. Van den Bogert (2015) has performed research on the importance of various factors such as magnitude of pore-pressure change, geometry of the reservoir, fault throw, dip and azimuth as well as the geomechanical properties of the rocks and faults up to a certain measure.

Also different approaches with energy balance equations (van den Bogert (2015)) or statistical methods (Eijs et al. (2006)) were constructed as proposed methods to gain better understanding in the occurrence and mechanisms behind fault-reactivation.

The most recent research, such as from Wassing et al. (2016), have put effort into modelling and describing what happens post-failure and have modelled the dynamic behaviour of reactivated faults to assess how fault rupture propagates.

Through the more recent advances in Finite Element Modelling (FEM) at least two conclusion were formed:

1. Simulations show more similar results to what we see from observations.
2. The way in which fault failure is currently calculated analytically does not coincide with what is seen in simulations.

This analytical method is called Poro-Elastic Loading (PEL) and is used in many applications in the industry. It is a simplified version of the complete mathematical problem to describe normal and shear stress on the fault. So realizing that this simplification is not sufficient, a new analytical approach using the complete mathematical approach has been developed by Hettema 2017. We will name this mechanism Differential Compaction Loading (DCL). The reason for the differences between the simulations and the analytical approach are that PEL can only be used under certain conditions and assumptions. These are:

- There is no rotation of the principal stresses with depletion
- There is no differential compaction in the reservoir. This means:
  - The fault is entirely permeable therefore the pressure decrease on both sides is equal,
  - the fault has no throw,
  - the reservoir properties are equal on both sides of the fault.

Differential Compaction Loading on the other hand can be used in all other situations, when the above conditions are not met or when the assumptions are not valid. Figures 1.1 and 1.2 are illustrations of reservoirs with faults that will abide to either one of the two methods.

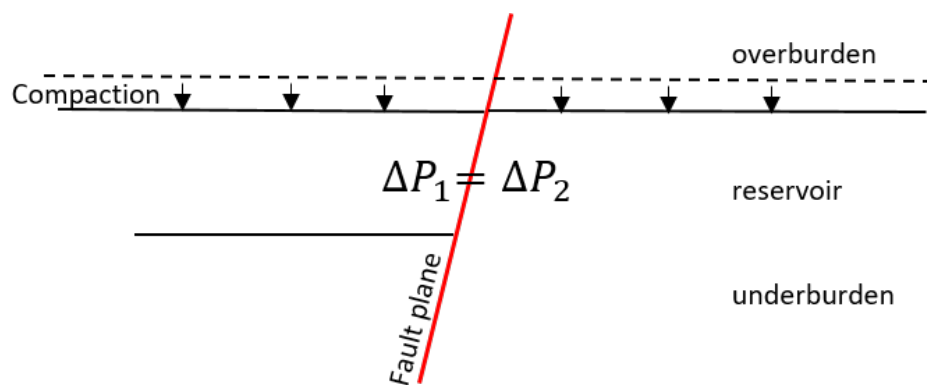


Figure 1.1: A reservoir with a fault and conditions which would allow analytical calculations to be performed correctly when using the method of Poro-elastic Loading.

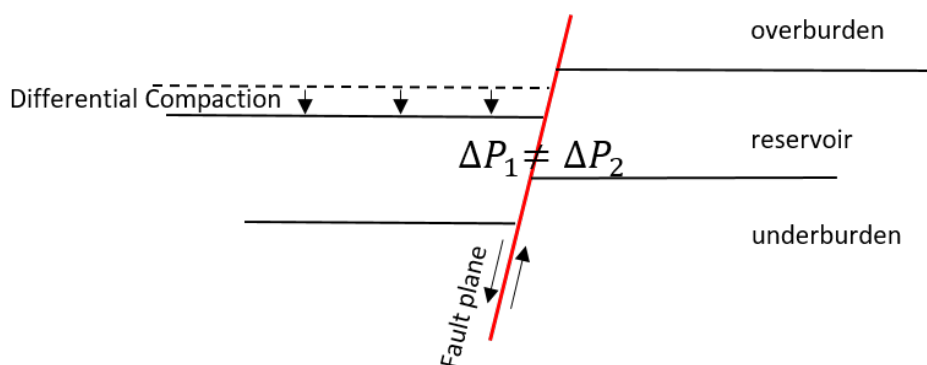


Figure 1.2: A reservoir with a fault and conditions which would allow analytical calculations to be performed correctly when using the method of Differential Compaction Loading but not PEL.

## Goal of this thesis

Based on previous research, the goal of this MSc. thesis is to create a better understanding of the mechanisms controlling the initiation of fault reactivation of a reservoir boundary fault which occurs due to production of gas from the subsurface. The three main research questions are:

**1. How does reservoir depletion lead to fault reactivation?**

Goals are to quantify stresses, strains and displacements within a depleting reservoir.

**2. What is the fault failure sensitivity to variation in reservoir and fault geometry, rock properties and fault strength. Which factors play a role and in what measure?**

The goal is to identify which factors play a role in fault failure and in what measure. With this, the study provides an approach on how an empirical sense for the sensitivity for certain parameter combinations can be created.

**3. How can PEL and DCL be quantified when the analytical approach by Hettema (2017) and Finite Element Modelling (FEM) in Plaxis are compared?**

The goal is to compare the analytical approach with simulations for geometry and material property variations of fault and reservoir configurations. The goal is to calibrate certain parameters of the analytical approach and to relate simulated phenomena to theory.

## Approach

In this thesis, the theory of compaction by Geertsma (1973) is used to describe displacements within the reservoir. Stress and strain on a fault plane, within and around the reservoir are described and its values estimated using a Mohr-Coulomb analysis. The method implements the mechanism of DCL as described by Hettema (2017).

To assess fault failure sensitivity FEM in Plaxis was used. A base-case model was created and validated. With it, the general behaviour of a depleting reservoir could be analysed. Adequate values for material properties and geometry were obtained from literature or data. From this base-case model (figure 4.3) and its parameters a set of scenarios was designed in which for each geometrical change, the parameters were varied in a certain range as well. From this various relationships on fault failure behaviour could be found.

The analytical approach by Hettema (2017) was then compared to the results from the simulations. In this process a tuning of a yet unknown factor allowed for the simulations and analytical calculations to match. Also the dependency on various input parameters and the robustness of this factor were investigated. From the relationships obtained by the simulations it became possible to also derive new theoretical relations. Because of this a better understanding of the mechanisms behind Differential Compaction was formed.

From these steps conclusions are drawn and recommendations for further research are given.

# 2

## Theory of Geomechanics

This chapter gives an overview of the various theoretical aspects necessary to describe the phenomena that occur in a depleting reservoir subdued to differential compaction.

### 2.1. Stress and Strain

In the study of rock mechanics the most important behaviours are elasticity and plasticity. Elasticity is the ability of a rock to recover from deformation. Plasticity is when the rock cannot completely recover from the deformation and permanent changes in shape occur.

Linear elasticity can be assumed when changes in forces are sufficiently small. This rests upon the concepts of stress and strain as described in more detail by Fjær et al. (2008).

**Stress**  $\sigma$  is defined as force  $F$  [N] per area  $A$  [m<sup>2</sup>] and measured in Pascal [Pa]. In rock mechanics compressive stresses are by definition positive.

$$\sigma = \frac{F}{A} \quad (2.1)$$

The normal stress is defined perpendicular to the surface which it acts upon. The stress parallel to this surface is called shear stress  $\tau$ . Figure 2.1 shows a cross-section of a cylinder which is subject to a vertical force perpendicular to the surface  $A$  and the respective forces that work on that section as well as a non-perpendicular section  $A''$ .

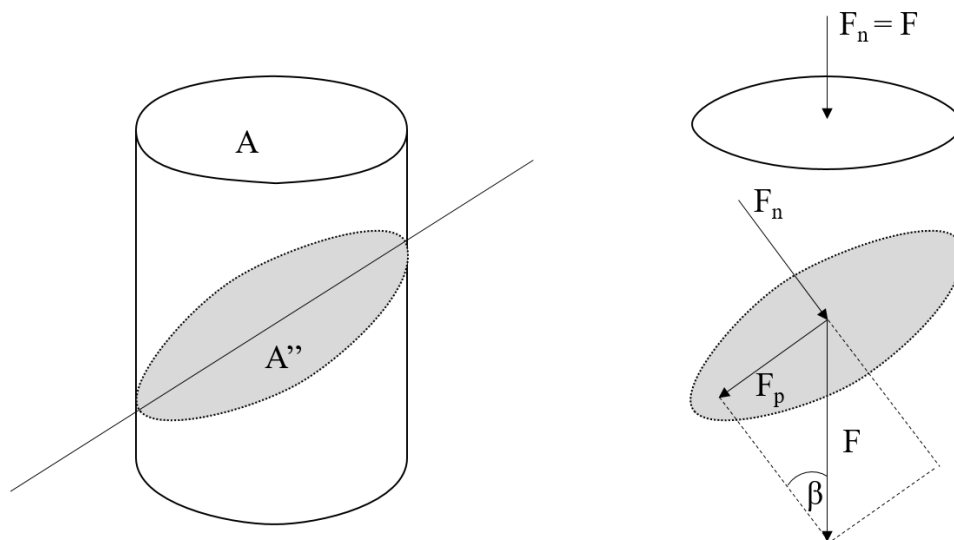


Figure 2.1: Cross-section through a cylinder and the decomposition of forces.

For the horizontal surface  $A$  equation 2.1 is valid. However, for the surface  $A''$  which is tilted at an angle  $\beta$

the total force  $F$  can be calculated using the following equations for stress and strain using the decomposed forces  $F_n$  and  $F_p$  as shown in figure 2.1:

$$\sigma = \frac{F_n}{A''} \quad (2.2)$$

$$\tau = \frac{F_p}{A''} \quad (2.3)$$

To give a complete description of the stress state at a specific point in three dimensions stress can be written in form of the stress tensor:

$$\begin{pmatrix} \sigma_x & \tau_{xy} & \tau_{xz} \\ \tau_{yx} & \sigma_y & \tau_{yz} \\ \tau_{zx} & \tau_{zy} & \sigma_z \end{pmatrix}$$

This tensor can be formulated in terms of just the principal stress  $\sigma_1, \sigma_2$  and  $\sigma_3$  by means of a rotation around the angle of incidence or rotation angle of the force. Due to this, all shear stress becomes zero. This forms the definition of principal stresses.

$$\begin{pmatrix} \sigma_1 & 0 & 0 \\ 0 & \sigma_2 & 0 \\ 0 & 0 & \sigma_3 \end{pmatrix}$$

**Strain** is defined as deformation per unit length that occurs due to an imposed force. There are two forms of strain, illustrated in figure 2.2. The first is elongation  $\varepsilon$  and is defined as the change in length  $\Delta L$  over the original length  $L$ . When infinitesimal strain is assumed the strain can be defined in a linear relationship as below for the x- as well as y-direction where  $\delta u_x$  and  $\delta u_y$  describe the displacement in x- and y-direction.

$$\varepsilon = -\frac{\Delta L}{L} \quad (2.4)$$

$$\varepsilon_x = \frac{\delta u_x}{\delta x}; \quad \varepsilon_y = \frac{\delta u_y}{\delta y} \quad (2.5)$$

The second type is shear strain  $\Gamma$  describes the change of angle  $\Psi$ . For infinitesimal strain it can be written as in equation 2.6.

$$\Gamma = \frac{1}{2} \tan \Psi \quad (2.6)$$

$$\Gamma_{xy} = \frac{1}{2} \left( \frac{\delta u_x}{\delta y} + \frac{\delta u_y}{\delta x} \right) \quad (2.7)$$

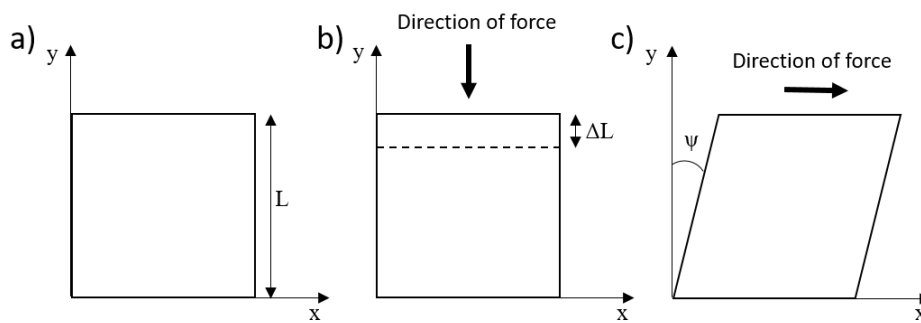


Figure 2.2: a) Initial state before forces are applied b) elongation strain in y-direction c) shear strain

Just as for stress, the strain tensor describes the strain occurring at a specific point in three directions.

$$\begin{pmatrix} \varepsilon_x & \Gamma_{xy} & \Gamma_{xz} \\ \Gamma_{yx} & \varepsilon_y & \Gamma_{yz} \\ \Gamma_{zx} & \Gamma_{zy} & \varepsilon_z \end{pmatrix}$$

Rocks behave linearly under small changes in stress but might show non-linearity when subjected to larger stresses (Fjær et al. 2008).

## 2.2. Elastic Moduli

The moduli describe the characteristics of a rock. There are multiple types of moduli but the most important ones used in this thesis *Young's modulus*  $E$ , *Poisson's ratio*  $\nu$ , *shear modulus*  $G$  and the *bulk modulus*  $K$  are described below.

The first one,  $E$ , is defined as below under the assumption that rock materials behave linearly and thus stress and strain are also related linearly:

$$\varepsilon_x = \frac{1}{E}\sigma_x \quad (2.8)$$

This equation is known as Hooke's law, where  $E$  is the Young's modulus. Its unit is  $[Pa]$ . This is a measure of stiffness of a material. When a material is put under stress it deforms in both vertical and horizontal directions,  $\varepsilon_y$  and  $\varepsilon_x$  respectively. The ratio between these two is known as Poisson's ratio which forms the second elastic modulus listed here.

$$\nu = \frac{\varepsilon_y}{\varepsilon_x} \quad (2.9)$$

For isotropic materials<sup>1</sup> the mathematical notation for stress and strain can be written as follows:

$$\sigma_{ij} = \lambda \varepsilon_{kk} \delta_{ij} + 2\mu \varepsilon_{ij} \quad (2.10)$$

$$\varepsilon_{ij} = \frac{1}{2} \left( \frac{\delta u_i}{\delta x_j} + \frac{\delta u_j}{\delta x_i} \right) = \frac{1}{E} \left( (1 + \nu) \sigma_{ij} - \nu \sigma_{kk} \delta_{ij} \right) \quad (2.11)$$

Where  $i$  and  $j$  are either 1, 2 or 3, representing the  $x$ -,  $y$ -, and  $z$ -axis ( $u_1 = u_x, u_2 = u_y, u_3 = u_z, x_1 = x, x_2 = y, x_3 = z$ ) (Fjær et al. (2008)) and  $\lambda$  and  $\mu = G$  are the Lamé-parameters.  $G [Pa]$  is also called the shear modulus and is the third modulus listed here. It indicates the ability of a rock to resist shear stress.  $\lambda$  is known as Lamé's constant and is sometimes referred to as incompressibility<sup>2</sup>.  $\varepsilon_{kk}$  and  $\sigma_{kk}$  are the traces of the strain and stress tensor and  $\delta_{ij}$  is the Kronecker Delta, a function which is 1 for  $i = j$ . The above parameters can be described as follows.

$$\lambda = \frac{E\nu}{(1 + \nu)(1 - 2\nu)} \quad (2.12)$$

$$\mu = \frac{E}{2(1 + \nu)} = G \quad (2.13)$$

$$\varepsilon_{kk} = \varepsilon_x + \varepsilon_y + \varepsilon_z \quad (2.14)$$

$$\sigma_{kk} = \sigma_x + \sigma_y + \sigma_z = \frac{\varepsilon_{kk} E}{1 - 2\nu} \quad (2.15)$$

$$\delta_{ij} = \begin{cases} 1 & \text{if } i = j \\ 0 & \text{if } i \neq j \end{cases}$$

The last modulus to mention here is the bulk modulus  $K$ . It describes the measure of a sample's resistance against hydrostatic compression and can be described as the hydrostatic stress  $\sigma_p$  over the volumetric strain  $\varepsilon_{vol}$  or as the reciprocal of the compressibility  $\beta_{compr}$  of the dry rock (Fjær et al. (2008) p.21).

$$K = \frac{\sigma_p}{\varepsilon_{vol}} = \frac{1}{\beta_{compr}} = \lambda + \frac{2}{3}G \quad (2.16)$$

All elastic moduli can be described in terms of the other elastic moduli. Mavko et al. (2009) gives a good overview of these moduli with a conversion table (see Appendix A figure A.1).

<sup>1</sup>Materials that behave the same, irrespective of the direction of the applied force.

<sup>2</sup>It is, however, not the reciprocal of the compressibility  $\beta_{compr}$  (Mavko et al. (2009)).

### 2.3. Poro-elasticity

The descriptions of stress and strain above are true for isotropic homogeneous solid materials without porosity. Typical reservoir rocks, however, are not entirely solid materials as they have a specific porosity. This alters their elastic behaviour. These effects are described with the concept of poro-elasticity by Biot (1962).

$$\sigma_{ij} = \sigma' - \alpha p \delta_{ij} \quad (2.17)$$

In his paper, Biot shows that the external stresses are carried by two parts. One: the effective stress working on the framework  $\sigma'$ . Two: the amount of stress carried by the fluid which translates to pore pressure as  $\alpha p \delta_{ij}$ , in which the Biot's coefficient  $\alpha$  is described as:

$$\alpha = 1 - \frac{K_{fr}}{K_s} = \frac{\Delta V_p}{\Delta V_{tot}} \quad (2.18)$$

$K_{fr}$  is the bulk modulus of the framework and  $K_s$  the bulk modulus of the solid. The following relations between them always apply. The first one is the Voigt bound as described by Watt et al. (1976).  $\phi$  is the porosity of the rock and for weak rocks  $\alpha$  is close to 1 (Fjær et al. (2008)).

$$0 < K_{fr} < (1 - \phi)K_s$$

$$\phi < \alpha < 1$$

### 2.4. Initial stress regimes and stresses during depletion

As an introduction to stress in the Earth and its development during various forms of stress changes Anderson (1905) described a number of tectonic stress regimes. The classification consists of normal, strike-slip and reverse faulting. Figure 2.3 shows these along with their beach-ball illustrations which clarify the directions of compression  $P$  and extension  $T$ .

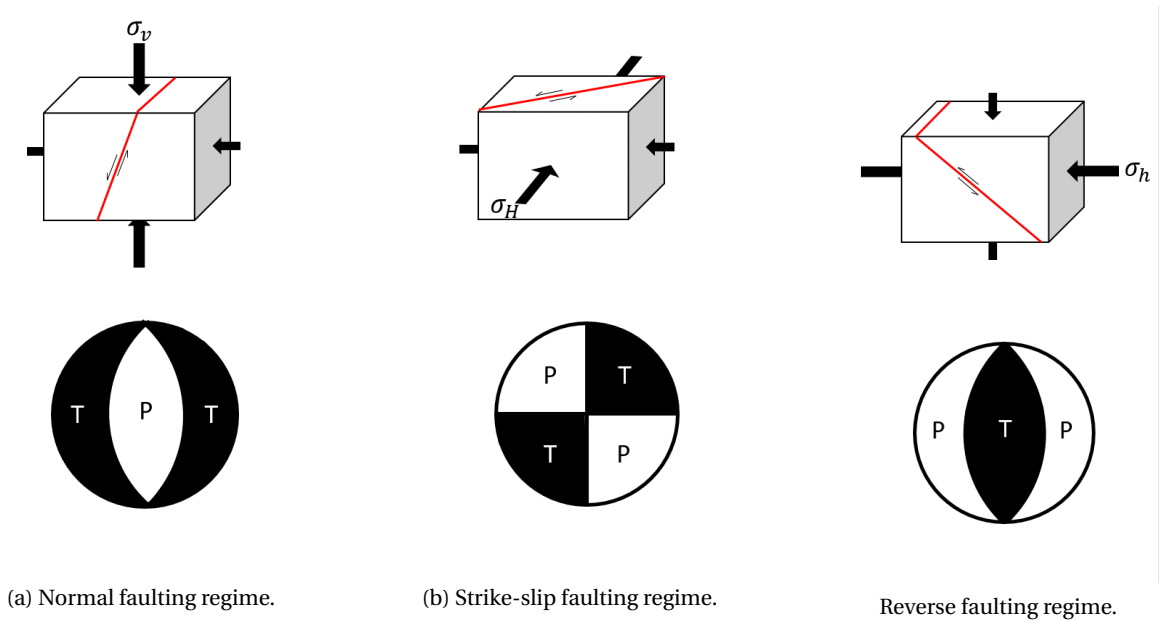


Figure 2.3: Faulting regimes according to Anderson (1905)

For modelling purposes, the relations between the stresses are described with the effective stress ratios  $K_{0H}$  and  $K_{0h}$  for the maximum and minimum horizontal stress respectively.

$$K_{0H} = \frac{\sigma'_H}{\sigma'_v} \quad (2.19)$$

$$K_{0h} = \frac{\sigma'_h}{\sigma'_v} \quad (2.20)$$

The effective vertical stress  $\sigma'_v$  is calculated by integrating the density of the formations over the depth  $z$  as in equation 2.21.

$$\sigma'_v = \int_z^0 \rho(z) g dz \quad (2.21)$$

$$\sigma'_H = \sigma'_h = \frac{\nu}{1-\nu} \sigma'_v \quad (2.22)$$

The effective horizontal stresses  $\sigma'_H$  and  $\sigma'_h$  are often assumed to be equal for simplicity. A translation of the vertical stress to the horizontal plane is achieved by using the Poisson's ratio as in equation 2.22, which is derived from equation 2.11. It is important to realize that the  $K_0$  values can range from 0.2 to 1.5 at larger depths, as no sediment reacts perfectly elastic and that there are always other stresses imposed on the lithologies (Fjær et al. (2008)).

During depletion of a reservoir the *pore pressure*  $p$  drops, as a result of which the effective vertical and horizontal stresses change. Equations 2.23 to 2.25, derived from the theory of poro-elasticity, show that as pore pressure decreases the effective stress within the reservoir increases. (With  $\Delta\sigma' = \sigma'_{after\ depletion} - \sigma'_{initial}$ )

$$\Delta\sigma_v = \Delta\sigma'_v + \alpha\Delta p \quad (2.23)$$

$$\Delta\sigma_H = \Delta\sigma'_H + \alpha\Delta p \quad (2.24)$$

$$\Delta\sigma_h = \Delta\sigma'_h + \alpha\Delta p \quad (2.25)$$

A very practical way to quantify the changes is total stress and to estimate fault behaviour with depletion is by defining the vertical and horizontal stress paths  $\gamma_v$  and  $\gamma_h$  respectively. The stress path is used to estimate fault behaviour.

$$\gamma_v = \frac{\Delta\sigma_v}{\Delta p} \quad (2.26)$$

$$\gamma_h = \frac{\Delta\sigma_h}{\Delta p} \quad (2.27)$$

$\gamma$  is a specific characteristic for each reservoir and is especially useful to indicate if a fault is stabilizing or de-stabilizing, moving away from or towards failure respectively. Figure 2.4 shows a Mohr-Coulomb diagram with two different depletion situations, each with their specific stress paths. Whilst  $\gamma_{h1}$  moves away from the failure line thus stabilizing the fault,  $\gamma_{h2}$  crosses it, thus causing the fault to fail. Hettema et al. (2000) describes the strong influence of the stress path of a reservoir in detail. The Mohr-Coulomb diagram will be discussed further in the following sections.

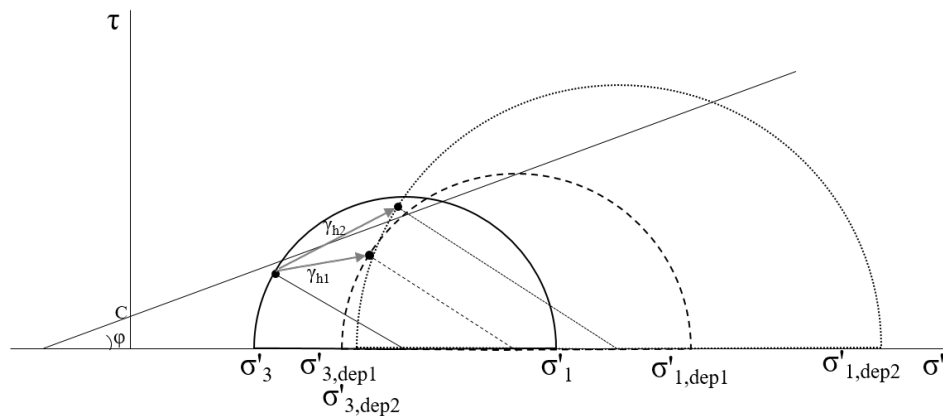


Figure 2.4: Mohr-Coulomb diagram for two different depletions situations and their specific stress paths.

In case of a compacting reservoir, Geertsma and Van Opstal (1973) state that the compaction-induced change in  $\sigma_v$  is very small for a laterally extensive reservoir thus making the stress path  $\gamma_v$  very small. Morita

et al. (1989) were able to prove that the effect on  $\gamma_v$  is negligible, even in a case where the simplification of Geertsma and Van Opstal on constant stiffness of reservoir, over- and underburden are not met.

$\gamma_h$ , however, experiences a larger change ( $\gamma_h > \gamma_v$ ) and lies between  $0 \leq \gamma_h \leq \alpha$ . If  $\gamma_h = 0$  the horizontal stress is totally independent of the pore pressure but the effective stress change is maximum. And if  $\gamma_h = \alpha$  the effective horizontal stress does not change.

From this it becomes possible to calculate the change in effective horizontal and vertical stress. One can assume  $\Delta\sigma_v = 0$  for a laterally extensive reservoir. Combining equations 2.22 and 2.23 the horizontal stress change can be written as:

$$\Delta\sigma_h = \left( \frac{1-2\nu}{1-\nu} \right) \alpha \Delta p \quad (2.28)$$

And equation 2.27 becomes:

$$\gamma_h = \frac{\Delta\sigma_h}{\Delta p} = \alpha \left( \frac{1-2\nu}{1-\nu} \right) \quad (2.29)$$

resulting in:

$$\Delta\sigma_h = \gamma_h \Delta p \quad (2.30)$$

Inserting this into equation 2.25 allows the change in effective horizontal stress to be defined as:

$$\Delta\sigma'_h = (\gamma_h - \alpha) \Delta p \quad (2.31)$$

For the vertical stress change something similar can be done. Here, however,  $\gamma_v = 0$  if  $\Delta\sigma_v = 0$  so we receive:

$$\Delta\sigma'_v = -\alpha \Delta p \quad (2.32)$$

## 2.5. Stress and strain on a 2D fault plane

Moving from the general principles to the principles of fault reactivation, which are of main interest in this thesis, it can be said that failure of rock occurs between particles of the rock and thus it concerns failure of the framework. This means that the effective (and not total) stress determines if failure occurs (or not) due to an external load or increase/decrease in pore pressure  $p$ . Especially of interest is the failure of planes of weakness: faults.

To determine if failure occurs, the local stresses on the fault need to be known. Imagine a situation as in figure 2.5 which shows the decomposition of the various forces working on a two-dimensional fault plane in the subsurface. The normal effective stress  $\sigma'_f$  and shear stress  $\tau_f$ , which influence the local stress situation on a fault, can be calculated as follows:

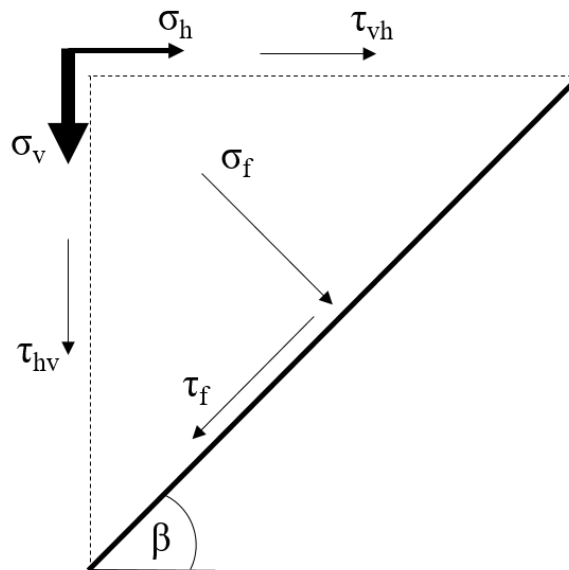


Figure 2.5: Forces on a 2-dimensional fault plane in a normal faulting stress regime.

$$\sigma'_f = \frac{\sigma'_v + \sigma'_h}{2} + \left( \frac{\sigma_v - \sigma_h}{2} \right) \cos 2\beta + \tau_{vh} \sin 2\beta \quad (2.33)$$

$$\tau_f = -\frac{\sigma_v - \sigma_h}{2} \sin 2\beta + \tau_{vh} \cos 2\beta \quad (2.34)$$

$$|\tau_f| = \frac{\sigma_v - \sigma_h}{2} \sin 2\beta - \tau_{vh} \cos 2\beta \quad (2.35)$$

The main components of the equations are the effective  $\sigma'_v$  and normal vertical stress  $\sigma_v$ , the effective and normal minimum horizontal stress  $\sigma'_h$  and  $\sigma_h$ , the fault angle  $\beta$  and the induced shear stress  $\tau_{vh}$ . Both values of stress, the effective normal and shear stress, can be easily calculated (see equation 2.21) or measured using leak-off tests (LOTs).<sup>3</sup> In equations 2.33 and 2.34 the induced shear stress  $\tau_{vh}$  still remains unknown.

By means of a mathematical rotation, as mentioned in section 2.1, it is possible to eliminate the term  $\tau_{vh}$  from equation 2.33 and 2.34. This introduces the principal stresses  $\sigma_1$  and  $\sigma_3$  to the equation which have a different (but unknown value) than  $\sigma_v$  and  $\sigma_h$ . Equations 2.33 and 2.34 take on following simplified form:

$$\sigma'_n = \frac{1}{2}(\sigma'_1 + \sigma'_3) + \frac{1}{2}(\sigma_1 - \sigma_3) \cos 2\beta \quad (2.36)$$

$$\tau_f = -\frac{1}{2}(\sigma_1 - \sigma_3) \sin 2\beta \quad (2.37)$$

These equations describe the mechanism of Poro-elastic Loading (PEL). In the calculation of the normal and shear stress on a fault it has been common practice to continue using the vertical and horizontal stress. However, neglecting the difference between the principal and Earth' stresses is an assumption which leads to errors in the calculated values.

A practical way of visualizing the stress situation of rocks or faults is by plotting the local stress situation in a Mohr-Coulomb diagram. This plot consists of a Mohr's circle with a radius equal to the maximum shear stress  $\tau_{max}$  (see equation 2.38) and the Coulomb failure line. The largest value  $\tau_{max}$  can have before failure of the rock or fault is equal to the shear stress the fault can handle before the initiation of failure occurs  $\tau_{fail}$ . This parameter is also called the Coulomb failure criterion. To define it two parameters are necessary. The cohesion  $C$  of the rock or fault and the internal friction angle  $\varphi$ . It is written as:

$$\tau_{max} = \frac{\sigma_1 + \sigma_3}{2} \quad (2.38)$$

$$\tau_{fail} = C + \sigma'_n \tan \varphi \quad (2.39)$$

Figure 2.6 shows the Mohr circle together with the Coulomb failure criterion. For failure to occur the effective normal and shear stress need to result in a location on the failure line. The first point of the circle to touch the failure line is the point that represents a fault at the critical angle. This angle is related to the friction angle<sup>4</sup> of the fault as such:  $\beta_{crit} = 45^\circ + \frac{\varphi}{2}$ . For a fault at an angle  $\beta_{crit} < \beta < 90^\circ$  to be reactivated using the same fault strength parameters a change in stresses needs to occur so that that point of the circle touches the failure line. This can be achieved for example through depletion.

Consider a case where fluids are being produced from a reservoir causing a drop in pore pressure  $\Delta p$ . In figure 2.7 two Mohr circles are shown. One before depletion with a fault with angle  $\beta$  (represented by the point a  $2\beta$ ), where no point of the circle touches the failure line and one after a certain depletion of the reservoir where the fault reaches the failure line. In the case that other faults with angles that lie between both points crossing the failure line are present, they will all also be reactivated. It is interesting to note that for a fault with angle  $\beta = 90^\circ$  the failure line is never reached as the point representing a fault of  $90^\circ$  remains on the x- or  $\sigma'$ -axis. This means that when using the mechanism of PEL a fault with  $\beta = 90^\circ$  will never reactivate.

<sup>3</sup>A LOT is defined as: "A test to determine the strength or fracture pressure of the open formation ... During the test, the well is shut in and fluid is pumped into the wellbore to gradually increase the pressure that the formation experiences. At some pressure, fluid will enter the formation, or leak off, ... by fracturing the rock." ([15])

<sup>4</sup>Angle at which an item of a specific material placed on a slope will start sliding.

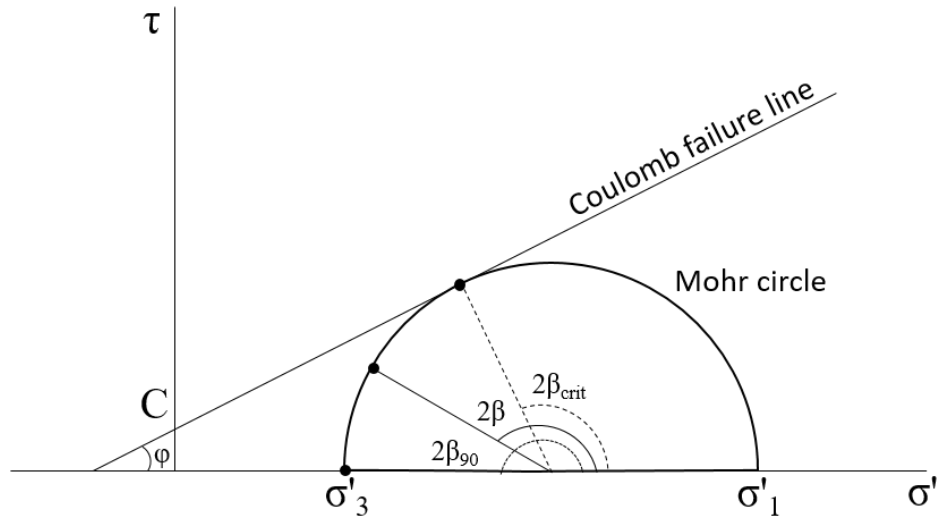


Figure 2.6: Mohr-Coulomb diagram

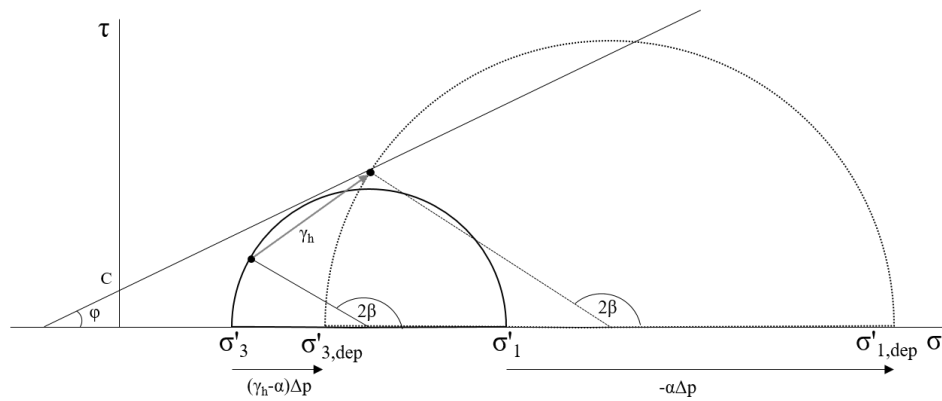


Figure 2.7: Mohr-Coulomb diagram for a fault before and after depletion describing how the maximum and minimum stress change with a decrease in pore pressure.

### 2.5.1. Differential compaction in producing reservoirs

Given that a fault with an angle of  $90^\circ$  would never reactivate an extremely high stress is needed to reactivate faults with steep angles when assessing the problem with the mechanism of PEL. However, in reality it is seen that also in reservoirs with steep and vertical faults reactivation occurs. This suggests that another mechanism plays a role in the reactivation of faults. According to Hettema (2017) this is related to the compaction of the reservoir layer which is crossed by the fault. We will refer to this second mechanism as Differential Compaction Loading (DCL). In the theory behind DCL an additional shear stress is induced on the fault plane, causing it to reactivate even at steep angles.

The difference between PEL and DCL is that instead of rotating the stress tensor in such a way that shear stress can be eliminated from the equation (as explained in section 2.1, equations 2.36 and 2.37), all parameters are used as in equations 2.33 and 2.34. This implies that  $\tau_{vh}$  needs to be determined. To demonstrate how shear stress can develop on a vertical plane figure 2.8 shows a differentially compacting reservoir as an example (Hettema (2017)).

In figure 2.8,  $L_1$  and  $L_2$  are the influence distances of shear strain  $\varepsilon$  to each side of the fault. This is the distance where deformation no longer changes with distance to the fault and uniaxial conditions can be assumed.  $G_1$  and  $G_2$  are the shear modulus of the reservoir and  $u_1$ ,  $u_2$  and  $u_f$  are the vertical displacements of the reservoir at different positions as indicated in the figure.

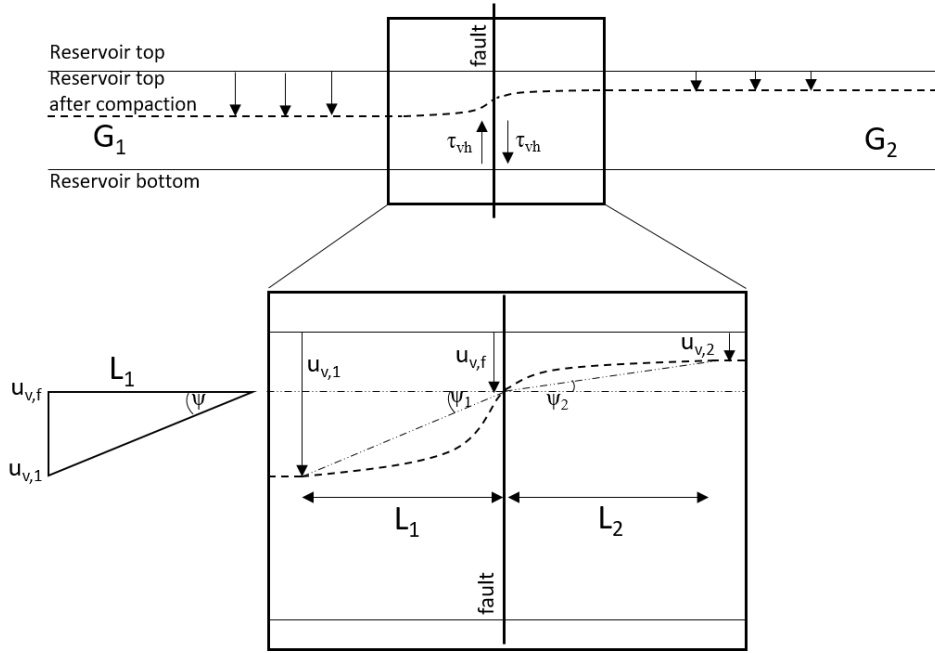


Figure 2.8: Shear stress on a vertical fault plane (modified after Hettema (2017))

It is possible to calculate  $\tau_{vh}$  with Hooke's law (equation 2.11) as follows:

$$\Gamma_{ij} = \varepsilon_{ij} = \frac{1}{2} \left( \frac{\delta u_i}{\delta x_j} + \frac{\delta u_j}{\delta x_i} \right) \quad (2.40)$$

$$\tau_{ij} = 2G\Gamma_{ij} = 2G\varepsilon_{ij} = G \left( \frac{\delta u_i}{\delta x_j} + \frac{\delta u_j}{\delta x_i} \right) \quad (2.41)$$

$$\left( \frac{\delta u_i}{\delta x_j} + \frac{\delta u_j}{\delta x_i} \right) = \tan \psi = \frac{u_1 - u_f}{L_1} = \frac{\Delta u_1}{L_1} \quad (2.42)$$

$$\tau_{ij} = G_1 \frac{\Delta u_1}{L_1} = G_2 \frac{\Delta u_2}{L_2} \quad (2.43)$$

So the difference in compaction  $\Delta u = \Delta u_1 - \Delta u_2$  can be described as  $(u_1 - u_f) + (u_f - u_2)$ . This leads to the following set of equations and the definition of  $\tau_{vh}$  as it is used in this thesis (equation 2.41):

$$\Delta u = \frac{L_1 \tau_{vh}}{G_1} + \frac{L_2 \tau_{vh}}{G_2} \quad (2.44)$$

$$\tau_{vh} = G_f \frac{u_1 - u_2}{L_1 + L_2} = G_f \frac{\Delta u}{L_1 + L_2} \quad (2.45)$$

$$G_f = \frac{2}{\left( \frac{1}{G_1} + \frac{1}{G_2} \right)} \quad (2.46)$$

Now still left unknown are the vertical displacements  $u_1$  and  $u_2$  as well as the influence distances  $L_1$  and  $L_2$ .

### 2.5.2. Compaction, Subsidence and Vertical Displacement

In Hettema's (2017) analytical approach for DCL displacement due to compaction is affected by the geometry of the reservoir. To describe this displacement it is not necessary for the reservoir to have uniaxial strain conditions<sup>5</sup> are valid. It is assumed this is the case for large parts of the reservoir as it is laterally much larger than its thickness.

Following from the definition of vertical strain  $\varepsilon_v$  (equation 2.4), the change in height or compaction  $\Delta h$  of a depleting reservoir can be described by the vertical strain times the original height  $h$ .

<sup>5</sup>Uniaxial conditions means that there is no horizontal strain and the vertical stress remains constant in those regions.

$$\Delta h = -\varepsilon_v h \quad (2.47)$$

$$\frac{\Delta h}{h} = -\varepsilon_v = \frac{1}{E_{fr}} \Delta \sigma'_v - \nu_{fr} (\Delta \sigma'_H + \Delta \sigma'_h) \quad (2.48)$$

Using equation 2.22 and  $\Delta \sigma'_v = -\alpha \Delta p$  this becomes (dropping the subscript  $fr$ ):

$$-\varepsilon_v = \frac{1}{E_{fr}} \left( -\Delta \sigma'_v + 2 \frac{\nu}{1-\nu} \Delta \sigma'_v \nu \right) = \frac{1}{E} \left( \alpha \Delta p \left( \frac{(1+\nu)(1-2\nu)}{1-\nu} \right) \right) = C_m \alpha \Delta p \quad (2.49)$$

From this, both the compaction coefficient or uniaxial compressibility  $C_m$  and the compaction  $\Delta h$  can be defined:

$$C_m = \frac{1}{E} \frac{(1+\nu)(1-2\nu)}{1-\nu} \quad (2.50)$$

$$\Delta h = C_m \alpha \Delta p h \quad (2.51)$$

This approach has been used by Geertsma and Van Opstal (1973), whose nucleus of strain model shows how deformation of a compacting reservoir propagates through the overburden. In this work, they calculated the subsidence resulting from compaction of a small sphere. By adding the effect of many such spheres on top of each other it is possible to calculate the total subsidence. This method has a shortcoming as it is limited to the case where there is no contrast in elastic properties between the reservoir and its surroundings (homogeneous conditions). To calculate vertical displacement at any depth outside the reservoir they propose following equation 2.52, which is valid along the central axis.

$$u(z)_{out} = -\frac{1}{2} C_m h \alpha \Delta p \left( 3 - 4\nu + \frac{D-z}{|D-z|} - \frac{D-z}{\sqrt{R^2 + (D-z)^2}} - \frac{(D+z)(3-4\nu)}{\sqrt{R^2 + (D+z)^2}} + \frac{2R^2 z}{(R^2 + (D+z)^2)^{\frac{3}{2}}} \right) \quad (2.52)$$

Here  $C_m$  is the uniaxial compaction coefficient,  $\Delta p$  the change in pore pressure,  $R$  the reservoir radius,  $z$  the depth at which the displacement is computed,  $h$  the height of the reservoir and  $D$  is the depth of the nuclei or the central depth of the reservoir.

$$D = \frac{(D + \frac{h}{2}) + (D - \frac{h}{2})}{2} \quad (2.53)$$

To calculate the subsidence at the surface  $z = 0$  can be inserted into equation 2.52 resulting in equation 2.54.

$$u(z)_{surface} = 2C_m \alpha \Delta p (1-\nu) \left( 1 - \frac{D}{\sqrt{D^2 + R^2}} \right) \quad (2.54)$$

From equation 2.52 two factors can be defined:

$$f_3(x) = 1 - \frac{x}{\sqrt{R^2 + x^2}} \quad (2.55)$$

$$f_4(x) = \frac{xR^2}{(R^2 + (D+x)^2)^{3/2}} \quad (2.56)$$

With  $f_3$  the intra-reservoir vertical displacement at any depth can be determined:

$$u(z)_{res} = u(D) - C_m \alpha \Delta p f_3 \left( \frac{h}{2} \right) (D-z) \quad (2.57)$$

$$u(D) = \frac{u(D - \frac{h}{2}) + u(D + \frac{h}{2})}{2} \quad (2.58)$$

Important to note is that these equations relate to a ratio of  $R/D$ . Hence, compaction as well as subsidence are influenced by these parameters radius  $R$  and central depth  $D$ . This influence is described by introducing a geometrical factor  $rc(R/D)$ .

$$rc(R/D) = \frac{u(D)}{\Delta h} = \frac{3-4\nu}{2} f_3(2D) + f_4(D) \quad (2.59)$$

### 2.5.3. Initiation of fault reactivation: The failure criterion and failure reservoir pressure

Combining all this information, it is almost possible to solve equations 2.33 and 2.34 for  $\tau_{vh}$ , which is the only left unknown. The unknown term  $\tau_{vh}$  is defined as equation 2.44 up to a distance of  $0.1 * h$  from the fault. Farther away  $L_1 + L_2$  is replaced by the influence zone  $\Lambda_f$  which Scholz (2002) has suggested is related to the thickness of the reservoir  $h$  with a constant  $c$  as  $\Lambda_f = c * h$  (see section 5.3.1). With the help of the reservoir specific parameters  $rc$ , the uniaxial stress path  $\gamma_u$  and putting everything into relation to the thickness  $h$  of the reservoir the equation for  $\tau_{vh}$  can be reformulated to:

$$\tau_{vh} = G_f \frac{\Delta u}{\Lambda_f} = \frac{1}{2C} (\gamma_u rc \Delta p)_2 - (\gamma_u rc \Delta p)_1 \quad (2.60)$$

$$\gamma_u = \alpha \frac{1-2\nu}{1-\nu} \quad (2.61)$$

To determine if failure occurs on the fault, a failure criterion needs to be specified. Two different methods will be discussed here.

**Shear capacity utilization** (SCU) is defined as the fraction between the shear stress on the fault  $\tau_f$  over the maximum shear stress the fault can hold before failure  $\tau_{fail}$ . If this ratio becomes larger or equal one, failure occurs.

$$SCU = \frac{\tau_f}{\tau_{fail}} \geq 1 = \tau_{rel} \quad (2.62)$$

**Mohr-Coulomb criterion** (MC) gives an absolute difference between the shear stress on the fault  $\tau_f$  and the maximum shear stress the fault can hold  $\tau_{fail}$ . This means that if this difference becomes larger or equal zero, failure occurs.

$$MC = |\tau_f| - \tau_{fail} \leq 0 \quad (2.63)$$

$$MC_{risk} = \frac{|\tau_f| - \tau_{fail}}{|\tau_{f,i}| - \tau_{fail,i}} \quad (2.64)$$

Out of a perspective for applications such as risk analysis the MC criterion is a more useful tool as it can give a percentage estimate of risk increase. The SCU gives the impression that it can do this as well, however, it can only indicate if failure occurs or not, and not how close to failure the fault is. Equation 2.64 shows how to calculate the "risk" by looking at the ratio of the difference between shear stress on the fault  $\tau_f$  and the shear strength  $\tau_{fail}$  over that value of the initial state before depletion (marked with subscript  $i$ ). To illustrate this, figure 2.9 shows three different Mohr-Coulomb circles. The first one shows the initial stage of the reservoir and the two subsequent ones show different increasing stages of depletion. What can be seen is that for each stage the circle grows but that the value for  $MC$  stays the same. Table 2.1 shows the calculation of both criteria for the three different stages. From the calculation of the SCU it would seem as though the risk for reactivation is increasing, whereas in reality the difference stays constant, as is shown by the values for  $MC$ , which are all close to one. The closer this value is to zero, the larger the risk for failure.

Table 2.1: Table comparing both reactivation criteria with data from figure 2.9

	Initial state	First depletion step	Second depletion step
SCU	$0.37/0.51 = 0.72$	$0.63/0.79 = 0.79$	$0.85/1 = 0.85$
$MC_{risk}$	$\frac{0.37-0.51}{-0.14} = 1$	$\frac{0.63-0.79}{-0.14} \approx 1$	$\frac{0.85-1}{-0.14} \approx 1$

Instead of determining  $\tau_{rel}$  for each depletion phase, it would be more useful to directly calculate the failure reservoir pressure. Hettema (2017) formulated equation 2.65 for the calculation of the critical reactivation pressure. This is based on equations 2.66 to 2.72

$$p_i - p_{react} \leq \frac{K_{pe}(\sigma_v - p)_i - (\sigma_h - p)_i - S_0/q_2}{K_{pe} \left( \frac{\gamma_v}{2} - \alpha_1 \right) - \left( \frac{\gamma_h}{2} - \alpha_1 \right) + K_{dc} \gamma_{hv}} \quad (2.65)$$

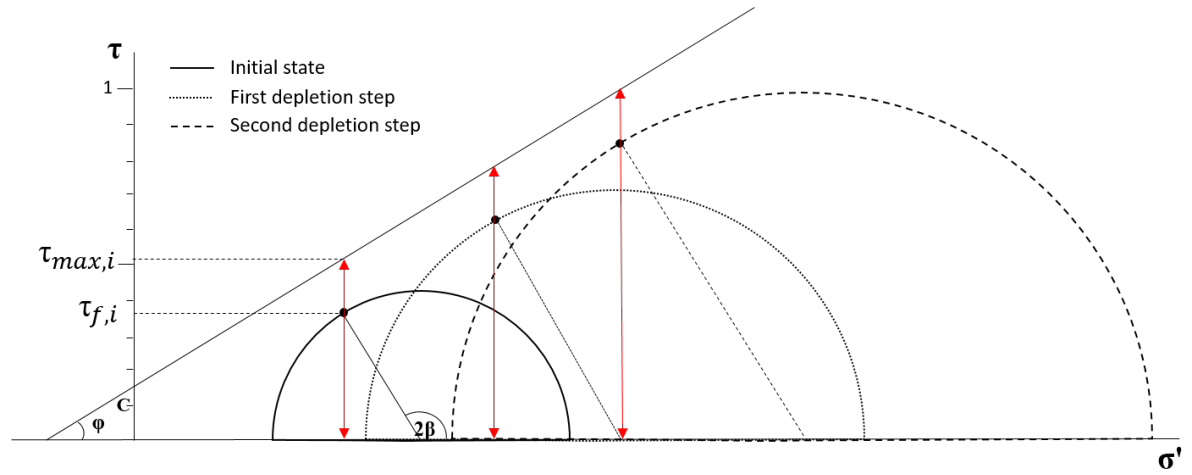


Figure 2.9: Systematic figure of a depleting system to illustrate differences between both fault reactivation criteria.

In which:

$$K_{pe} = \frac{\sin(2\beta - \varphi) - \sin \varphi}{\sin(2\beta - \varphi) + \sin \varphi} \quad (2.66)$$

$$K_{dc} = \frac{-2 \cos(2\beta) - 2\mu \sin(2\beta)}{\sin(2\beta) + \mu(1 - \cos(2\beta))} \quad (2.67)$$

$$\gamma_h = \left(1 - \frac{\pi}{4}e\right)\gamma_u \quad (2.68)$$

$$\gamma_v = \frac{\pi}{2}e\gamma_u \quad (2.69)$$

$$e = \frac{H}{2R} \quad (2.70)$$

$$\gamma_{hv} = \frac{\gamma_u}{2c} \left(\frac{f_3}{2}\right) \quad (2.71)$$

$$q_2 = \frac{\sin(2\beta) + \mu(1 - \cos(2\beta))}{2} \quad (2.72)$$

With these theoretical principles for the analytical calculation of the stress situation on a fault it becomes possible to assess the stability of a fault relatively quickly if correct estimates of parameters are present. Besides this, the approach provides a method to compare it to the simulations performed in this thesis. These theoretical principles can then allow us to relate the results of the sensitivity study back to the various parameters within them.

# 3

## Geological Background of the Netherlands

This chapter gives a short overview of the regional tectonic setting around The Netherlands and its paleogeographical development in text and illustrated by figure 3.2. It also provides a more precise description of the lithologies and their depositional environments (figure 3.7). A chronostratigraphic column of the time periods of interest for this project can be found in Appendix A figure A.2.

### 3.1. Tectonic setting and paleogeographical development

Starting in the Pre-Carboniferous 400 Ma ago, the Laurentian tectonic plate drifts further to the north-west and collides with Baltica-Avalonia, creating the Caledonian mountains and forming the large Laurussian continent (Doornenbal and Pagnier (2004)). The Appalachians and Scandinavian massifs are remnants of this orogeny.

During the Carboniferous, 400-300 Ma ago, the Variscan orogeny is initiated by the collision of Laurussia and Gondwana. This collision creates the Variscan mountain belt stretching from what is now southern Ireland through Belgium to Poland. A flexural foreland basin is created in the area where now The Netherlands is (figure 3.1). It is subject to extreme thermal and flexural subsidence (Kombrink (2008)). In the south-east of The Netherlands there is still evidence for this compression which can be seen in the form of thrust planes with a SW-NE strike. After the Variscan orogeny, at the border to the Permian, wrench faulting allows for intrusion of volcanic rocks causing regions of The Netherlands to be uplifted and eroded. The Groningen High belongs to one of these uplifted regions (Doornenbal and Pagnier (2004)).

In the following I follow the tectonic history as described by Plant et al. (2003). The Rheno-Hercynian Basin is filled with eroded Devonian and Carboniferous sediments during the Permian, 300-250 Ma ago. The development of new rifts during this time allows for rapid subsidence in the basins and thus the accumulation of large amounts of sediment. These systems were sometimes accompanied by the presence of volcanic rocks. The rift basins also played a crucial part in the deposition of the evaporitic sequences at the end of the Permian, forming the Zechstein formation. This formation plays a critical role in hydrocarbon trapping in large parts of Western Europe.

The continued rifting and drifting during the Triassic creates a sediment sequence of continental to brackish-marine red-beds in the Early Triassic and of marine carbonates and evaporites at the Late Triassic. The drifting phase causes a relative sea-level rise which can be seen in the larger extent of Triassic sediments compared to Permian sediments that are found in the Rheno-Hercynian Basin. Additionally, the Neotethys starts opening further to the south during this age, announcing the first of many rift events that define the geometries and structures of the North-Western European hydrocarbon province as we know it today.

In the Jurassic, 200 - 150 Ma ago, the break-up of Pangea starts due to the opening of the North Atlantic ocean. The North Sea rift system is part of this rift zone and thus the extensional regime which forms the large hydrocarbon provinces surrounding the various graben systems of North-Western Europe was created. The rifting causes a large marine transgression over wide areas forming marine deposits. In the Late Jurassic the collapse of the North Sea rift dome along with the changes in the regional stress directions due to the extensional stress regime, caused the form of the basin to change. This had direct influence on the source of clastic sediment input.

During the Cretaceous the opening of the South Atlantic causes the African plate to move northwards

with a slight anticlockwise rotation. Because of this, the Neotethys to the south begins to close, causing the microplates between the Eurasian and African plates to collide, marking the start of the Alpine orogeny.

During the Tertiary this convergence continues, creating a foreland basin north of the Alps in the Late Eocene which is filled with erosional sediment from the growing mountains. This compression causes a change in stress directions from N-S to NE-SW throughout large parts of Western Europe. Even though the central Alps are now showing signs of extensional tectonics these regions are still subject to the above described crustal tectonics and associated stress regimes at present day. A more detailed analysis of the subsurface stress regime is given by Mechelse (2017).

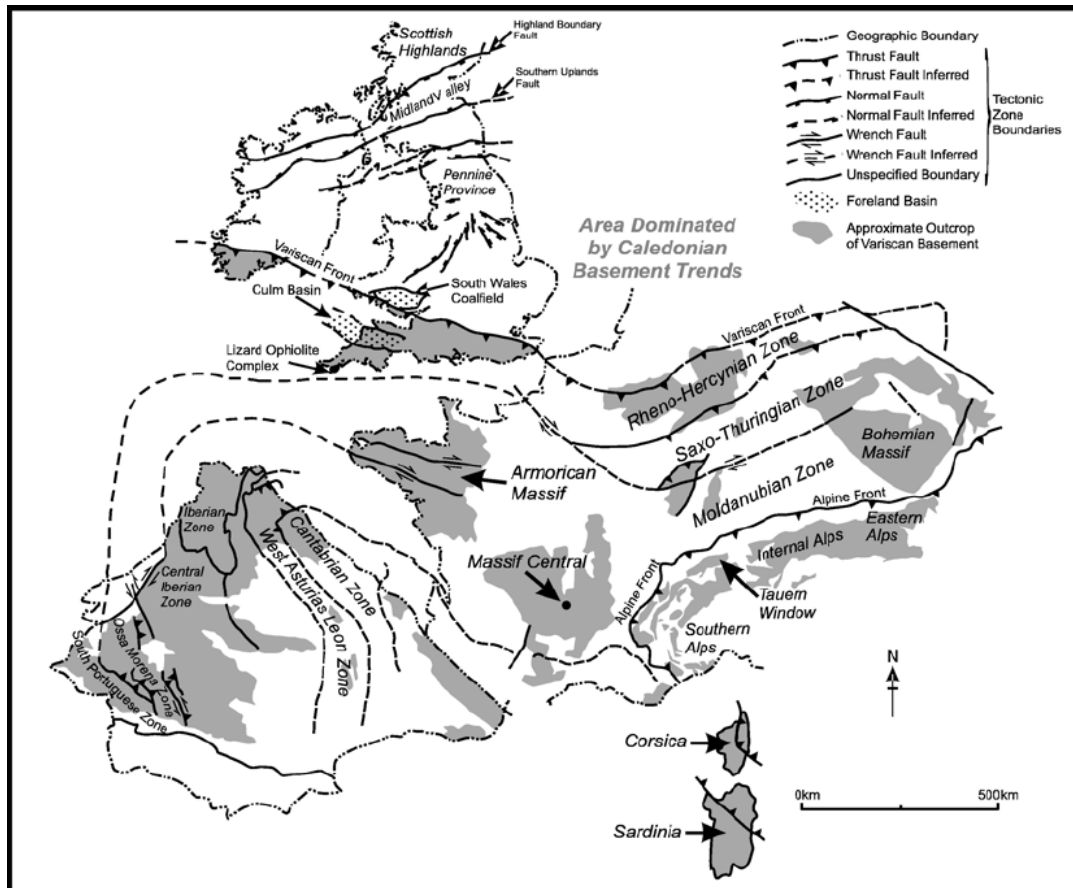


Figure 3.1: Variscan orogeny belt across western Europe

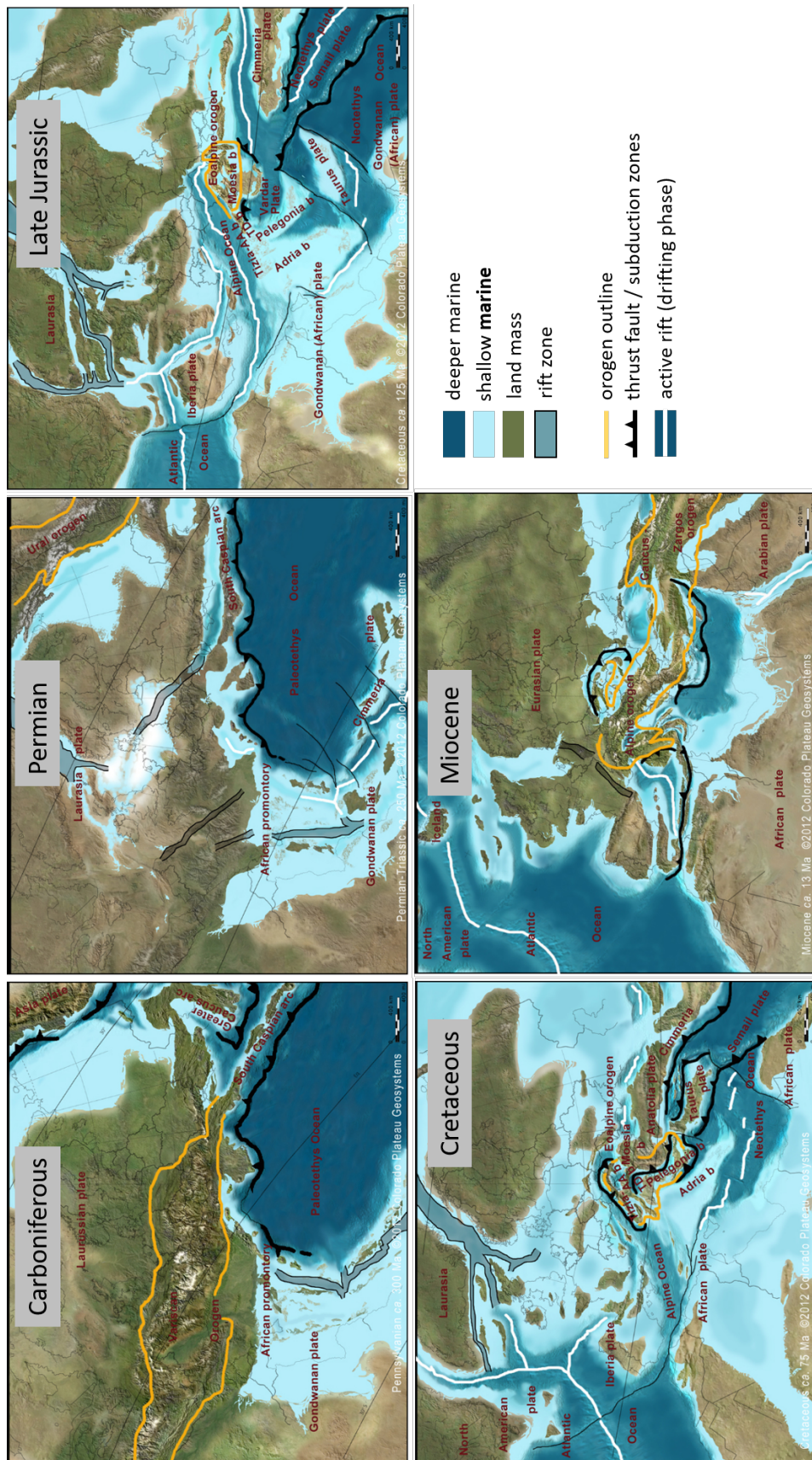


Figure 3.2: Time slices of Europe's tectonic history [20]

## 3.2. Lithologies

The formations that are used for the model are based on subsurface information from the Groningen gas field as more data is available in this region than in others. This makes it possible to create a generic model which is based on actual data. In the following sections the lithologies of the formations found in the underburden, overburden and the reservoir itself of the Groningen field are described. Figure 3.3 shows an overview of these formations.

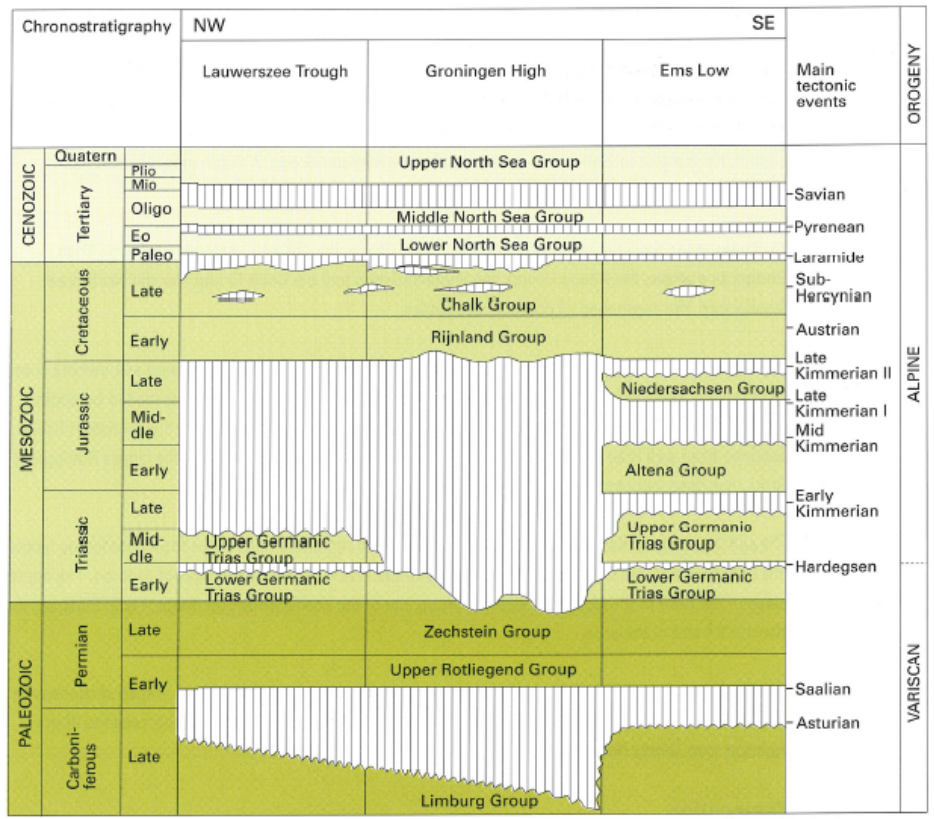


Figure 3.3: Stratigraphic column of the lithologies beneath the Groningen high.

### 3.2.1. Underburden

**Pre-Carboniferous:** These are the deepest known sediments in the Dutch subsurface. They were strongly deformed during the Caledonian orogeny and consist of metamorphosed shales, sandstones and quartzites and lie at large depth (> 5000 m).

**Carboniferous** The largest part of the underburden consists of Carboniferous sediments. They have a very large but varying thickness of up to multiple kilometers and consist of the Carboniferous (Dinantian) limestone group deposited in the Early Carboniferous followed by the Limburg group deposited disconformably over it. (Doornenbal and Pagnier (2004)) According to Doornenbal and Pagnier (2004) and Kombrink (2008) the influx of clastic sediment was stopped due to a rise in sea level in the Early Carboniferous and carbonate platforms started to form on shelves such as the Groningen High. In the troughs, which were thought to be partially starved due to the rapid subsidence (both thermal and flexural (Kombrink (2008))), more shaley sediments were deposited (Doornenbal and Pagnier (2004)). This depositional environment lasted for larger parts of the Early Carboniferous, depositing thick shaley layers, until the Variscan mountains started to rise in the Namurian. Due to the orogeny an increasing amount of clastic sediment was deposited in this basin (Collinson (2005)) and together with the regression of the ocean the environment transitioned to a more deltaic setting. This change marks the onset of the Westphalian in which the well known coal seams were deposited that were mined for many years in the south of The Netherlands and that source many gas

fields in the Dutch sectors, on- and offshore including the Groningen gas field (Van Buggenum and den Hartog Jager (2007)). Towards the end of the Westphalian and during the Stephanian dryer conditions caused the amount of coal seams to decrease (Besly et al. (1993)). The sediments of the Namurian and various stages of Westphalian form the Limburg group beneath the Groningen field. No Stephanian deposits are found due to erosion (TNO-NITG (1995)). Figure 3.4 shows the different formations within the Limburg group.

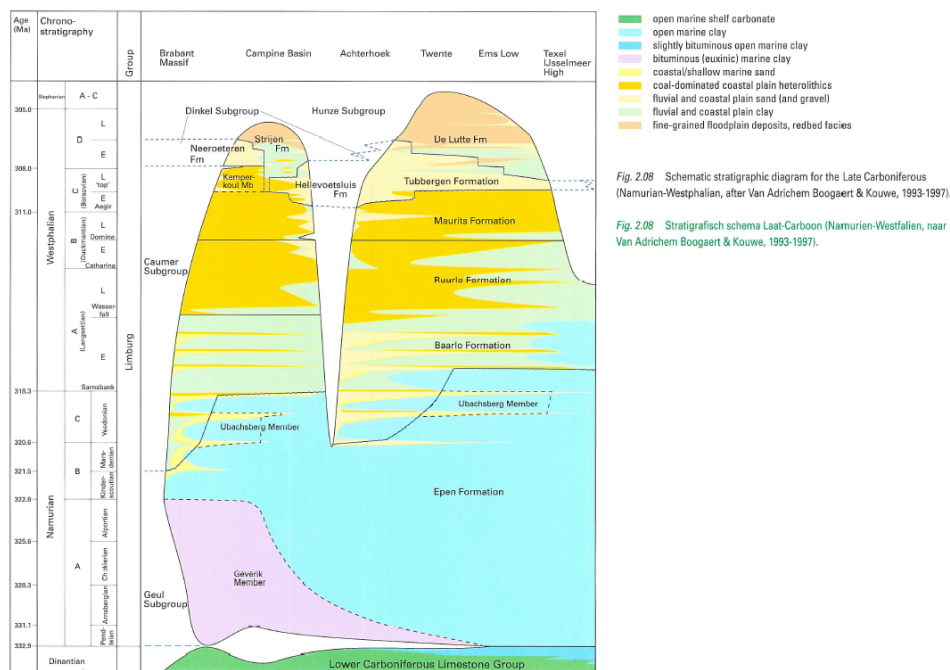


Figure 3.4: Stratigraphic column of the Carboniferous sediments beneath the Groningen High.

### 3.2.2. Reservoir

**Permian** Multiple tectonic phases at the beginning of the Permian caused large parts of the Limburg formation to be eroded again but also allowed for the further formation of troughs and highs. After a period of erosion, the increasingly dryer conditions and increase in sand-to-shale ratio created the deposits of the upper Rotliegend group. The youngest and sandier formations of this group are the upper and lower Slochteren formations that form the important reservoir formations for many fields in The Dutch sector of the North Sea. They are built from fluvial sandstones and conglomerates deposited in a desert wadi environment. These are replaced by aeolian sandstone and further towards the north by lacustrine deposits where the center of the Permian basin was as seen in figure 3.7. The lacustrine deposits in the basin itself are named the Silverpit claystone and the Silverpit Evaporite formations. They interfinger with the Slochteren formation and each time the climate became more humid - this meaning periods of high-water - the lacustrine environment moved southwards, thus covering larger parts of the northern part of The Netherlands in floodplain deposits. The largest of these high-stands are represented by the Ameland and Ten Boer claystone members. The Ameland member can be found in between the lower and upper Slochteren formations in the more northern areas of the Groningen field and the Ten Boer forms the top layer of the reservoir formation. The boundaries of these formations are often gradual, confirming the ideas on the depositional environment. Where the Lower Slochteren formation shows more conglomerates and is less well rounded the Upper formation becomes increasingly more homogeneous and better rounded towards the top until no more evidence for conglomerates is found and the amount of shale intercalations increases (TNO-NITG (1995)).

### 3.2.3. Overburden

**Late Permian Zechstein** The Zechstein forms the seal of the gas reservoir and consists of six different formations. Five formations each represent an individual evaporitic cycle (Z1 to Z5) and next to this there is also the Zechstein Upper-Claystone formation. The Zechstein was deposited all the way to the Brabant Massif in the south of the Netherlands and its thickness gradually increases towards the north. However, it varies

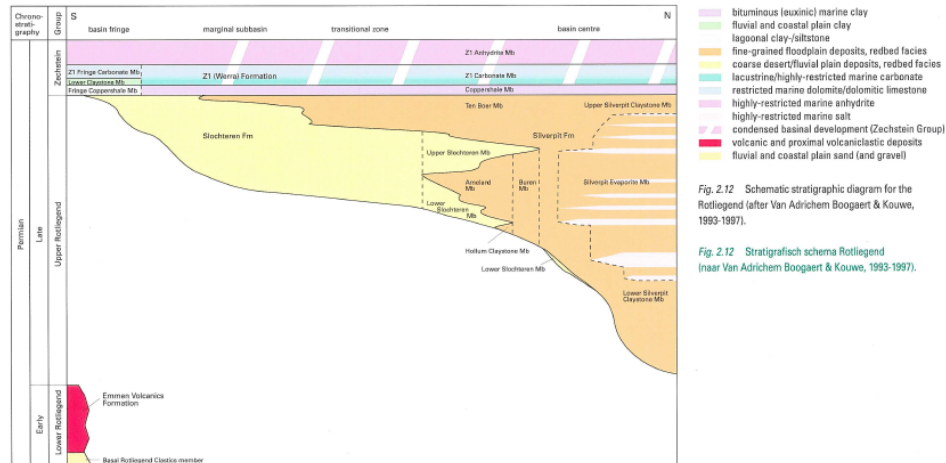


Figure 3.5: Stratigraphic column of the Permian sediments beneath the Groningen High.

greatly in thickness due to the forming of basins and highs at later stages, causing the salt to creep due to differential weight distribution. This causes the salt thickness to range from some tens of meters to over 2500 m in specific areas (TNO-NITG 1995). These thick evaporite sequences could be deposited thanks to the opening of a connection between the Barentsz Sea further to the north and the Southern Permian Basin. This connection was created due to rift formation in the North Atlantic and a sea-level rise caused by the melting of the Gondwanan ice cap (Doornenbal and Pagnier 2004). Due to the opening the basin was rapidly flooded but because of the arid climate and irregular influx from the arctic ocean it was possible for these evaporites to be deposited (TNO-NITG 1995).

Figure 3.6 shows a stratigraphic column of the different Zechstein cycles. The first sediment to be deposited under euxinic conditions was the Coppershale member (Taylor 2009). This was followed by a layer of Carbonate and Anhydrite. The Z1 formation has a relatively constant thickness of around 35 m throughout the field. The Z2 formation consists of a nearly complete evaporite cycle. Due to the large amounts of Halite present, the thickness varies greatly due to halokinesis. This rock-salt is the so-named Zechstein salt. Next to halite there are also thinner layers of carbonate and anhydrite. The Z3 member consists of the Grey Salt Clay, Carbonates, Main Anhydrite and again Halite. Within the Halite there are some thin layers of valuable K-Mg salts which are won by Nedmag B.V. in the north of The Netherlands. The thicknesses of each of these layers varies laterally but the Z3 formation forms the thickest layer of the Zechstein. The Z4 formation is not present everywhere in the Groningen field due to hiatus or salt domes. It consists of a thin layer of Red Salt Clay and Pegmatite Anydrite and is locally covered by up to 80 m of rock-salt. The last evaporite cycle formed the very thin Z5 formation which only covers the western half of the Groningen field. Overlying these cycles is an anhydrite claystone sequence which forms the Upper-Claystone Formation.

**Triassic** In this period extremely uniform basin subsidence of the Southern Permian basin occurred. Therefore the basin is also named the Permo-Triassic basin. Due to the continued rifting in the Atlantic and the opening of the basin to larger instream of fluid the depositional environment changes from continental lacustrine to shallow marine or from deltaic coastal and shallow marine setting. The Triassic sediments are partially not present above the salt structures in the Dutch subsurface. However the sediments consist of brackish-marine red-beds in the Early Triassic and of more shallow marine limestone and evaporites in the Later Triassic. They also form potential reservoir rocks.

**Jurassic** In the Jurassic the rifting causes the entire region up to the Brabant massif to be subject to marine conditions. The most noteworthy about the Jurassic period is the deposition of the Posidonia shale in large parts of Europe during Toarcian in which there was a period of anoxic conditions. The Posidonia shale serves as an important source rock throughout Europe and in many other regions around the world. The Jurassic is not present above the Groningen field.



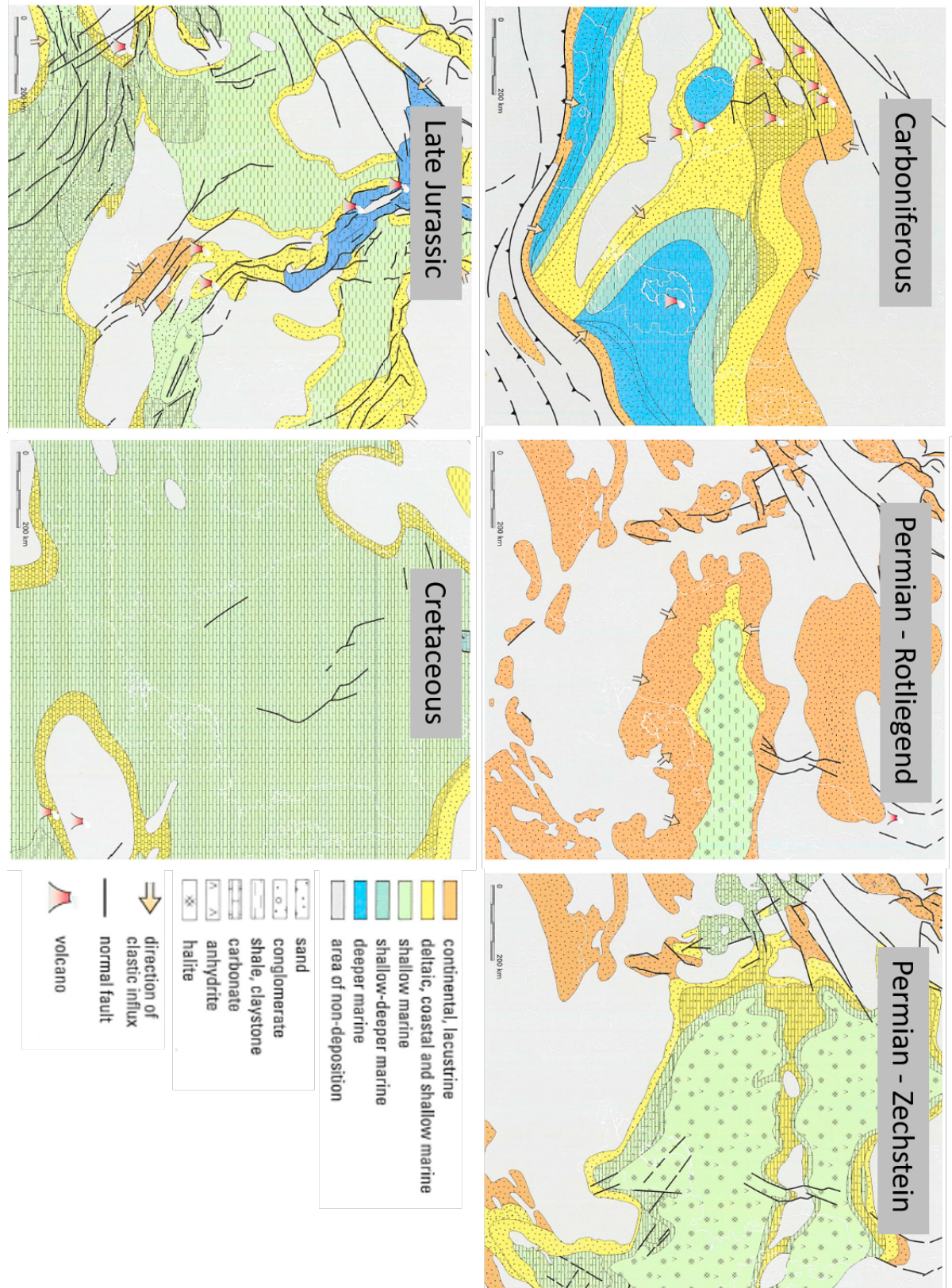


Figure 3.7: Time slices of North Western Europe's depositional environments Doornenbal and Pagnier(2004)

# 4

## Geomechanical Model

### 4.1. Software - Plaxis 2D 2017

The software used to perform the geomechanical modelling is Plaxis 2D 2017, a two-dimensional finite element geotechnical software. From here on referred to as Plaxis. It has been mainly developed to be used for shallow subsurface geotechnical applications such as deformation and stability of soils and groundwater flow. Plaxis was chosen for this thesis because of its theoretically sound computations of non-linear finite element computations, its robustness and user-friendliness.



The steps to building a geomechanical model with Plaxis are:

- Choice of model and mesh type
- Building of individual elements of the model (soil polygons, interfaces, ground water level etc.)
- Choice of soil model & input of material parameters
- Defining boundary conditions & meshing
- Definition of various modelling phases
- Running the model
- Quality control and gathering of output data

Plaxis allows for both *axisymmetric* as well as *plane strain* calculations to be performed. An axisymmetrical model is more representative of reality as it simulates a disc-shaped reservoir with a certain radius. However, introducing a fault in an axisymmetrical model implies a circular fault at the reservoir boundary, which is not something representative of reality. Figure 4.1a shows the schematic representation in a cross-section of an axisymmetric model. While using the software only one half will be shown, the other side is identically mirrored. The other option is a plane strain model, which assumes the third dimension (perpendicular to the plane of sight, denoted by  $z$ ) to be an endless representation of the 2D image (figure 4.1b). This means all elements in the strain tensor that contain a  $z$ -element are set to zero, reducing the tensor to 4 elements. Depth in Plaxis 2D is hereafter represented by the  $y$ -variable.

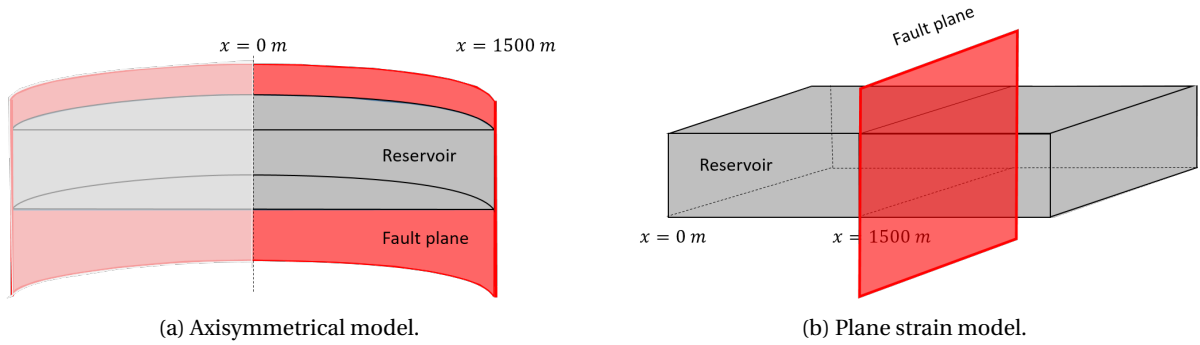


Figure 4.1: Schematic of an axisymmetrical and a plane strain model.

Plaxis offers a choice out of multiple soil models such as the *Hardening Soil*, the *Soft Soil* or the *Hoek-Brown* models among others. For application to deeper problems as in this thesis, the *Mohr-Coulomb model* or the *Jointed Rock model* are most applicable. It is assumed that no significant layering and anisotropy is noticeable in the layer of interest, the reservoir. So the *Mohr-Coulomb model* was used for all layers. It can model linear elastic perfectly plastic behaviour of materials and interfaces. Plaxis [5] recommends the use of the *Mohr-Coulomb model* as a first approximation to soil behaviour. This is because actual soils, behave non-linearly when subjected to larger changes in stress or strain. As the models including non-linearity cannot cope with deeper application and the soils we are dealing with are well consolidated, we assume the *Mohr Coulomb Model* to be representative enough for this situation. More information of the theoretical background and implementation of this model within Plaxis can be found in the various Plaxis manuals [5].

## 4.2. Geometry - Reservoir setting<sup>1</sup>

The geometry of the model is based on the simple geometrical aspects of a typical hydrocarbon field as it can be found in the Dutch subsurface. In section 3 the tectonic setting of the Dutch subsurface was described. As the research question was formed based on the problems around subsidence and seismicity in Groningen the geomechanical model and its properties are based on that specific part of the Dutch subsurface. The Groningen reservoir is crossed by various normal faults as is to be expected in an extensional regime. As mentioned in Kortekaas and Jaarsma (2017) the fault angles and offsets are known to range from 58.2 - 90°. The distribution of fault angles can be seen in figure 4.2. Fault throw was chosen as listed in table 4.1. It shows the range of these values along with the range for reservoir thickness also obtained from that dataset.

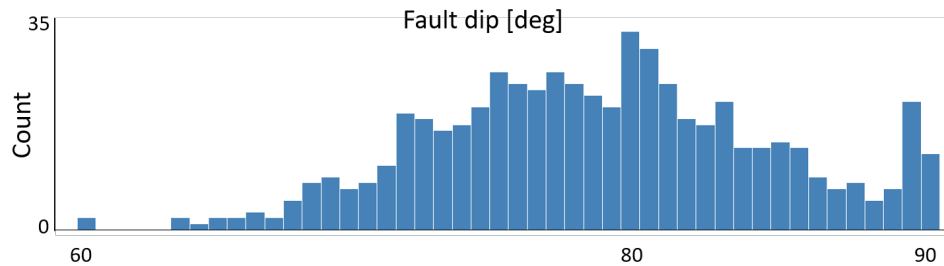


Figure 4.2: Distribution of average fault dips after Kortekaas and Jaarsma (2017).

Table 4.1: Range of fault dips, throws and reservoir thickness

	Dip angle	Throw [m]	Reservoir thickness [m]
min	57.88	0	100
max	90	400	350
average	79	30	200

<sup>1</sup>Information in this section were changed due to confidentiality reasons.

Figure 4.3 shows a schematic overview of the subsurface as modelled in Plaxis. The model dimensions are  $4\text{ km}$  deep with the reservoir top at  $y = -2800\text{ m}$ . The reservoir thickness is chosen to be  $200\text{ m}$  thick. The model is  $3\text{ km}$  wide, the fault is located in the middle (at  $x = 1500\text{ m}$ ) and propagates from some distance above the reservoir to multiple hundreds of meters below it. A more detailed explanation of why these general dimensions are valid can be found in section 4.4. The fault is modelled as an interface element. This means that it consists of pairs of nodes which each have the possibility to differential displacement. In this way slipping and gapping can be modelled correctly [5]. The interface was modelled in such a way that the pressure within the fault is the same as in the non-depleting side of the reservoir as this resulted in quicker fault failure.

The model contains an overburden, reservoir and underburden, all of them homogeneous and with the same material properties. The input parameters for this material are based on properties of a typical Rotliegend reservoir obtained from data or literature. The reason why the entire model is homogeneous is because the goal is to understand the mechanism of fault failure initiation. To do this it is necessary that the simulations can be compared to an analytical approach. The analytical approach can only work with homogeneous rock conditions, which therefore set the constraint for the simulated models.

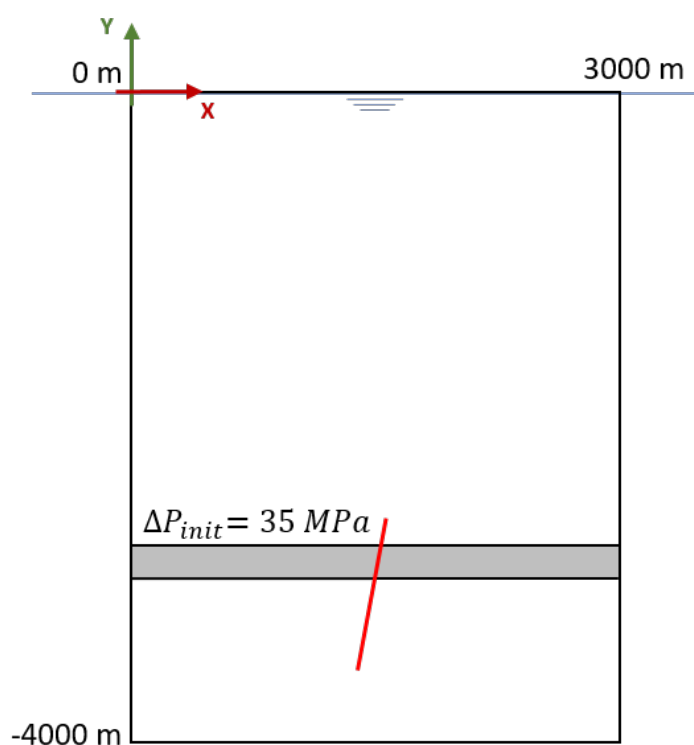


Figure 4.3: Model dimensions with homogeneous rock properties resembling the Slochteren formation. Reservoir top is found at  $-2800\text{ m}$  depth and is crossed by a fault which continues in the over- and underburden for a certain distance

From the values of the real data set around 20 different geometries were chosen to run simulations on to assess fault failure behaviour. The following list shows the different variations of the geometries and in Appendix A figure A.3 shows a schematic overview of all geometrical variations.

Table 4.2: Differences in varied geometries of the reservoir and fault.

Geom. parameter	Values
Reservoir radius [m]	500, 1000, 3000
Reservoir thickness [m]	50, 100, 200, 300
Fault angle [deg]	60, 70, 79, 90, 101, 120
Fault throw [m]	0, +30, -30, +100, -100, + res. thickness, -res. thickness

### 4.3. Input Data - Geomechanical, Strength Parameters<sup>2</sup>

The *Mohr-Coulomb* model which was chosen as soil model requires the following input to work correctly:

- Specific unsaturated weight  $\gamma_{unsat}$ ,
- specific saturated weight  $\gamma_{sat}$ ,
- void ratio  $e$ ,
- Young's modulus  $E$ ,
- Poisson's ratio  $\nu$ ,
- cohesion  $C$ ,
- friction angle  $\varphi$  and
- stress ratios  $K_{0H}$  and  $K_{0h}$ .

The specific unsaturated weight can be estimated from the density of the Slochteren sandstone  $2200\text{kg}/\text{m}^3$  (or  $22\text{kN}/\text{m}^3$ ). With an average porosity of 16% which translates to a void ratio of 0.19 (Core Plug database EBN) the specific saturated weight becomes around  $24\text{kN}/\text{m}^3$ .

Geomechanical parameters are estimated from literature on similar formations. From this the dynamic Young's modulus and Poisson's ratio have been calculated with the following equation from Fjær et al. (2008):

$$E_{dyn} = \frac{\rho v_s^2 (3v_p^2 - 4v_s^2)}{(v_p^2 - v_s^2)} \quad (4.1)$$

$$\nu_{dyn} = \frac{v_p^2 - 2v_s^2}{2(v_p^2 - v_s^2)} \quad (4.2)$$

However, the dynamic values do not represent reality as they should so they need to be transformed into static values to account for effects related to the porosity. According to Eijs et al. (2006) Eissa and Kazi (1988) found the best correlation between dynamic and static:

$$E_{stat} = 0.64E_{dyn} - 0.32 \quad (4.3)$$

Inserting average estimated values for the Slochteren formation this gives:

$$E_{dyn} = 30 \text{ GPa}$$

$$E_{stat} = 20 \text{ GPa}$$

$$\nu_{dyn} = 0.2$$

Porosity has a large effect on the geomechanical parameters is illustrated in figure 4.4 (Lele et al. (2015)). For the Slochteren reservoir, data on the compaction coefficient  $C_m$  is available in the technical addendum for "het Winningsplan" (NAM (2013)). Figure 4.5 shows the relation of the compaction coefficient to porosity. Assuming an average porosity of 16% the compaction coefficient is around  $10^{-4} [\text{MPa}^{-1}]$ . For the same average porosity value it can be seen that the Young's modulus becomes  $15 \text{ MPa}$  and the Poisson's ratio around 0.15. This is lower than what was calculated previously with  $\nu_p, \nu_s$  data.

Besides the geomechanical parameters, the strength parameters of cohesion and friction angle are also required for the geomechanical calculations. These values are quite hard to measure so rough estimates from similar formations were taken as listed in ? ( ? ) and Fjær et al. (2008). From this it was decided to take a cohesion of the intact rock was around  $C = 5 \text{ MPa}$  for the Slochteren sandstone and the internal friction angle  $\varphi = 30^\circ$  (for NAM (2014)<sup>3</sup>).

The initial reservoir pressure along with vertical and horizontal stress gradients are taken from Wassing et al. (2016):

- $p_{initial} = 35 \text{ MPa}$
- vertical stress gradient =  $0.022 \frac{\text{MPa}}{\text{m}}$

<sup>2</sup>Information in this section were changed due to confidentiality reasons.

<sup>3</sup>Confidential data

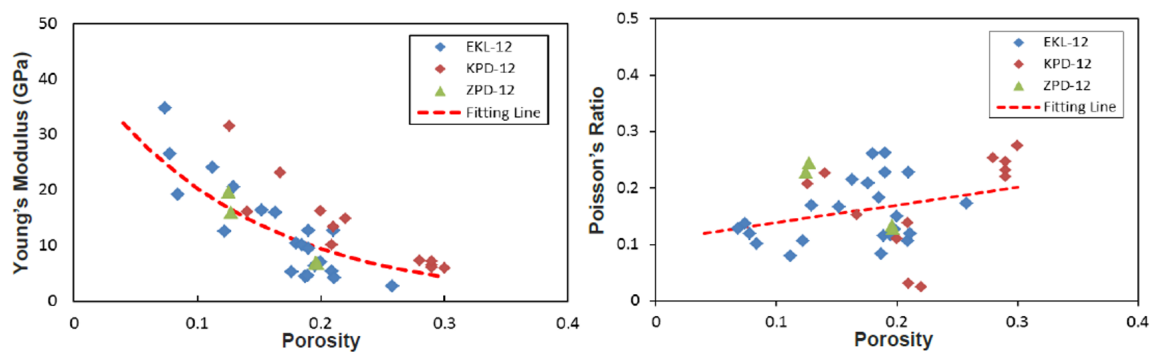


Figure 4.4: Dependency of Young's modulus and Poisson's ratio on porosity. Measured on cores of the Slochteren reservoir. (Lele et al. 2015)

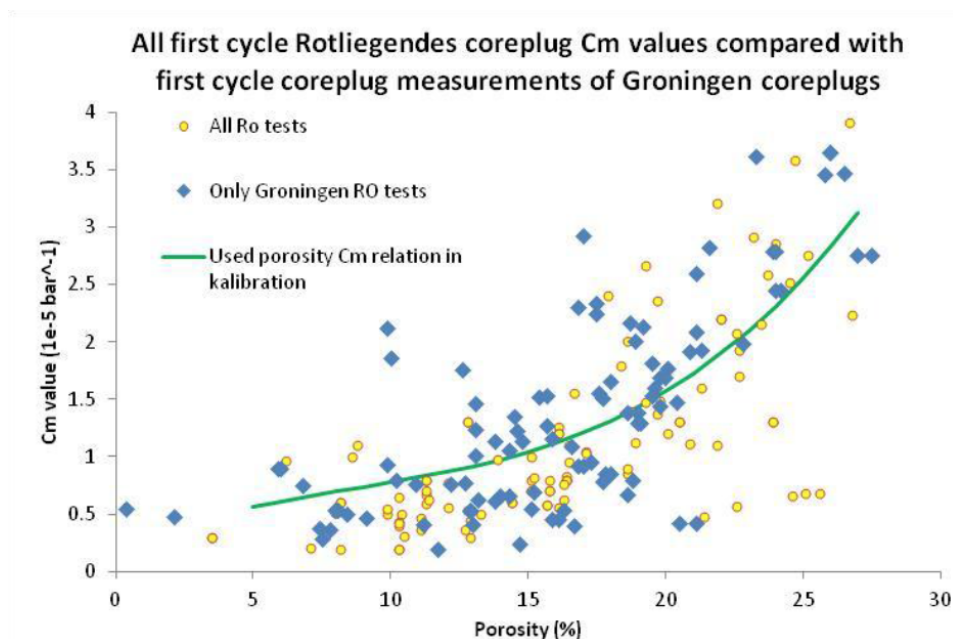


Figure 4.5: Dependency of compaction coefficient on porosity. Measured on cores of the Slochteren reservoir. (Lele et al. (2015))

- min. horizontal stress gradient = max. horizontal gradient =  $0.016 \frac{MPa}{m}$
- hydrostatic gradient =  $0.011 \frac{MPa}{m}$
- gas gradient =  $0.0015 \frac{MPa}{m}$

Therefore,  $K_0 = 0.7$  as suggested by Roest and Kuilman (1994).

The fault material is assumed to have the same stiffness and Poisson's ratio as the neighbouring soil but cohesion is set to zero as to represent a pessimistic case of a fault with no cohesion (one in which failure will occur quicker). Also the friction angle is set slightly lower than that of the soil itself at  $25^\circ$  as this part of the rock has already experienced failure once before.

For each geometry in table 4.2 the four rock and fault strength parameters were varied. These are the Young's modulus  $E$  and Poisson ratio  $\nu$  of the reservoir rock and fault as well as the fault strength parameters cohesion  $C$  and friction angle  $\varphi$ . Table 4.3 shows the ranges and amount of variations performed for each geometry.

Table 4.3: Range of varied rock and fault strength parameters

Rock / Fault strength parameter	Base	Min	Max	Steps
$E$ [GPa]	15	5	25	9
$\nu$	0.15	0.1	0.3	6
$C$ [MPa]	0	0	10	5
$\varphi$ [deg]	25	15	40	9

#### 4.4. Boundary conditions, meshing & model validation

To determine if the model dimensions as described above will not influence the results, the influence of the boundary conditions are tested. The exact steps of how the boundary conditions were validated can be found in Appendix A section A.3. The analysis resulted in the conclusion that a model with the dimensions described above can be used without consequence for the results. General conclusions from this analysis are that there is no difference between using a plane strain or axisymmetrical model. However, there is one limiting factor, the numerical *Virtual Interface Thickness (VIT)*, which restricts the size the model can have. This limitation comes from that Plaxis is generally not applied to areal domains of this size and that the VIT is linked to the general dimensions. This means that if the general dimensions are large, so is the VIT. This factor directly influences the elasto-plastic behaviour of the fault and surrounding rocks. Therefore it is necessary to make sure its value stays realistic.

After these tests on general model behaviour, meshing can continue. The mesh elements consist of 15-node triangular elements and Plaxis has an automatic meshing function in which local refinement of soils or interfaces can be manually selected. The soil polygons of the reservoir as well as the fault were refined to ensure a fine mesh at the locations of interest. That is, where the largest changes in stress and displacements were expected. The total mesh has around 34334 soil elements which is equivalent to 276444 nodes. This translates to a node spacing of around 80cm between nodes along the fault.

#### 4.5. Execution of the Simulations

Taking into consideration the desired boundary conditions and restrictions enforced by the software, it can be concluded that a model as seen in figure 4.3 would yield the best results for the analysis on the mechanisms leading to fault reactivation. However, when looking at compaction or subsidence, a larger, axisymmetrical model would provide more complete and representative results.

Compaction in the reservoir is simulated by decreasing pore pressure in the reservoir on the left side of the fault in steps of 2.5 MPa starting from the initial reservoir pressure 35 MPa to 5 MPa. This results in 12 different so-called phases plus an initial phase. The pore pressure on the right hand side of the reservoir is set to the hydrostatic pressure of that depth. Hence, the modelled fault is a sealing (boundary) fault with no permeability. The interface was chosen to maintain the pressure of the non-depleting side as this resulted in a higher sensitivity to fault failure.

After running the simulations a visual quality control on the results is performed. In the case that no errors have occurred and everything seems to be calculated correctly, data is exported for further analysis. Mainly data on the fault is exported. Values of the following parameters are looked at:

- Phase respectively the Pore Pressure
- $X$  - coordinate
- $Y$  - coordinate
- $U_x$ : Displacement in  $x$ -direction (horizontal)
- $U_y$ : Displacement in  $y$ -direction (vertical)
- $\tau$ : Shear stress on the fault
- $\tau_{rel}$ : Relative shear stress on the fault
- $\tau_{max}$ : Maximum shear stress (fault strength)
- $\sigma_n$ : Normal stress on the fault
- $\sigma'_n$ : Effective normal stress on the fault

## 4.6. Uncertainty

In the Finite Element Model used in Plaxis the most restrictive assumption is that the soil and rock behaves in an linear elasto-plastic manner according to the *Mohr-Coulomb* failure criterion. It is assumed that the material behaves in solely this manner, however, this is not a given as soils or rocks behave non-linearly under large strains.

If this first assumption were indeed correct the next limitation of the model is that only the initiation of failure can be accurately modelled. For this, a fully dynamic model would be needed in which also factors such as the change from static to dynamic friction angle is integrated. This limited the reach of the results this research could produce. Still a lot of research is needed to find out how this change actually happens. It is still unknown if the friction angle decreases in an instant, linear or non-linear manner as shown in figure 4.6.

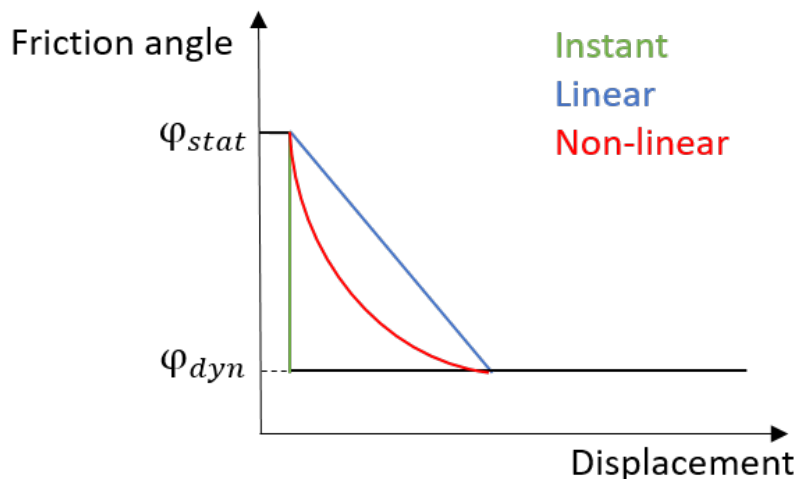


Figure 4.6: Change from static to dynamic friction angle. It is unknown if this decrease occurs instantly, linearly of a certain length of displacement or in a non-linear manner.

Other simplifications within the model were that the Biot-alpha factor was set to one for simplicity as well as for reasons of software limitations. Again here this is not representative of real rock formations as the Biot alpha is  $< 1$  for porous media.

Another uncertainty, which creates large differences in the results for fault failure is which pore pressure is assigned to the fault. In Plaxis it is possible to either assign the pressure of the depleting side or the non-depleting side. As more severe effects, so quicker failure, is achieved when the fault is assigned the non-depleting pressure, all simulations were run with this assumption.

Besides this the material properties that are entered for the reservoir, fault, over- and underburden are roughly estimated from limited data from lab experiments and literature. Additionally, the entire model is homogeneous. Knowing that on geological scale the lithology can change every few centimetres this is surely not a correct representation of reality. Heterogeneity could have both a positive or negative effect on rock or fault stability. This should be further investigated. Also the interaction between two rock formations with entirely different properties could bring good results.

This shows the importance of estimating the properties correctly. So when performing analysis of the risk of fault reactivation in a certain reservoir, even small amounts of uncertainty can lead to entirely different results. In chapter 5 the differences in results for small changes in parameter choice can be seen. The analysis in this thesis shows that if one is able to correctly estimate these properties, the failure criterion could be much better assessed.

Also the range of rock and fault parameters used for the variations were based on parameters of the Slochteren reservoir formation in the Dutch subsurface. The largest limitation here is that the values assigned to the shear modulus are in a rather small range. This means that if in a real case lithologies are present which are not similar to these type of sandstones the effects of shear modulus variations might have a larger effect than it now seems to have. The results are to be found in chapter 5 but to see how a large the influence of the shear modulus is more simulations would need to be run. Simulations performed by van den Bogert (2015),

however, show that even for large values, it does not have a large influence on the failure pressure.

# 5

## Analysis and Interpretation of Fault Failure Behaviour

In this section the results from the simulations as well as the insights gained by comparing them with the analytical approach are presented, analysed, interpreted and discussed.

### 5.1. The depleting reservoir

To get an idea of the response of the geomechanical model, an initial test was performed based on the present depletion of the Groningen field. Data in "het Winningsplan" from NAM (2013) records the reservoir pressure and the corresponding amount of subsidence. With these initial models a depletion of 20 MPa was simulated and the corresponding results of compaction in the reservoir estimated (Appendix A, figure A.7).

The driving force of a depleting reservoir is the change in pore pressure  $\Delta P$ . Figure 5.1a shows the pore pressure at different stages of depletion. The pressure above ( $> -2800m$ ) and below ( $< -3000m$ ) the reservoir are equivalent to the hydrostatic pressure at those depths. Only within the reservoir itself a pressure drop is simulated as seen in figure 5.3. Figure 5.3a shows the initial pressure before depletion and figure 5.3b after 20 MPa depletion. As a response to the pressure drop, compaction occurs within the reservoir. This causes the top of the reservoir to move downwards and the bottom of the reservoir to move slightly upwards. Looking at this effect 10 m away from a vertical fault ( $x = 1490m$ ) as shown in figure 5.1b, a small upwards movement can be seen. Throughout large parts of the reservoir this effect is constant. So when looking at figure 5.4, which corresponds to the state of depletion in figure 5.3b, we can see a negative vertical displacement of the top of around  $-22\text{ cm}$  and at the bottom a positive vertical displacement of up to  $6\text{ cm}$  in large parts of the reservoir. Closer towards the boundary fault the behaviour changes and the displacement becomes less extreme. A compaction of  $22\text{ cm}$  lies in a similar range as the findings of NAM (2013).

A short note on subsidence at this point: Figure 5.4a shows that the compaction of the reservoir propagates through the overburden causing substantial subsidence at the surface. However, the amount of subsidence is not equal to compaction. Multiple factors have an effect on the surface response to compaction. For a more complete physical explanation of this relationship and what the effects of structures in the subsurface have on subsidence, see thesis William Hazel (Hazel (2017)).

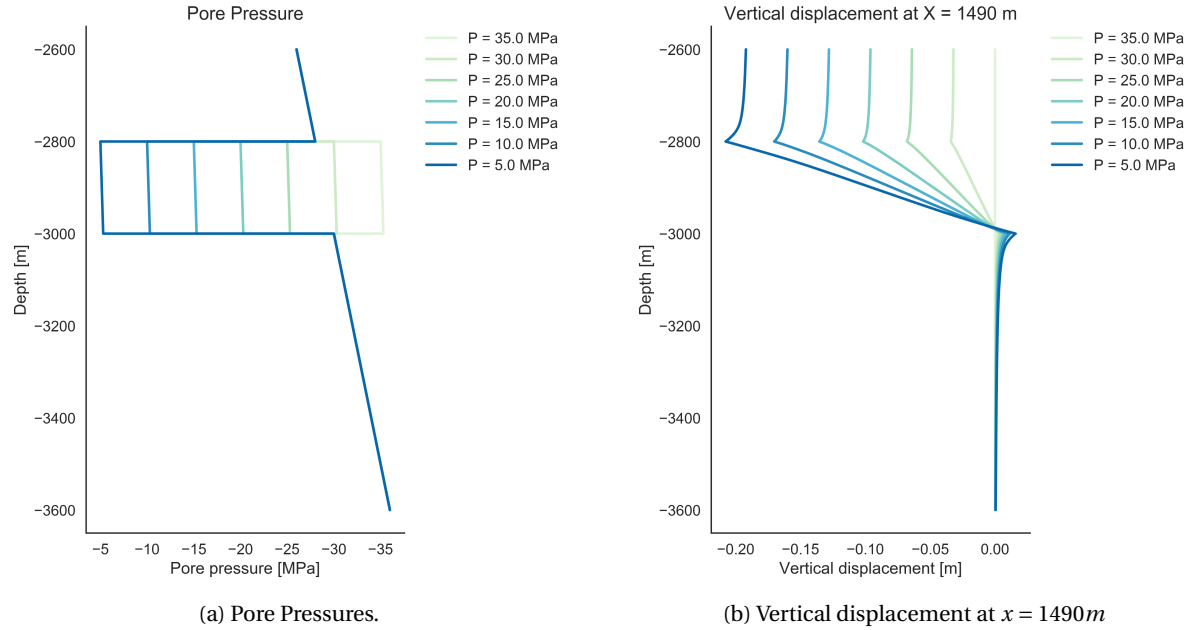


Figure 5.1: Change in pore pressure and the vertical displacement within the depleting reservoir at  $x = 1490m$ .

As already mentioned above, the vertical displacement seen in figure 5.4b becomes less closer to the fault. This means that while through large parts of the reservoir uniaxial strain conditions are valid, closer towards the fault this is no longer the case. This can also be seen in figure 5.5 which shows the horizontal displacement in the reservoir. Especially large changes in horizontal displacement over short distances can be seen close to the fault. In these regions it is possible to calculate the vertical displacement with the help of "Hankel-Lipschitz integrals" by Eason et al. (1955) as was also done by Geertsma (1973). This can lead to exact calculations of the displacement near a fault and thus to precise calculations of the shear stress on the fault under the assumption of linear-elastic behaviour. Figure 5.2 shows the typical vertical displacement of the top and base of a depleting reservoir with a vertical boundary fault. Even though there is no pressure drop in the non-depleting side, it also shows a negative vertical displacement and does not simply remain in its initial state. Another results can be gained from this plot. Geertsma (1973) claimed that the relation of the difference in vertical displacement of the top and bottom of the reservoir  $\Delta u_z$  over Compaction  $C_m h \Delta p$  is equal to 1.

$$f_3 = \frac{\Delta u_z}{C_m h \Delta p} = 1 \quad (5.1)$$

Hettema (2017) derives that this assumption is not valid near the fault. The simulation results support this and find that  $f_3$  is slightly below 1 near the fault. This has an influence on the calculation of the displacements and stress on the fault.

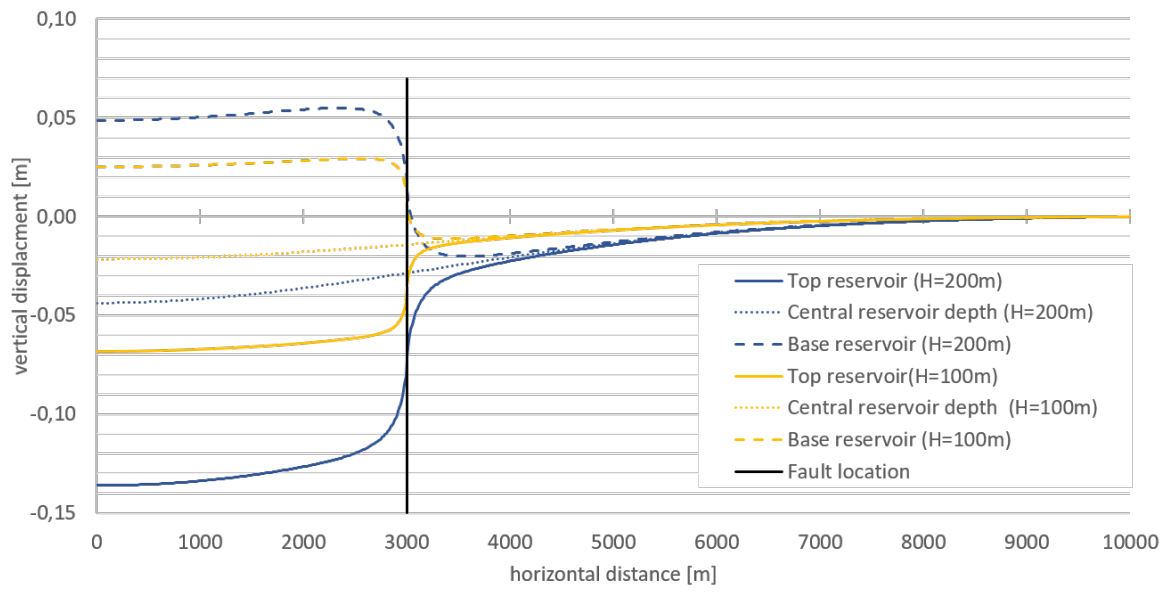


Figure 5.2: Vertical displacements profiles of top, base and center of a reservoir with thickness  $h = 100m$  and  $h = 200m$ .

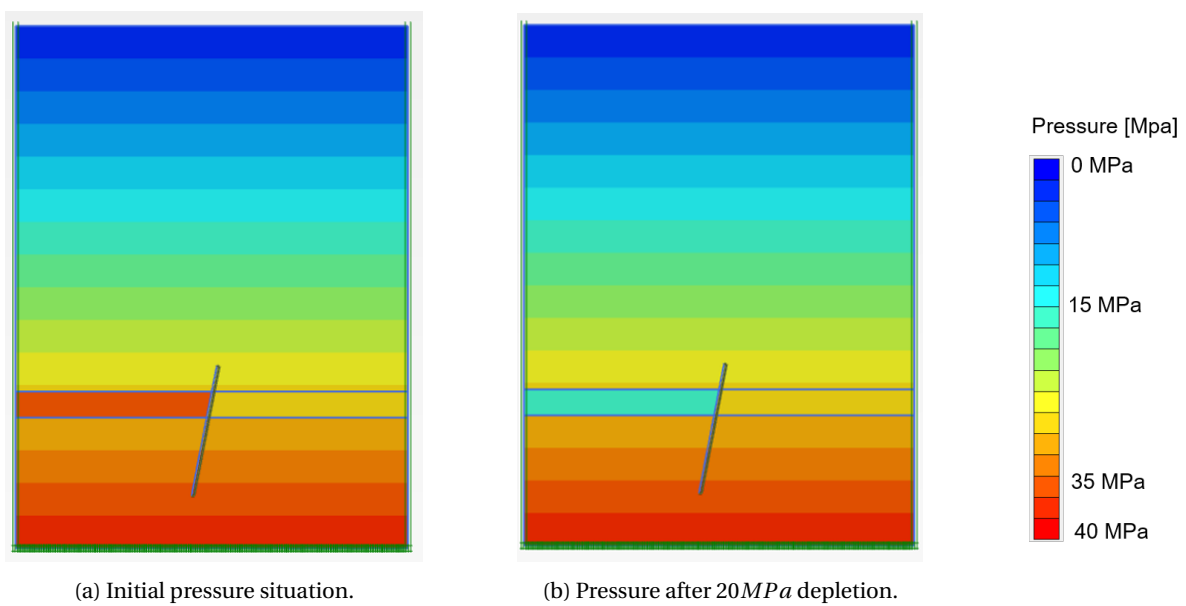


Figure 5.3: Pressures within the geomechanical model at initial state and after 20 MPa depletion.

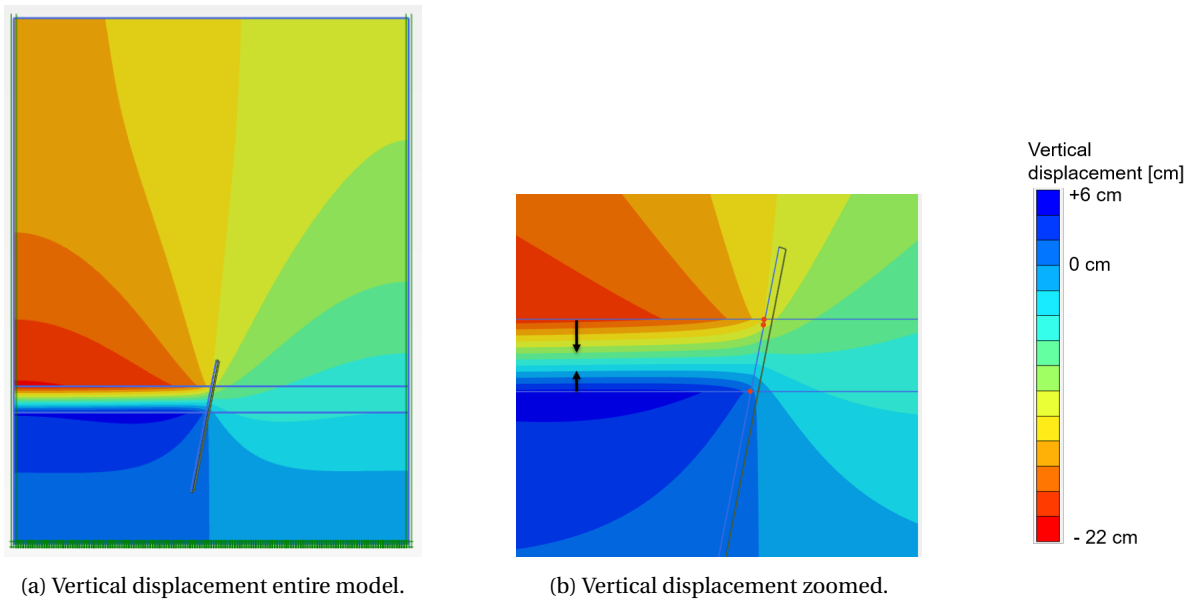


Figure 5.4: Vertical displacement of the reservoir and the surrounding formations after 20MPa depletion.

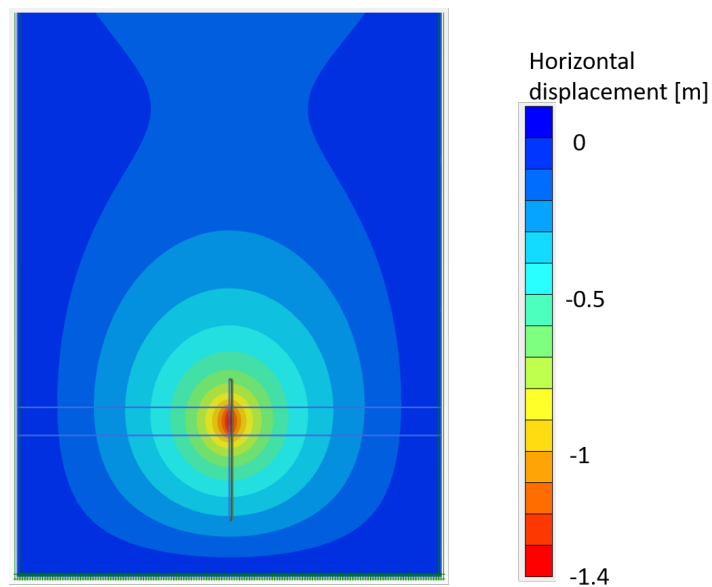


Figure 5.5: Horizontal displacement of the reservoir and the surrounding formations after 20MPa depletion.

Besides this directly visible effect of compaction, the vertical displacement causes an increase in shear stress  $\tau_f$  on the fault, as described in equation 2.34. Figure 5.6a shows what this looks like for the various drops in pressure within the reservoir with a vertical fault. It can be seen that the shear stress increases within and around the reservoir until a certain reservoir pressure when the shear stress "drops back" to a lesser value. Also interesting to notice is the difference in sign; the shear stress can have positive and negative values. At the top the values are negative and at the bottom positive. The sign does not affect if failure occurs so the absolute value of  $\tau_f$  can be used to assess this. Another thing to note is that in the middle of the reservoir section there is no shear stress on the fault. For a fault with a shallower angle this point of zero shear stress moves downwards in the reservoir (Appendix A figure A.8).

The shear stress on the fault can be translated into the relative shear stress  $\tau_{rel}$  by dividing the shear stress by the fault strength  $\tau_{fail}$  (equation 2.62). Figure 5.6b shows this for the vertical fault with the shear stress as in figure 5.6a. In all cases observed the relative shear stress reaches 1, showing that failure occurs at the top

of the reservoir.

From this point on, all analysis is done for the node on the fault at the top of the reservoir.

Plotting the relative shear stress for each depletion step (figure 5.7) it becomes clear at which pressures failure first occurs on a fault. Figure 5.7 shows this for all runs for a fault of 90° in which the Poisson's ratio  $\nu$  was varied. By interpolation it was possible to determine the point at which the relative shear stress becomes one. The pressure corresponding to that point is the pressure at which the fault fails first.

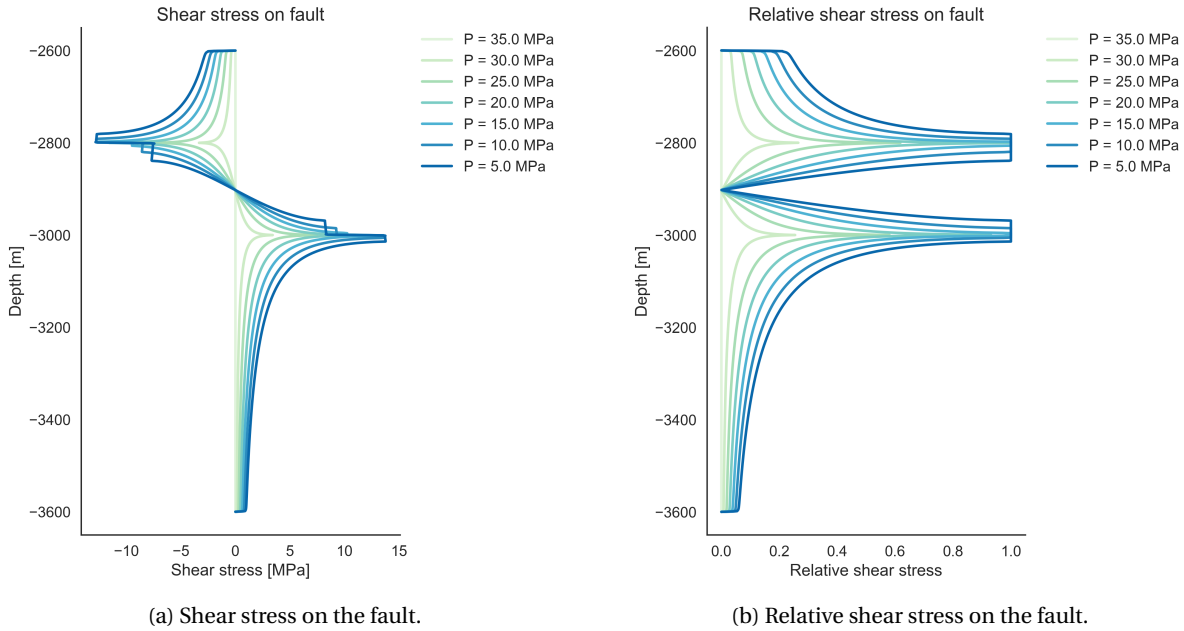


Figure 5.6: Shear stress and relative shear stress on the fault for different stages in depletion.

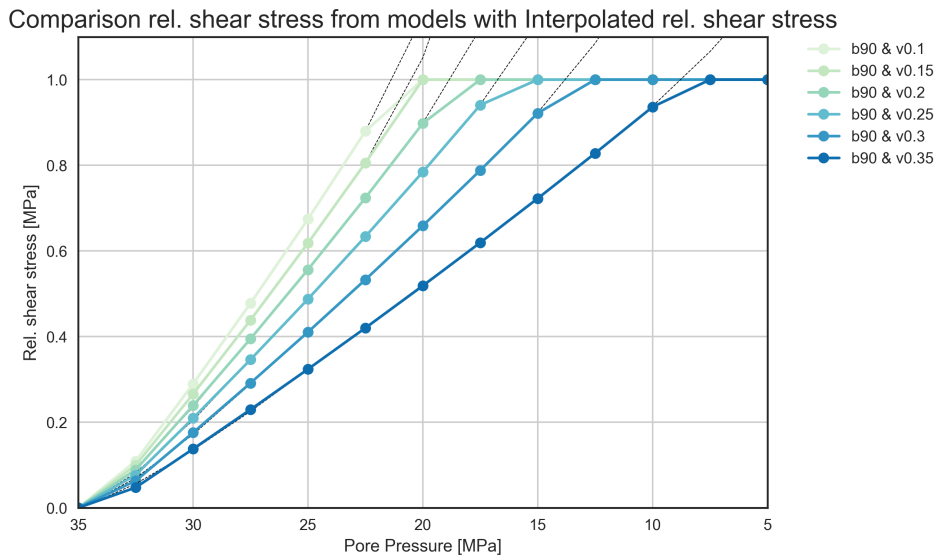


Figure 5.7: Comparison of the relative shear stress for each step of depletion from various simulation runs in which the Poisson's ratio was varied.

## 5.2. Simulations

After having taken a look at general behaviour of a depleting reservoir with a boundary fault and having established its behaviour during depletion, a sensitivity analysis of fault failure, as discussed in section 4, was performed by varying the geometry of the reservoir and fault as well as changing the rock and fault properties as shown in tables 4.2 and 4.3. The results are examined and interpreted next.

### 5.2.1. Effect of reservoir radius

When testing the geomechanical models for dependency on the reservoir radius it was found that for  $R = 500m$ ,  $R = 1000m$  and  $R = 3000m$  there is no effect on the failure behaviour of the fault. Figure 5.8 shows the relative shear stress over depth for the three models. There is no significant difference between the curves in the reservoir section (between  $-2800$  and  $-3000m$ ). In the region above and below the fault there are slight differences. As this is not of direct interest for this thesis it can be concluded that a reservoir with any radius larger than its thickness could be used for the analysis of initial fault failure behaviour. As an axisymmetrical model was needed to test the influence of the radius, no variations of the various rock parameters (as listed in table 4.3) were tested. With this test it was possible to establish that the radius of the reservoir has no influence on fault behaviour when  $R > h$ .

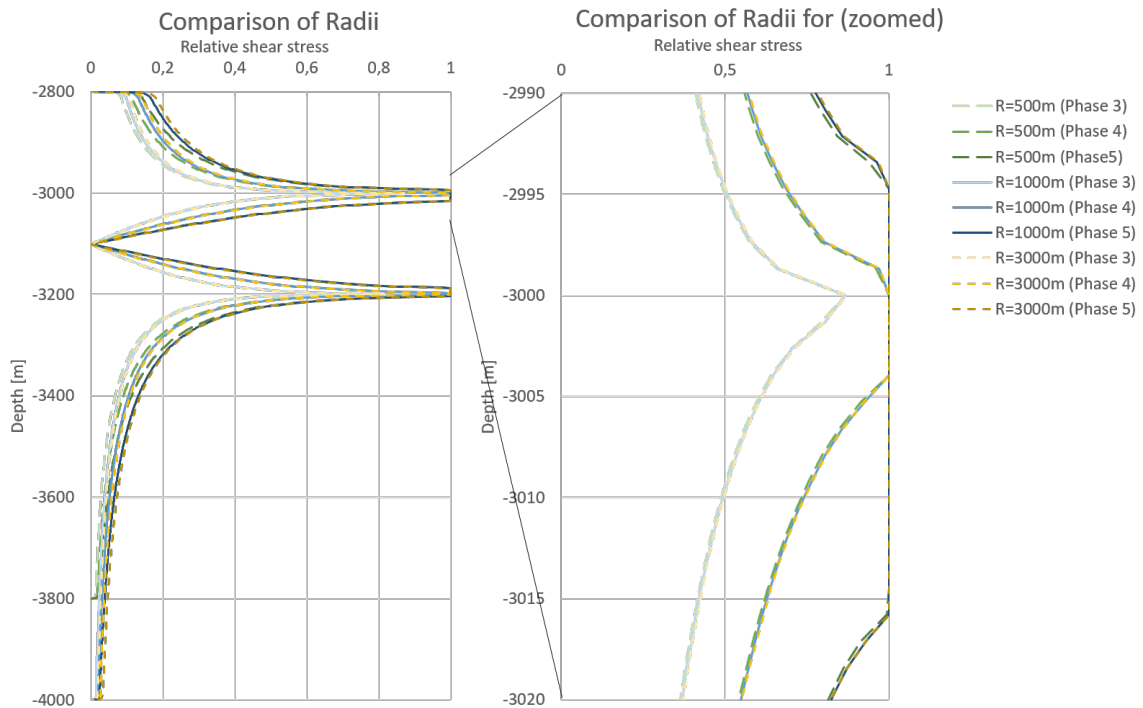
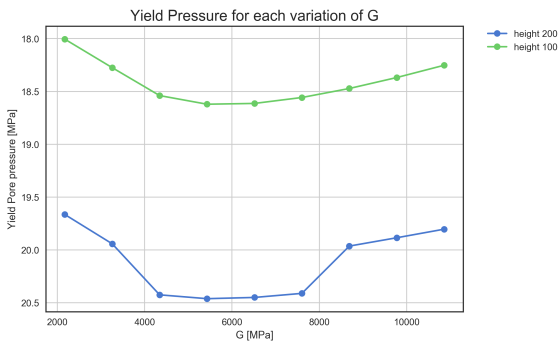


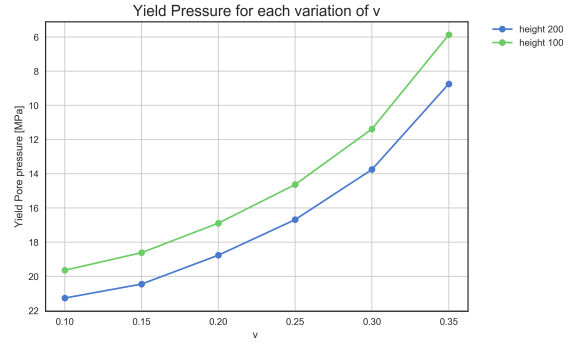
Figure 5.8: Comparison of three different Radii for three different stages of depletion over the entire length of the fault and a zoomed section of the reservoir top.

### 5.2.2. Effect of reservoir thickness

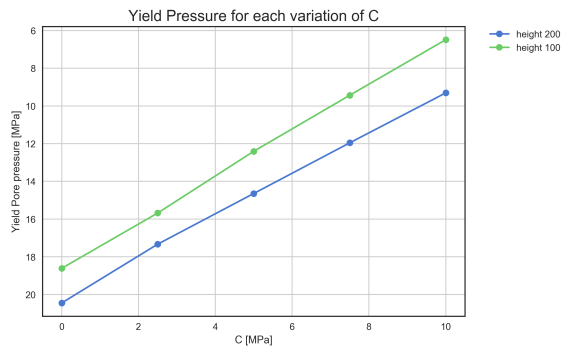
The second geometry variation investigated was the reservoir thickness. Figure 5.10 show that failure behaviour is non-linearly related to the reservoir thickness. Besides this, the differences between models of different reservoir thicknesses remains constant for variations of  $G$ ,  $\nu$ , and  $C$ . Only for variations of  $\varphi$  a change in behaviour is observed (figure 5.10d). Here, for smaller friction angles there is almost no difference between the different thicknesses, whereas for large friction angles the difference increases. It shows that with decreasing thickness the fault becomes more stable, reactivation thus occurring at larger levels of depletion (figure 5.9). This is logical as with thinner reservoirs less compaction occurs. This means that there are smaller differential displacements on both sides of the fault thus causing less shear stress. Thus failure occurs after further depletion of the reservoir.



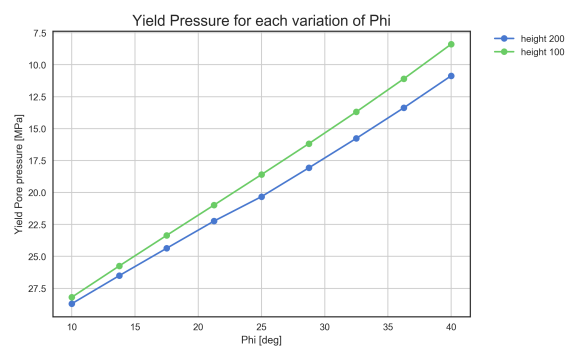
(a) Reservoir thickness versus shear modulus.



(b) Reservoir thickness versus Poisson's ratio.



(c) Reservoir thickness versus cohesion.



(d) Reservoir thickness versus friction angle.

Figure 5.10: Yield pore pressure of each variation of the reservoir thickness for all variations of geomechanical parameters.

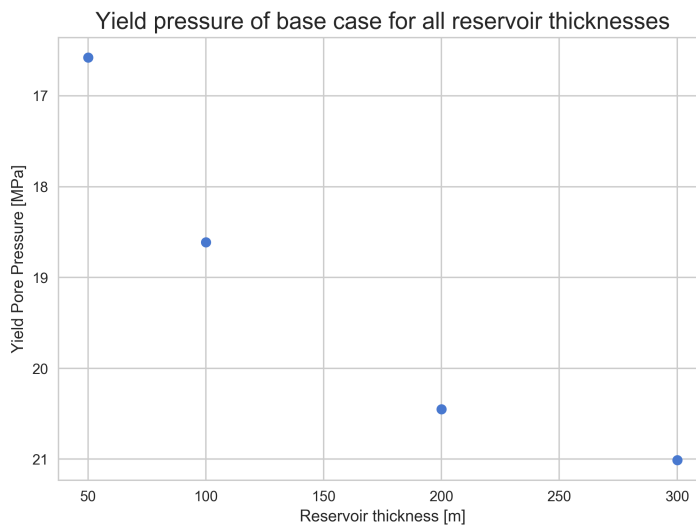


Figure 5.9: Comparison of the yield pressure for all base case models with varied reservoir thickness.

### 5.2.3. Effect of fault throw

For the base case parameter configuration of the model the fault throw seems to have almost no effect (figure 5.11). The same counts for variations of  $C$  and  $\varphi$ , the fault strength parameters (figure 5.12c and 5.12d). Here all the models overly each other and the yield pore pressure increases linearly. For the rock material properties,  $G$  and  $\nu$  (figure 5.12a and 5.12b), this behaviour is different. Variations of the shear modulus show that for negative throws (when the non-depleting side is lower than the depleting side) the change in yield

pressure is again very small and equal to when the fault has no throw. However, for faults with a positive throw the fault becomes much more stable for low values of the shear modulus and more unstable for higher shear moduli. Interesting to note is that the magnitude of the throw does not appear to play a large role. From this it can be deduced that simply the contact to a different material causes the differences and not the relative position of the reservoirs. Taking a look at the behaviour with changing Poisson's ratio, the exact opposite can be observed. Here positive throws have no effect and show the same as a fault with zero throw, and the negative throws show a stabilization with higher ratios and a destabilization with lower ones. The fault throw is a parameter which shows complicated behaviour and should be investigated into more depth.

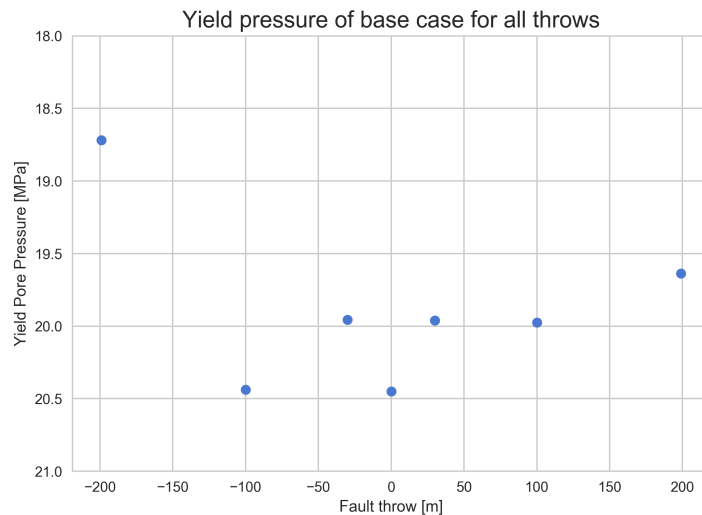


Figure 5.11: Comparison of the yield pressure for all base case models with varied throw.

#### 5.2.4. Effect of fault angle

For variations of the fault angle fault failure behaviour varies significantly for the various rock and fault parameters. For a fault with  $90^\circ$  angle there is little sensitivity to fault failure initiation for variations in the shear modulus. However, with a steep angle of  $79^\circ$  the lower shear moduli create a more stable setting, meaning failure will only occur with more depletion, when compared to the base case parameters, whereas the higher values initiate failure quicker. A more shallow angle of  $60^\circ$  shows the same behaviour as the steeper fault but there are many more values for  $G$  where the fault could handle a larger pressure drop before failure. For a fault of  $101^\circ$ , which would make the reservoir in the footwall instead of the hanging wall, the fault is much more stable than when the reservoir is the hanging wall.

Another interesting aspect is that the fault angle seems to control if failure first occurs just within the reservoir (at its top) or just above the top along the fault. For faults with a angle of  $60$ - $90^\circ$  the fault rupture is inside the reservoir and they fail at lower levels of depletion than faults with  $90$ - $120^\circ$ . For these initiation only occurs at a later stage, so after more depletion, and the failure point is located just above the reservoir top and the rupture then propagates upwards.<sup>1</sup>

For variations of the Poisson's ratio (figure 5.15b) the behaviour for the models with different fault angles are all similar. At lower values for the Poisson's ratio, the fault will fail more quickly than with higher values. Interesting to see is that a fault of  $79^\circ$  shows failure at the smallest amount of depletion.

Almost the same behaviour is seen for the cohesion (figure 5.15c). The figure shows that cohesion has a very strong effect on fault failure. Depending on the angle, failure will only occur in very late stages of depletion. Interesting to see here is the crossing of the line between fault angle  $90^\circ$  and  $79^\circ$  at a cohesion of around  $7.5 \text{ MPa}$ .

This behaviour is also found for variations of the friction angle. The friction angle also has a large effect on the failure pressure (figure 5.15d). Higher values of friction angle cause the fault to be stable and show no signs of failure for larger amounts of depletion. Low values cause the fault to fail with less depletion. The

<sup>1</sup>Note that these ranges are simply based on the modelled values and are not to be taken as absolute. Just as the direction or length of rupture cannot be taken exactly as such.

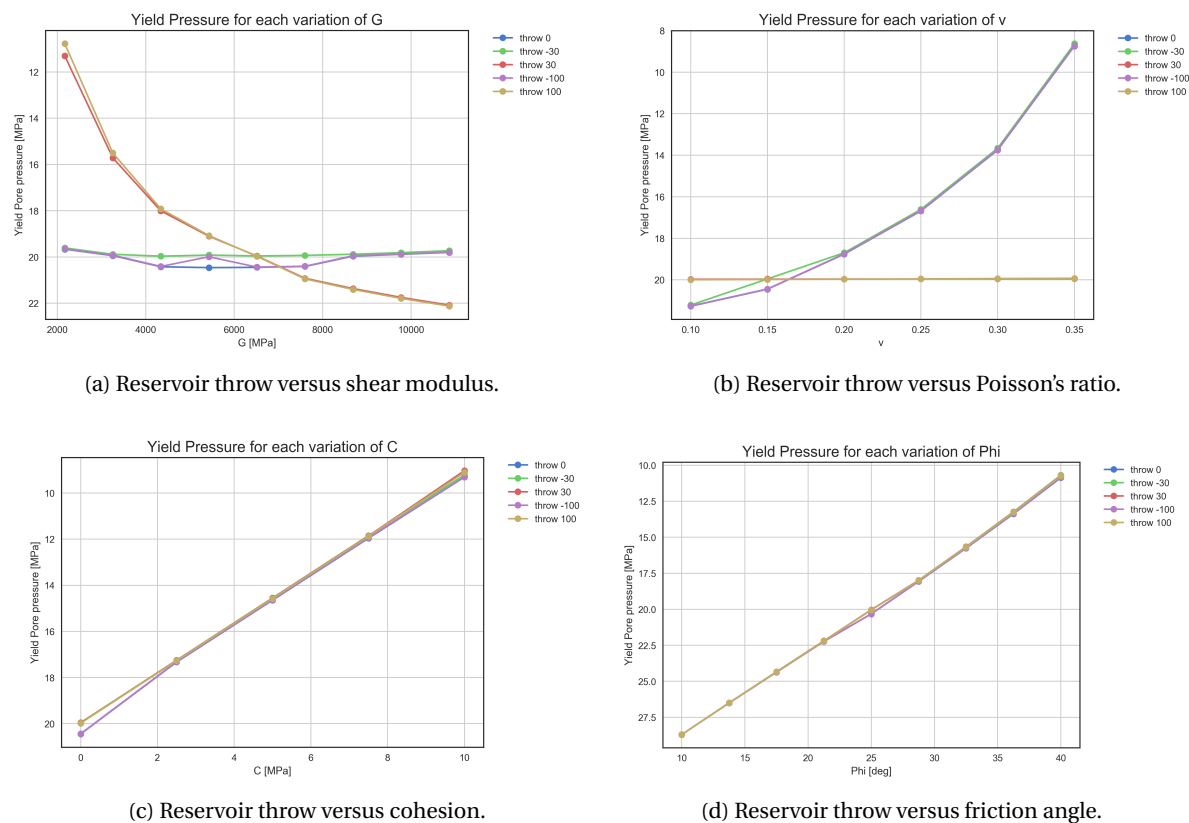
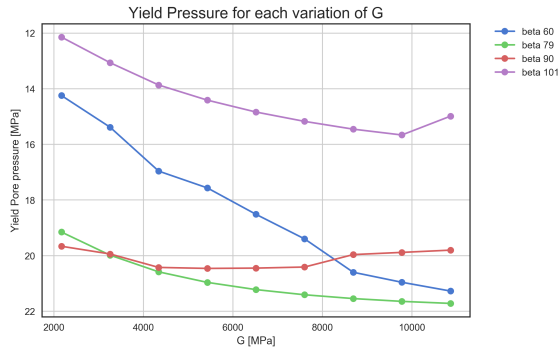


Figure 5.12: Yield pore pressure of each variation of the reservoir throw for all variations of geomechanical parameters.

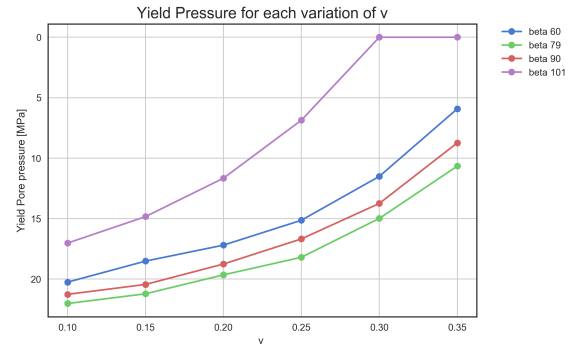
steeper the angle of the fault, the shallower the gradient over the variations of the friction angle are. This means that for steeper faults the friction angle has less influence on fault failure behaviour. This counts for faults between 60-90° dip. For the fault with an angle of 101°, it can be seen that the behaviour is different and stabilizes much quicker than with the other angles.

A different visualization of the sensitivities in figure 5.14 is to plot the data on 3-dimensional surfaces (figure 5.15). This allows for a better assessment and understanding of the behaviour of reactivation pressure for fault angles and rock / fault parameters which were not directly simulated in that specific combination. For example: If in a real case, the fault angle were 70° and the Poisson's ratio 0.35, you would be able to see that failure would occur between a reservoir pressure of 12.5 and 10 MPa.

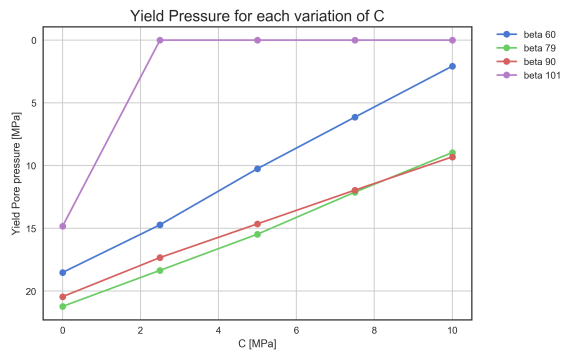
The yield pore pressure for the base case parameters for each of the fault angles clearly shows parabolic behaviour as seen in figure 5.13. Also a minimum can be seen at a fault angle of 80°. This means that under these conditions of the base case scenario, a fault which has that specific angle would fail first. This angle is also called the critical angle. It could be worthwhile to do more research on this as the mean angle of faults in the Groningen field happens to be close to this critical angle, 79°. The immediate question that arises here is: Could there be a link between the critical angle found on reservoir scale in this thesis and tectonic processes?



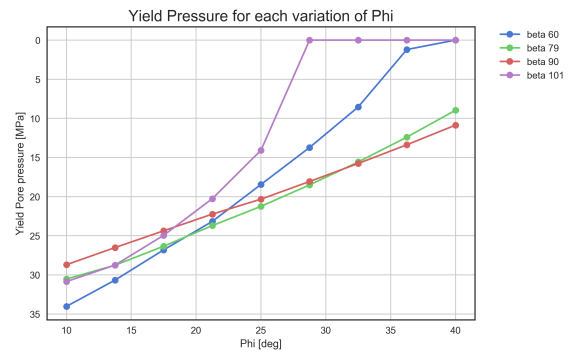
(a) Fault angle versus shear modulus.



(b) Fault angle versus Poisson's ratio.



(c) Fault angle versus cohesion.



(d) Fault angle versus friction angle.

Figure 5.14: Yield pore pressure of each variation of the fault angle for all variations of geomechanical parameters.

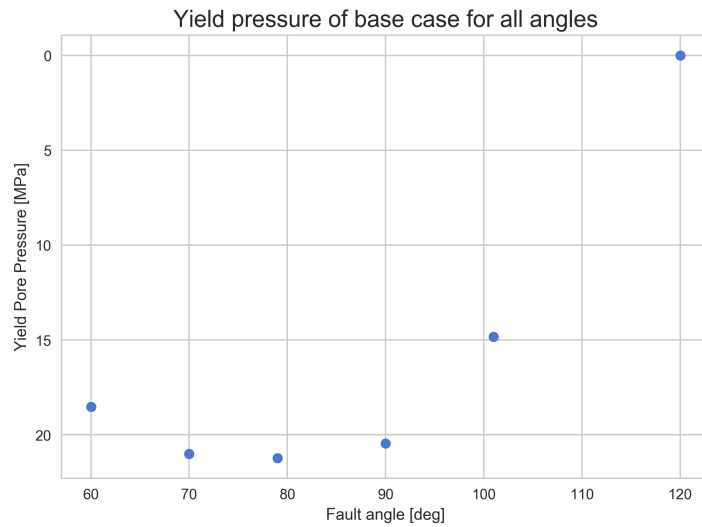
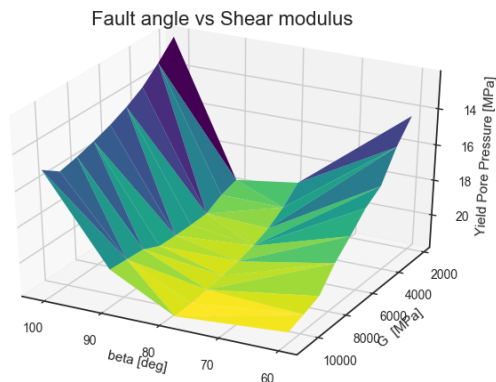
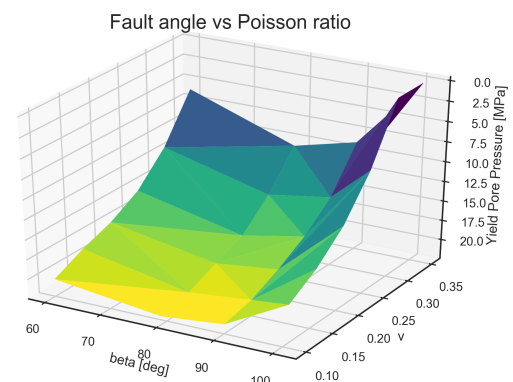


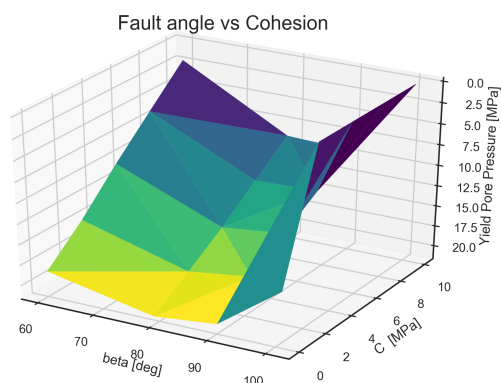
Figure 5.13: Comparison of the yield pressure for all base case models with varied fault dip.



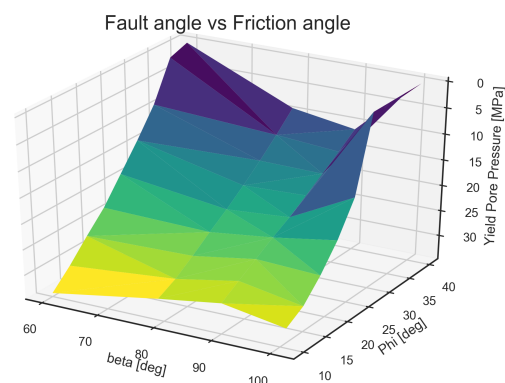
(a) Fault angle versus shear modulus.



(b) Fault angle versus Poisson's ratio.



(c) Fault angle versus cohesion.



(d) Fault angle versus friction angle.

Figure 5.15: Yield pore pressure of each variation of the fault angle for all variations of geomechanical parameters.

### 5.2.5. Fault failure sensitivity and the combining of information from various rock and fault properties

To compare all the created data in the simulations a histogram (figure 5.16) was made of all simulated models combined. They sum up to a total of 358 separate runs. It shows that for the range within the parameters were chosen there is a unimodal distribution of reactivation pressure. From all models run most will show failure at a reservoir pressure of around 18 MPa. The earliest reservoir pressure at which failure was observed was 34 MPa. This was for a model with a very low value for the friction angle. On the other hand, about 10 models did not fail at all. These models are the models with high values of cohesion, friction angle or Poisson's ratio.

Figure 5.17 shows the distribution for each varied parameter. Table 5.1 shows the amount of different simulations were run for each parameter.

Table 5.1: Amount of runs performed for each parameter

Parameter	Number of runs
$G$ [GPa]	126
$\nu$	84
$C$ [MPa]	70
$\varphi$ [deg]	125

Grouping the data according to the individual varied rock / fault parameters shows the relative sensitivities and spread of reactivation pressures for each parameter. Figure 5.18 visualizes the empirical density functions of the whole data, as presented in figure 5.16, as well as for each parameter separately. How large the spread is shows the relative influence variations of a parameter have on failure pressure. Looking at models in which the shear modulus was varied it becomes clear that in the chosen range for this parameter, there is almost no variation in failure pressure. All faults fail around 20 MPa, hence the large red peak. On the other hand, the yield pore pressure for variations of the friction angle show a large spread. This effect can be so significant that for certain values of the friction angle failure can occur at almost initial pressure. The probability (see figure 5.18) of this occurring lies within the same range as failure at a reservoir pressure of 5 MPa. As mentioned previously the friction angle has a very large influence on the initiation of failure on a fault. This indicates the importance of a correct estimation of the value of this factor when it is used in analysis in real field data.

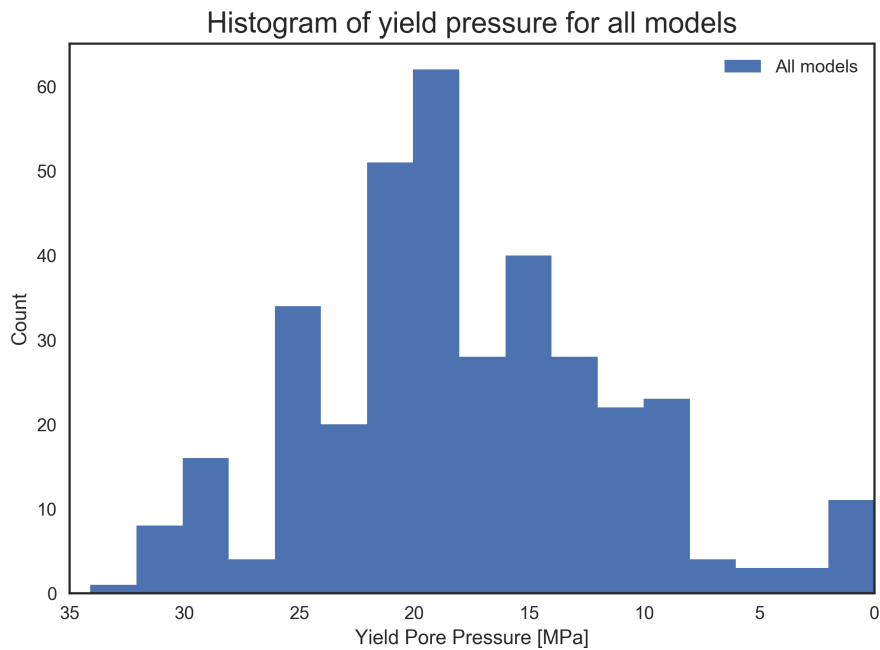


Figure 5.16: Histogram showing the spread for the values of yield pressure for all the models run.

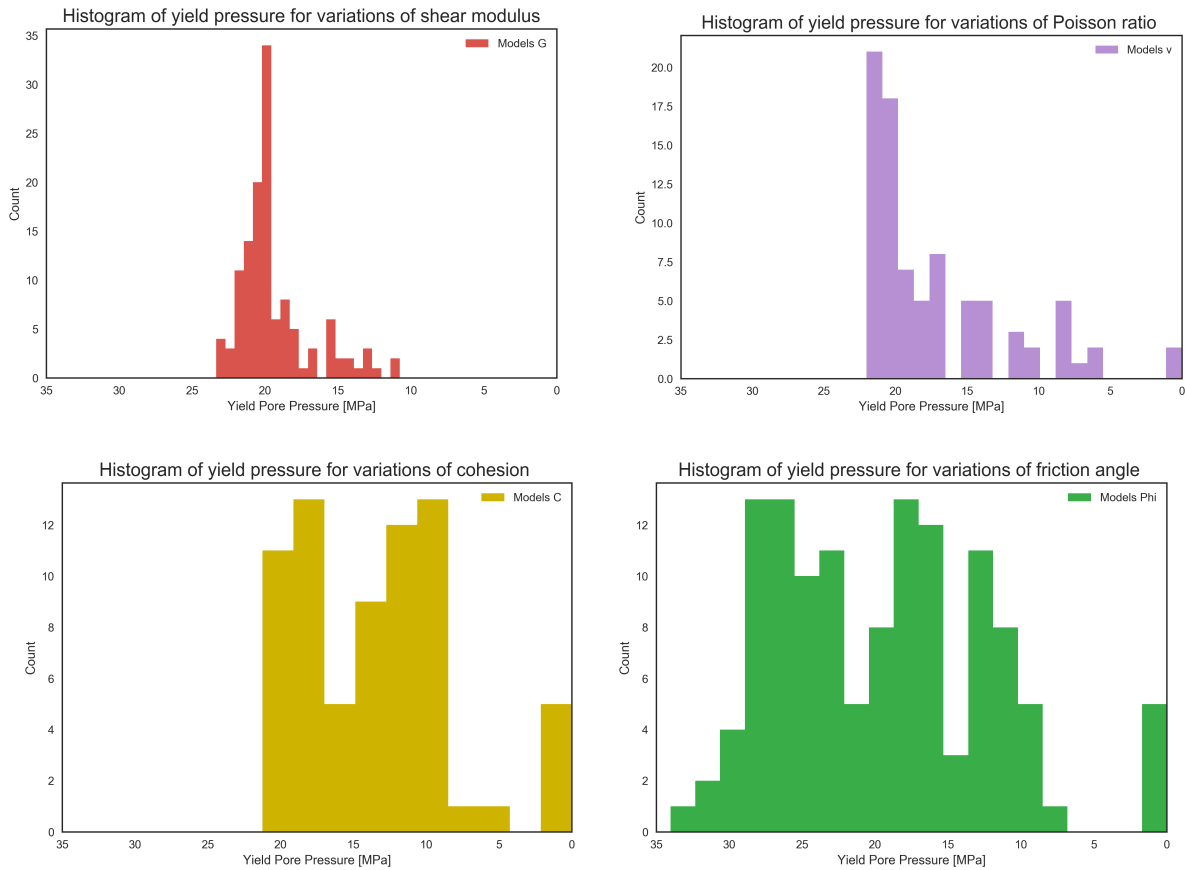


Figure 5.17: Histogram for all models run in which one parameter was varied.

Figure 5.18 does not, however, describe the interdependency of the parameters with each other. Until now the parameters were varied in isolation. However, it would be interesting to understand the behaviour for various combinations of both the rock and fault parameters and how they influence each other. By interpolation between the collected data points this becomes possible. Figure 5.19 shows these combined interpretations for the rock parameters shear modulus  $G$  with the Poisson's ratio  $\nu$  and the fault strength parameters Cohesion  $C$  with the friction angle  $\phi$  for a fault with an angle of  $90^\circ$ . From this we can infer that there is a non-linear relationship between these rock parameters and a linear relationship between the fault strength parameters. Practically, this means for instance if the Poisson's ratio would be higher than the base case, while the shear modulus remained the same, that the fault would show no failure for a larger amount of depletion. Similarly, this can be applied to the fault strength parameters.

It is important to remember that these results only apply to the range in which the parameters were chosen. They may however give a feeling for how each parameter generally influences the results, how sensitive fault failure is to variations of each parameter by itself or how the sensitivity translates to combined changes in parameters.

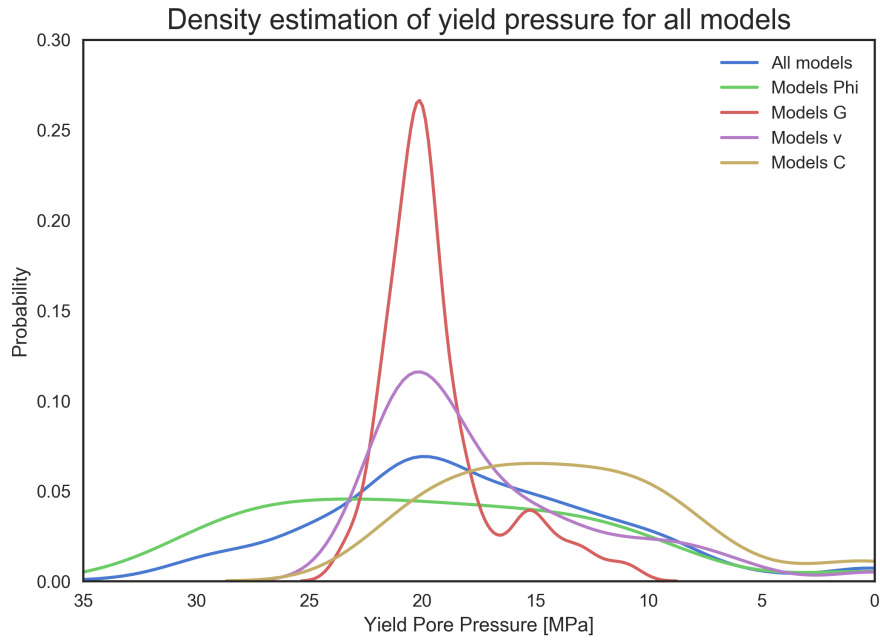


Figure 5.18: Density distribution showing the probability for each value of yield pressure for the various rock / fault parameters in the chosen range. This indicates which parameters have a large effect on failure

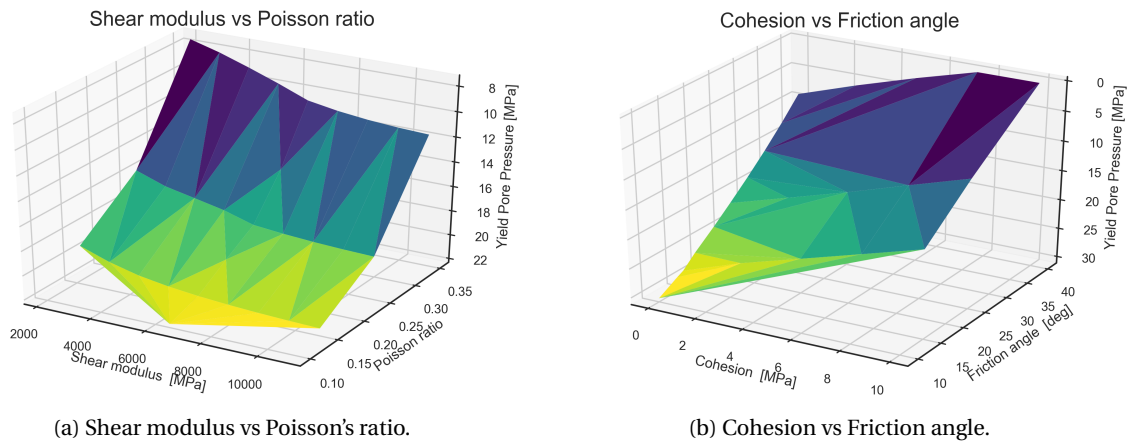


Figure 5.19: Combining information of rock and fault properties to see their interaction.

### 5.3. Comparing of analytical approach and simulations

After having looked at the results from the simulations and sensitivity study we will now compare them with the analytical approach in this section. To recall: the goal of the analytical approach is to determine  $\tau_f$  (see equation 5.4) since then it is possible to predict failure. The difficulty here is that some variables are still unknown. In the following sections it will be discussed how these unknown variables were obtained and what the new insights are by comparing the simulations and analytical approach.

#### 5.3.1. Determination of the influence zone

The last uncertain parameters left in equation 2.44 are the influence zones  $L_1$  and  $L_2$ , with  $L = L_1 + L_2$ . However, through FEM models it was possible to prove that equation 2.44 is only valid in the area so close around the fault that the displacement profile can be approximated linearly. This distance turns out to be up to  $0.1 * h$  away from the fault. However, when the vertical displacements are analyzed at a distance further away (e.g. where uniaxial strain conditions are valid), I found that  $L \neq L_1 + L_2$ . With this it becomes necessary to introduce a new variable. It will be named  $\Lambda_f$  and is a length value related to the thickness of the reservoir  $h$  with a certain constant  $c$ :

$$\Lambda_f = h * c \quad (5.2)$$

The only way to obtain  $\Lambda_f$ 's value is through modelling. Numerical simulations of a geomechanical model with a vertical boundary fault with the properties described in section 4 were run to assess the value of this influence zone. By analysing the vertical displacement profiles  $u_1$  and  $u_2$  at different distances,  $L_1$  and  $L_2$  (where  $L_1 = L_2$ ) from the modelled fault as well as the shear stress on the fault  $\tau_f$ , it is possible to determine the value of the influence zone  $\Lambda_f$  for each observation distance  $L$  and also for each depth within the reservoir. For a vertical fault  $\Lambda_f$  can be calculated using equation 5.3. It follows from equation 2.34 that  $\tau_{vh} = \tau_f$  in the case of a vertical fault. Figure 5.20b shows an example for  $L_1 = L_2 = 200m$  in which the calculated compaction induced shear stress  $\tau_{vh}$  has been fitted exactly to the curve of the shear stress  $\tau_f$  (red curve). The corresponding  $\Lambda_f$ , which varies with depth, can be seen in figure 5.20a for  $L_1 = L_2 = 200m$  and  $L_1 = L_2 = 500m$ .

$$\Lambda = G_f \frac{\Delta u}{\tau_{vh}} = G_f \frac{\Delta u}{\tau_f} \quad (5.3)$$

However, a varying value  $\Lambda_f$  is impractical for use in the analytical approach and since we are only interested in the point at the top of the reservoir, defining a constant value would be better. It was approximated in such a way that there was still reasonable overlap between  $\tau_{vh,appr}$  and  $\tau_f$  (see figure 5.20 b), green curve) and that the chosen value will still give correct calculations for  $\tau_f$  at the the weakest point, the top of the reservoir (at  $-2800m$ ), at which all analysis are done.

By analysing at different distances  $L$  the following relationship for  $c$  became apparent (figure 5.21). As mentioned above, the relationship can be described linearly up to a certain distance ( $0.1 * h$ ) from the fault, where  $\Lambda_f = \frac{L}{2} = L_1 = L_2$  is valid. However, when moving further away from the fault, the relationship between  $L$  and  $c$  becomes logarithmic. These findings can be formulated in such a way that they are related to the height  $h$  as  $\Lambda = c * h$  as seen in figure 5.21. The results are shown for two different reservoir thicknesses before fault failure. When putting both axis in relationship to  $h$  the lines fall together forming a globally applicable relationship approaching  $c = 0.5$  for observation distances far from the fault. Doing this for a situation in which failure has already occurred, shows that  $c$  approaches 1 and thus  $\Lambda = h$  as was postulated by Scholz (2002). So when analysing a fault before failure occurs a value of  $c$  between 0.25 and 0.4 seem to give the best matches between the analytical calculations and the simulations.

In general it was found that  $\Lambda_f$  is:

- Independent of the radius  $R$  of the reservoir
- Independent of the pressure difference  $\Delta p$  (before initiation occurs)
- Dependent on the depth  $z$  within the reservoir
- Dependent on the analysing distance  $L$  from the fault
- Dependent on the thickness  $h$  of the reservoir

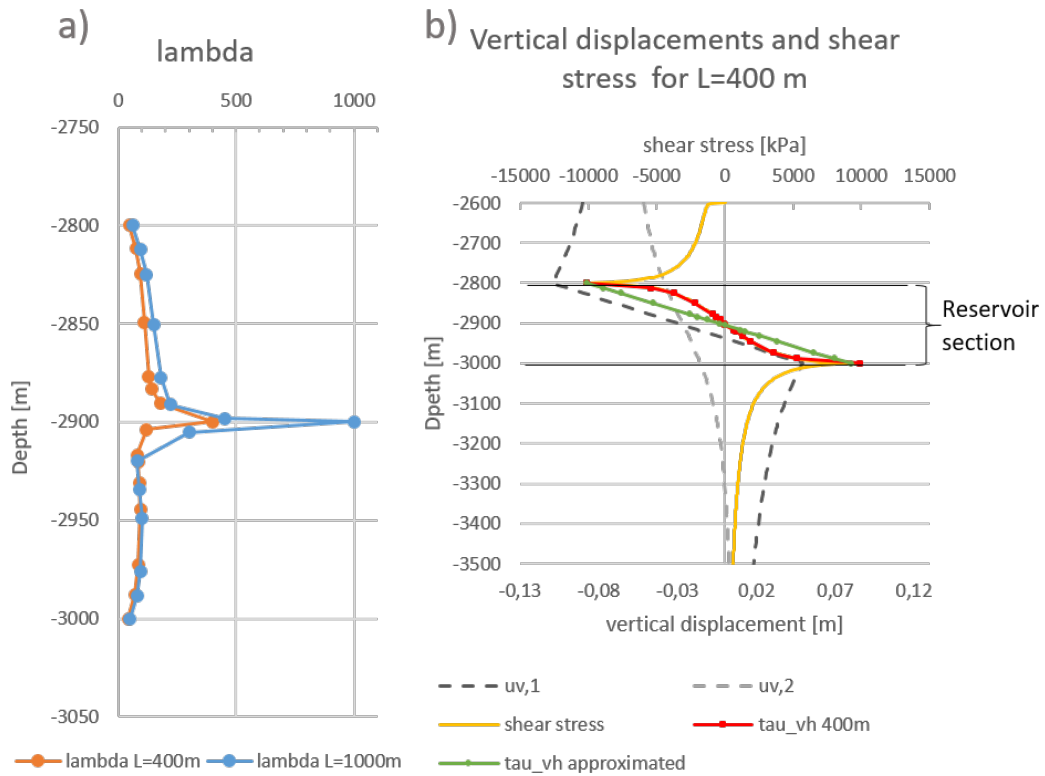


Figure 5.20: a) Change of  $\Lambda_f$  with depth within the reservoir section of a vertical fault. b) Exact and approximated fitting of the calculated compaction induced shear stress  $\tau_{vh}$  from the vertical displacements to the modelled shear stress  $\tau_f$

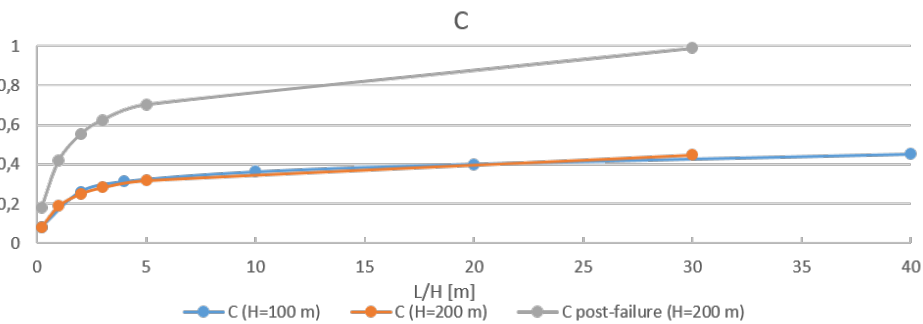


Figure 5.21: Relationship between  $\Lambda$  and the analyzing distance  $L$  by formulating the variable constant  $C$ .

### 5.3.2. Tuning of the analytical approach

So now more information on the behaviour and value of the last unknown within the analytical approach has been gathered, the approach is now ready to be used and the results compared to the simulations. Figure 5.22a shows a comparison of pore pressure as a function of shear stress computed analytically and numerically for a fault angle of  $90^\circ$ . Figure 5.22b does the same for  $\beta = 79^\circ$ . Each figure shows the analytically calculated values of the relative shear stress using the method of Poro-elastic Loading (PEL), with Differential Compaction Loading (DCL) as well as the simulation results corresponding to the equivalent input parameters. The most significant and important difference is the one between the calculations using PEL and those using DCL. Where the input parameters for the results in figure 5.22a resulted in zero relative shear stress when using PEL, the calculations using DCL and  $c = 1$  (as proposed by Scholz (2002)) differ from that result, moving toward a better match with the simulations. However, there is still a clear discrepancy between the simulations and the analytical results. When the value of  $c$  is adjusted to a value as described in section 5.3.1 it becomes possible to create quite good matches between the simulation results and the analytical approach.

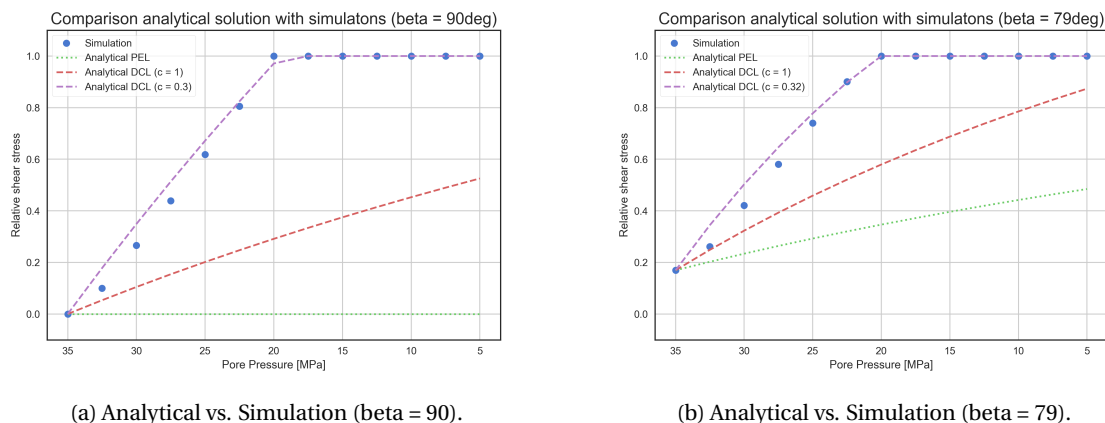


Figure 5.22: Comparison of the analytically calculated values for relative shear stress using the method of PEL and DCL with the simulation results.

The problem with not knowing what value  $c$  has is that I have to assume the simulations give correct results and thus in reality, the analytical approach is tuned so that it matches the simulations. We are thus rather speaking of a calibration / tuning instead of a benchmarking of the analytical approach.

In spite of the analysis in the previous section it is still difficult to decide which value of  $c$  is the most appropriate to be used. A large role in this is that while comparing the analytical results and simulations it became clear that which value to chose for  $c$  is strongly dependent on the input parameters for the analytical approach. Both the fault angle as well as which value is entered as the reservoir radius will cause  $c$  to change. Figure 5.23 shows this relationship.<sup>2</sup>

This stands in contrast to what the theory by Hettema (2018) says about the analytical approach. There the reservoir dimensions, including  $R$ , have a large influence on shear stress on the fault. A reason that these have an effect on the values of the calculation of shear stress  $\tau_f$  may come from the effect of  $R$  on the calculation of the vertical displacement  $u_z$ . As this is used as direct input for the induced shear stress  $\tau_{\nu h}$  the value of vertical displacement directly influences the value of shear stress. However, as the relationship of vertical displacement is not a linear one across the fault (see figure 5.2), this directly influences the results. The  $c$ -factor corrects this.

### 5.3.3. Reactivation pressure

When calculating the analytical reactivation pressure with equation 2.65 described in section 2, it was found that the analytically calculated pressures do not give similar results to the simulations. Even when an appropriate value for  $c$  is entered for the calculations. Figure 5.25 shows the reactivation pressure for  $c = 1$  and  $c = 0.42$ . For both there is no match as the reactivation pressures are negative.

There seem to be two axis of mirrored symmetry within the graph. One could be resolved by changing the sign of the analytically calculated reactivation pressure, which would make all the pressures positive. And flipping the graph by taking the fault angle as  $\beta_{f,new} = 180^\circ - \beta_f$  achieves a relatively good fit. This leads to believe that there is possibly a sign error within the equation and that the definition of the fault angle plays a crucial role in the calculation process of reactivation pressure.

Besides the slight differences, which might be explained by assumptions of uniaxial conditions within the analytical approach, a clear difference in behaviour can be seen. The simulation shows a critical angle  $\beta_{crit}$  at a fault angle of around  $80^\circ$ , whereas the analytical approach shows that faults with  $90^\circ$  are the weakest and will fail at the smallest level of depletion.

It is interesting to take a look at which of the two results is more in line with actual observations as this information is of critical importance when the methods want to be applied to real life situations. As mentioned previously it would also be interesting to take a look at the value of the critical angle from the simulations as it is exactly around the same values as the mean value for fault angles of the Groningen field data-set.

<sup>2</sup>This radius in the figure has nothing to do with the actual reservoir radius, it is simply the value entered into the analytical approach as radius. As discussed in section 5.3.1 the influence zone ( $\Lambda = c * h$ ) is independent of  $R$ .

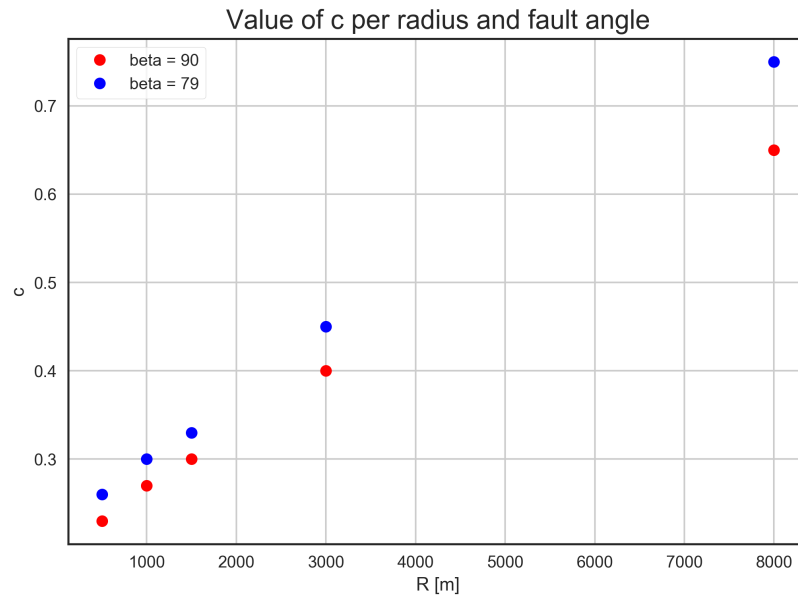


Figure 5.23: The dependency of the factor  $c$  on the fault angle and on which value is entered for the radius  $R$  in the analytical approach. Note: do not confuse this with the actual value of the reservoir radius.

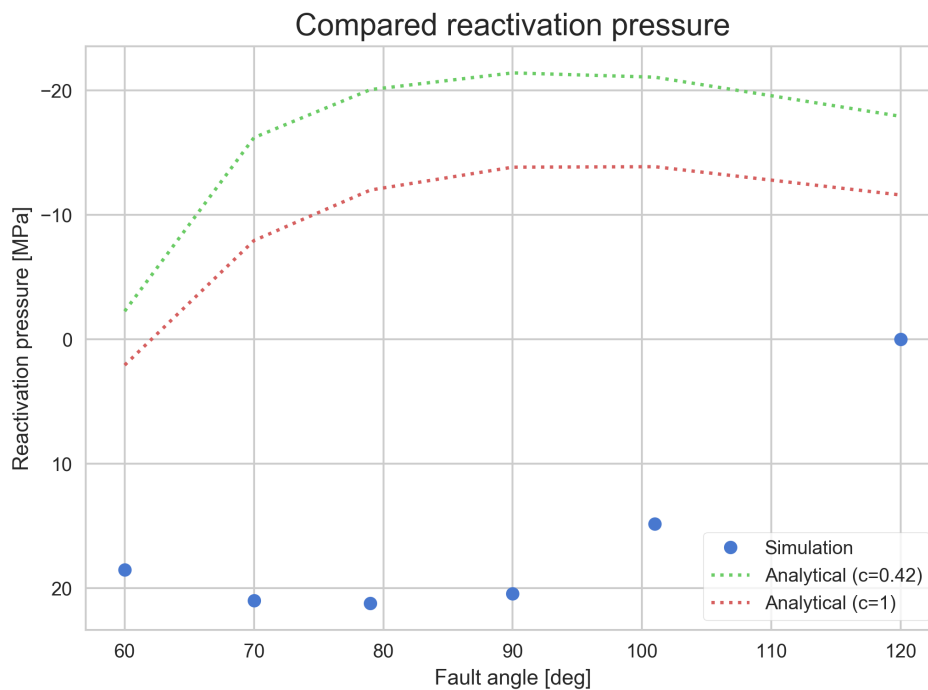


Figure 5.24: Comparison of the analytical and simulated reactivation pressures for different fault angles.

### 5.3.4. Critical fault angle for reactivation

The first step in finding a relationship for the critical fault angle, i.e. the angle at which failure occurs first under certain circumstances within the reservoir, was to check the simulation results for the sensitivity of the critical angle  $\beta_{crit}$ . From figures 5.15a to 5.15c we can see that the critical angle for reactivation stays mostly constant. For variations in Poisson's ratio and cohesion this is certainly the case, for variations of the shear modulus there are slight variations and for the friction angle there are strong changes (see figure 5.15d).

To explain these changes it becomes necessary consider the mathematical principles behind these phe-

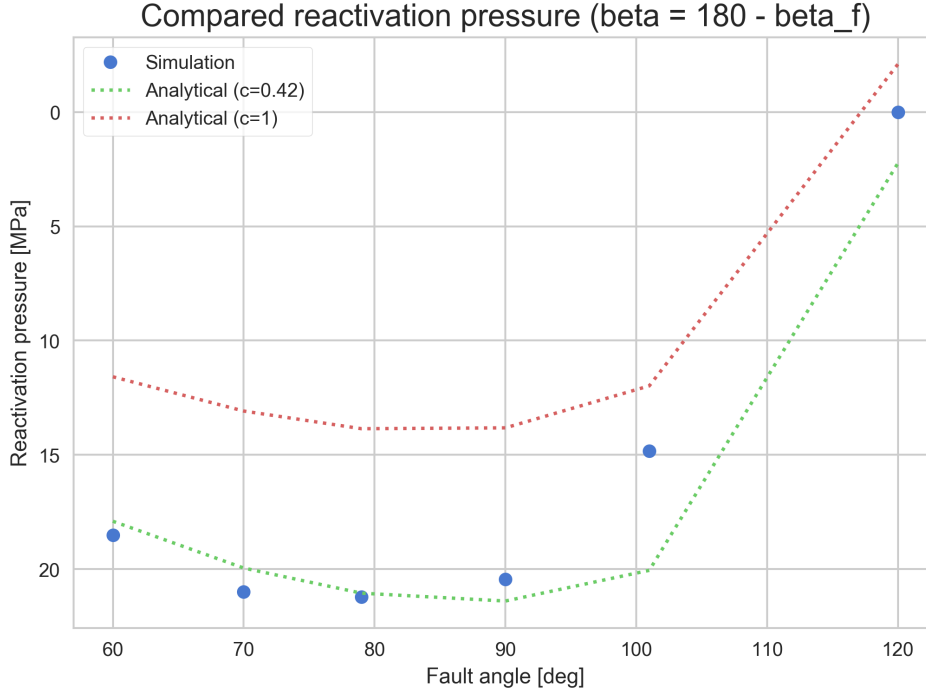


Figure 5.25: Comparison of the analytical and simulated reactivation pressures with  $\beta_{f,new} = 180^\circ - \beta_f$  for different fault angles.

nomena.

From the equation for the absolute shear stress on the fault (equation 5.4) a linear relationship between  $\tau_{max}$  and  $\tau_{vh}$  can be derived which allows us to formulate  $\tau_{vh}$  as  $-X * \tau_{max}$  in which  $X$  is an unknown scaling factor.

$$|\tau_f| = \frac{\sigma_v - \sigma_h}{2} \sin 2\beta - \tau_{vh} \cos 2\beta \quad (5.4)$$

$$= \tau_{max} \sin 2\beta - \tau_{vh} \cos 2\beta \quad (5.5)$$

$$= \tau_{max} \sin 2\beta + X \tau_{max} \cos 2\beta \quad (5.6)$$

The next question is the value of  $X$ . The shear stress on the fault can be calculated with the sum of the term with "sin", in which  $\tau_{max}$  forms the amplitude of the function, and the term with "cos", in which  $\tau_{vh}$  forms the amplitude. The rotation angle  $\beta_{rot}$  forms the phase shift between the curve calculated using the classical PEL method (so just with the "sin" term) and the curve with the new method DCL.  $\beta_{rot}$  is the angle between the initial direction of the maximum principal stress (in this case vertical) and the direction it has after depletion. To determine this shift the angle at which the curve of  $\tau_f$ , when calculated with DCL, reaches its minimum needs to be known. This angle will be called  $\Theta$ .

Before finding  $\Theta$ , we will first find  $X$  by setting the first derivative of  $\tau_f$  to zero and solving for  $X$ :

$$\frac{\partial |\tau_f|}{\partial \Theta} = 2\tau_{max} \cos 2\Theta - 2X\tau_{max} \sin 2\Theta = 0 \quad (5.7)$$

$$X = \frac{\cos 2\Theta}{\sin 2\Theta} = \cot 2\Theta \quad (5.8)$$

To find the value for  $X$  the shear stress on the fault  $\tau_f$ , the vertical stress  $\sigma_v$  and corresponding horizontal stress  $\sigma_h$  were taken from the simulations for each depletion step and substitution into the following equation derived from equation 5.4.

$$X = \frac{\frac{|\tau_f|}{\tau_{max}} - \sin 2\beta}{\cos 2\beta} \quad (5.9)$$

Knowing  $X$  allows the direct calculation of  $\tau_{vh}$  by multiplication with  $\tau_{max}$ .

With this the angle  $\Theta$  can be derived and the phase shift determined with  $\Theta - \frac{\pi}{4}$  as in figure 5.28a which shows the result for a fault with  $\varphi = 25$  deg.  $\frac{\pi}{4}$  is the angle at which the curve for shear stress when just using PEL is at its minimum. Or as discussed in section 2, the rotation angle  $\beta_{rot}$  can be calculated as follows:

$$\beta_{rot} = \frac{1}{2} \arctan\left(\frac{2\tau_{vh}}{\sigma_v - \sigma_h}\right) \quad (5.10)$$

Just as  $\tau_{max}$  changes with each step of depletion, so does  $\Theta$ . Doing this for all depletion steps, figure 5.26 shows that the rotation angle increases with depletion. However, the increase is non-linear and at larger depletion, the angle changes at a much smaller rate.

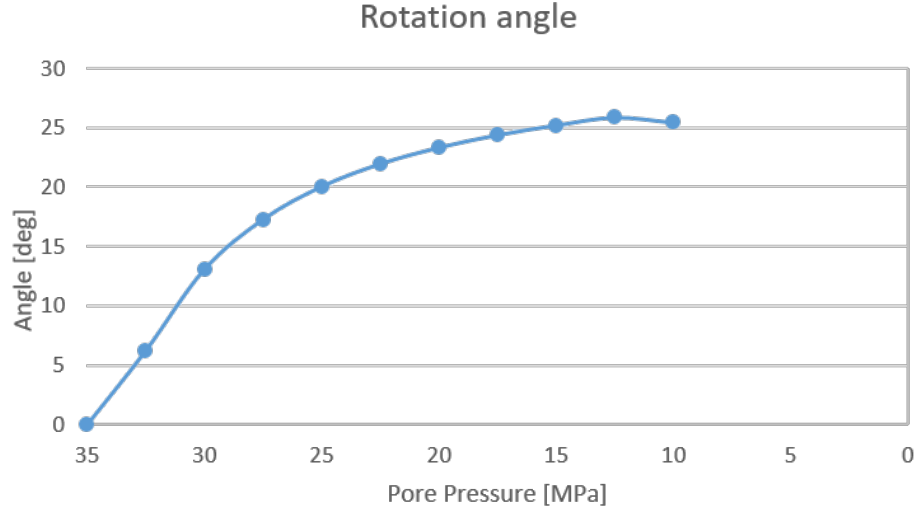


Figure 5.26: Rotation angle varying with depletion.

Now that beta rotate has been found it becomes possible to determine the critical angle  $\beta_{crit}$ . To do so, it is necessary to know the value for  $\tau_{vh}$  immediately before failure. This is also where it becomes important to look at the friction angle  $\varphi$  of the fault.

From the simulations performed for a fault with a specific friction angle the depletion at which failure initiates can be found along with the shear stress on the fault  $\tau_f$  (in theory the same as  $\tau_{fail}$ ) as well as the corresponding  $\sigma_v$  and  $\sigma_h$  at that moment. Entering them into equation 5.9,  $X$  can be found which will give the value for  $\tau_{vh}$ . The critical angle is that angle at which there is the smallest difference between the shear stress  $\tau_f$  and the failure shear stress  $\tau_{fail}$ . Graphically seen, as in figure 5.28b which shows the results for a fault with a friction angle of 25° this is around 80°. This result agrees with the simulation results described in section 5.2.  $\tau_{fail}$  is described by equation 5.11 and  $\sigma'_f$  comes from equation 2.33.

$$\tau_{fail} = C + \sigma'_f \tan \varphi \quad (5.11)$$

Figure 5.27 shows how the critical angle is related to the friction angle of the fault.

From these graphical figures it was derived that the critical angle for when DCL is included can be described as:

$$\beta_{crit} = \beta_{crit,PEL} + \beta_{rot} = \frac{\pi}{4} + \frac{\varphi}{2} + \beta_{rot} \quad (5.12)$$

## 5.4. Uncertainty

One of the larger uncertainties in analysing the results is during the extraction of the reactivation pressure from the simulations. As this is done by extrapolation (see figure 5.7) it is likely that this is not exact. However, because Plaxis creates the same output results for multiple runs of the same model, it was difficult to estimate the global error on the results created by all the different assumptions, simplifications and uncertainties. Therefore it was chosen that as all the uncertainties apply to each point no errorbars were plotted on the figures. However, it should be remembered that an uncertainty is connected to the results.

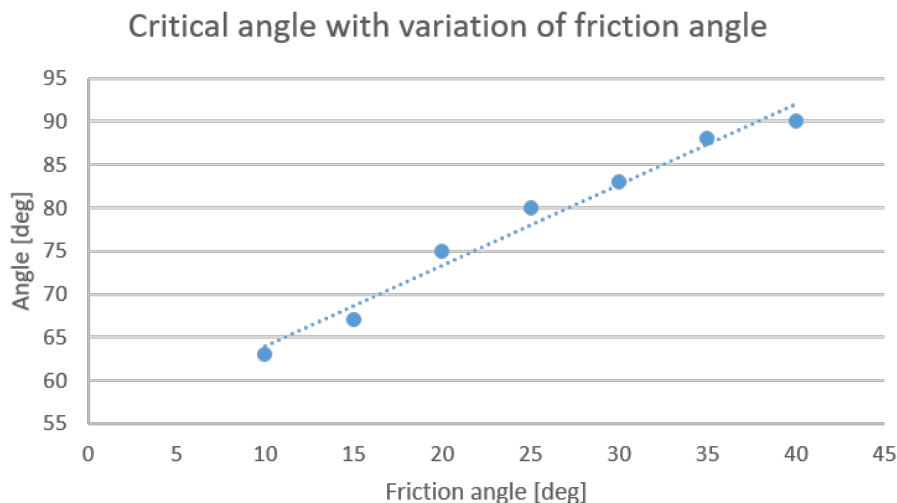
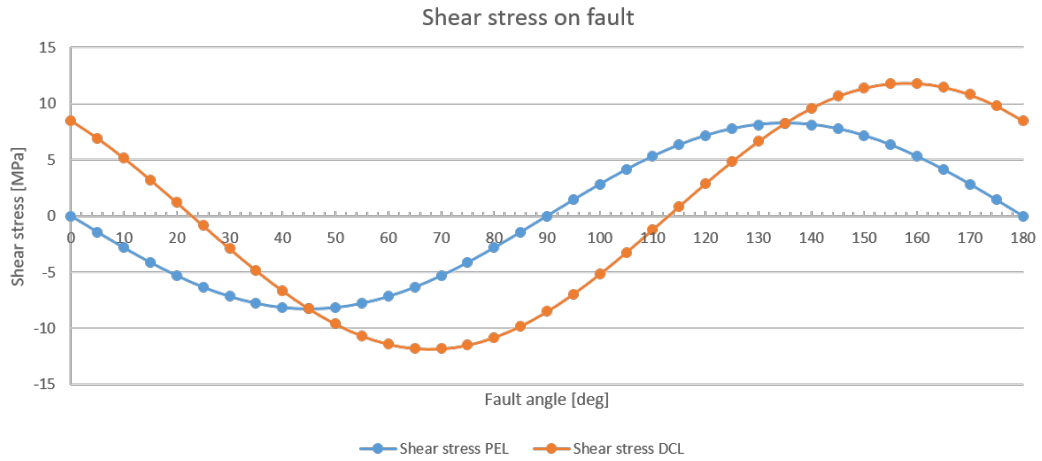


Figure 5.27: Analytically calculated critical angle for faults with various friction angles.

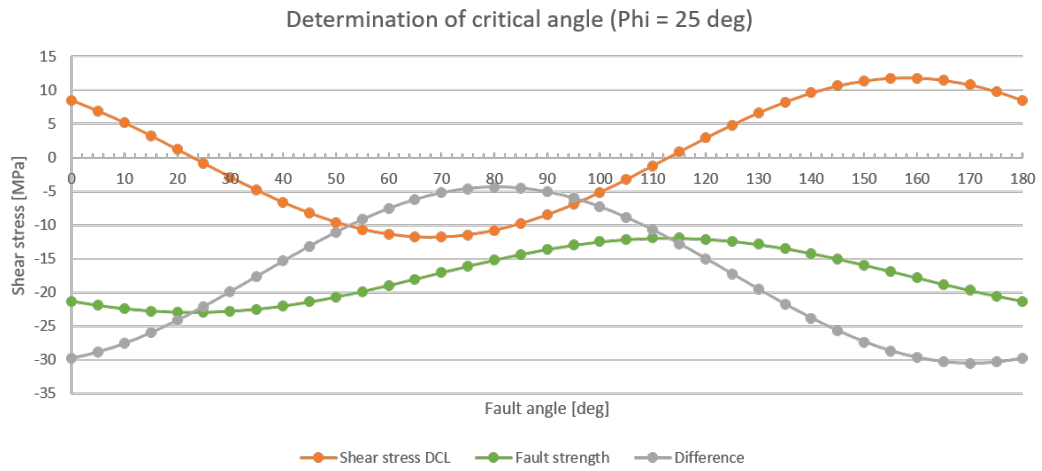
When comparing the simulation results with the analytical solution it becomes clear there is still quite some discrepancies and difficulties to overcome. Especially troublesome is the factor  $c$  which is heavily dependant on the input parameters used for the analytical approach. However, if correctly estimated, it is possible to generate a relatively good overlap between the simulations and analytical approach for the calculations of the relative shear stress at a certain level of depletion.

When analytically calculating the reactivation pressure the results did not coincide at all. Possible reasons for this might be that the equation for the reactivation pressure (equation 2.65) contains only the fault angle along with some material properties ( $\varphi$  and  $\nu$ ) and geometry of the reservoir (radius  $R$  and reservoir thickness  $h$ ). Therefore, it could be considered that the proposed relationship does not take all different effects into account to correctly estimate the reactivation pressure analytically.

Possibly a different approach could lead to better estimates. For example: apply the same approach of extrapolation as with the simulations, like was done in figure 5.7. Instead of extracting the reactivation pressure from results created in the simulations, the analytically calculated relative shear stress could be used, resulting in the reactivation pressure where the relative shear stress becomes 1. Here again the difficulty of estimating an appropriate value for the factor  $c$  plays a large role to gain correct results.



(a) Shear stress on fault just before failure.



(b) Determination of the critical angle for a fault with friction angle of 25 degree.

Figure 5.28: Figure 5.28a Shear stress on a fault with a friction angle of 25 deg just before failure and the corresponding rotation angle. Figure 5.28b Determination of the critical angle for a fault with friction angle of 25 degree.

# 6

## Conclusions & Recommendations

In this thesis a combination of analytical and numerical methods were used and compared. Apparently, this is an unusual approach as it is not often seen in the literature on previous research (see chapter 1). Most of these publications focus on either only performing simulations or only analysing fault failure analytically. Therefore, the approach taken in this thesis, to perform simulations and to compare these with a new analytical approach have led to new insights on the understanding of fault failure behaviour. The main benefit of this combination is that both the credibility of the simulations and the analytical approach are strengthened, as they can be compared. The numerical analysis done allows a feeling for fault failure sensitivity to be established. The comparison with the analytical approach allows for the extraction of mathematical explanations for phenomena and behaviour seen in these simulations.

The main use of the simulations proved to be the establishment of an empirical sense of sensitivity for the behaviour of the reactivation pressure to variations in both reservoir geometry and material properties. Especially, when trying to assess the sensitivity of a fault, or multiple faults, within a field simulations can provide a range in which the reactivation pressure might be expected. Besides this the simulations can show how behaviour of the fault might change if a parameter were different than estimated.

With the analytical solution it becomes easier to quickly assess fault stability within a reservoir by applying a set of equations. For field applications this quick and fast approach can lead to the reduction of uncertainty on fault stability and better mitigation of risk in exploration or production phases of reservoirs.

The ultimate goal in this field of studies would be the prediction of fault reactivation and the mitigation of seismicity in reservoirs that are being used for production or injection purposes. This research brings us yet one step closer to a better understanding of these phenomena. Further investigation into what the combined analysis of simulations with the new analytical approach by Hettema (2017) might reveal could definitely result in to more insights still.

Below, a more detailed listing of all the conclusions is presented . This has been divided into three parts. Conclusions linked to either the simulations, those linked to the analytical approach and general findings. Following them are recommendations for further research on the subject of this thesis and related topics.

### 6.1. Simulations

Generally, it can be said that the simulations in this thesis have allowed for a broadening of the application range compared to what the analytical approach allows. With this, a better understanding has been obtained of non-homogeneous conditions, the influence of geometrical factors of the reservoir and fault as well as various combinations of rock and fault parameter values. It was found that both the geometrical aspects as well as the rock and fault parameters play a substantial role in fault failure sensitivity. By analysing the distribution in reservoir pressure at which failure initiation occurs it was found that:

- Varying the fault angle  $\beta_f$  between realistic limits creates the largest spread in reactivation pressure of the varied geometrical parameters.
- The friction angle  $\varphi$  of the rock / fault is the most sensitive property with respect to the large spread it causes in the reactivation pressure when varied.

- Varying the shear modulus  $G$  (in the range it was chosen within this thesis) has almost no effect on the reactivation pressure.
- A combined analysis of the interdependency of the various material properties shows how these properties can interact. This directly accentuates the importance of correct estimation of material properties when performing simulations or calculations with the analytical approach.

Other findings which results from the analysis and interpretation of the sensitivity study performed in this thesis are:

- The reservoir radius has no influence on fault failure initiation for a reservoir with  $R \gg h$
- Thicker reservoirs are more likely to show failure along the fault than thinner reservoirs.
- If faults have a throw, the material properties of the point of contact of the top of the depleting section of reservoir defines if failure occurs after a certain amount of depletion. Here, high values for Poisson's ratio  $\nu$  and low values for the shear modulus  $G$  cause the fault to remain stable, so without failure, for a larger amount of depletion.
- Especially steep normal faults (opposed to a regular normal fault of  $60^\circ$ ) in which the reservoir is in the hanging wall are more prone to failure.
- The steeper the fault dip for a reservoir in the hanging wall, the less influence the cohesion  $C$ , friction angle  $\varphi$  and the shear modulus  $G$  have on failure pressure.

When comparing these results to previous research such as van den Bogert (2015), a significant difference is that the general behaviour of each parameter is more clearly defined in this thesis so that an empirical sense of sensitivity is established for each parameter. Also the investigation of how the reactivation pressure behaves when parameters are changed in combination and not just isolated is aspect not looked into before.

Even though case studies such as from Roest and Kuilman (1994) are possibly of more interest and of more direct applicability to real fields in the subsurface, it is often difficult to find the underlying reasons for a certain response. By linking simple simulations as were performed in this research to theory, deeper lying explanations may be found for the simulated phenomena. This will increase the overall level of and thus the understanding and insights into the mechanisms related to fault reactivation.

## 6.2. Analytical approach

When comparing the results from the simulations with the analytical approach multiple insights were gained:

- Successful calibration / tuning of the analytical approach was achieved. This included the finding of an appropriate value for the factor  $c$  which forms the last unknown in the analytical equations. This factor, however, is strongly dependent on which fault angle and value for the radius are entered into the equations used in the analytical approach. This requires further study.
- The rotation angle of principal stresses was found analytically by means of a newly developed method and matches with the results from the simulations.
- It was possible to find a new definition for the critical fault angle for when the new theory of DCL is implemented. The critical angle can be linked to a specific depletion pressure and rotation angle of the principal stresses. Hence, the analytically calculated results match the results from the simulations.
- Analytical calculation of the reactivation pressure did not result in a match with simulations. Possibly a wrong sign and/or different definition for the fault dip angle could be causing this discrepancy.
- Furthermore multiple limitations of the analytical solution were defined:
  - it can only be applied to homogeneous rock conditions,
  - it uses the assumption of uniaxial strain conditions throughout the entire model and
  - the robustness and precision of estimation factor  $c$  is defining for the precision of the analytical calculations.

In no previous study have simulations been compared to analytical calculations of stress on a fault with an analytical approach which incorporates the effect of differential compaction.

The simulations have helped define an entirely new definition for the critical fault angle for situations in which differential compaction is present (see equation 5.12). The value of the critical fault angle is of great importance when estimating the general stability of faults within a reservoir.

Furthermore, this thesis has not only shown that in a situation where differential compaction is present a rotation of the principal stresses occurs but this rotation has also been quantified using a new mathematical approach. The method to finding this rotation could be a first step in the better understanding of stress rotation around heterogeneities in the subsurface.

### 6.3. General findings

The general conclusions are not specifically related to either the simulations of the sensitivity study nor the comparison with the analytical approach are these:

- In section 5 it was discussed that when analysing the vertical displacement throughout the reservoir across a boundary fault Hettema (2017) found that  $f_3 \neq 1$ . This stands in contrast to what was once proposed by Geertsma and Van Opstal (1973). The simulations are in line with Hettema (2017) findings.
- Hettema's theoretical approach to implement DCL leads to results closer to the actual observations from real fields showing fault reactivation as discussed in section 5.3.2. It is also possible to calculate failure at any depth within the reservoir, not solely for the central reservoir depth.
- The mechanism of fault failure initiation is strongly dependent on the location along the fault within the reservoir. The weakest part of a fault is at the reservoir top in the depleting side with the first signs of failure always located there. The top is followed by the bottom border of the reservoir.
- From multiple simulation runs that were performed to test the influence of the Virtual interface thickness VIT, it was deduced that a smaller VIT results in fault failure initiation with less depletion. It was concluded that if the VIT was reduced to 1 m by reducing the general model size, the prediction of fault failure was quite accurate. The target element dimensions of the model should thus have a maximum of 100m.

### 6.4. Recommendations

With this research a start was made in understanding fault failure initiation in differentially compacting reservoirs. However, even though some questions were answered and promising new leads have been found, many new questions have arisen throughout the process. These have led to the formulation of the following recommendations:

- Perform further investigation into the analytical calculation of reactivation pressures.
- Investigate how simulations and analytical approach can be in better agreement. As a first step I recommend further investigating the following aspects:
  - Is the assumption of uniaxial strain sustainable?
  - Given the limited influence of certain parameters (e.g. reservoir radius): Is it possible to eliminate variables from the equation that have no influence on the initiation of fault failure at all?
  - What is the effect when the vertical displacement of the non-depleting side is also taken into account for the calculation of shear stress on the fault? Is it possible to bring the analytical approach in closer agreement to simulations in such a way?
  - Would it be possible to find a different approach for the analytical calculation of the reactivation pressure? A possible approach is briefly discussed in section 5.4
  - Perform further research on the dependence and value of factor  $c$ .
- Investigate if the newly found relationships on reservoir scale can be used for phenomena on larger (e.g. tectonic) scale.

- Investigate the effect of the effective stress ratio  $K_0$ . At the moment opinions on which value the effective stress ratio has are very divided. Looking into how fault failure would be influenced by this value could bring new insights.
- Develop Plaxis for use in rock mechanics with such applications:
  - Create a non-linear soil model for deep applications
  - Allow for manual override of the default meshing algorithms to allow for better application to deep subsurface problems
  - Do research on how the static friction angle changes to the dynamic friction angle so dynamic modelling would be possible
- Run simulations in a model that uses a non-linear soil model and compare the results.
- Perform simulations on non-sealing, intra-reservoir faults to gain better insights on these alternative scenarios.
- Test the software with case-studies. This could give a better view on how realistic the model is and what deviations are created by the simplifications and assumptions.
- Perform, more research into the correct measuring and extraction of values rock and fault properties so that the model can be built with the correct material properties and the analytical approach can be used correctly. In the case of prediction and mitigation of seismicity connected to fault reactivation the correct estimation of material properties would be absolutely necessary. For the wrong estimate can lead to a large change in the value of reactivation pressure.

# Bibliography

- [1] E.M. Anderson. The dynamics of faulting. *Transactions of the Edinburgh Geological Society*, 8(3):387–402, 1905.
- [2] B.M. Besly, S.D. Burley, and P. Turner. *The late Carboniferous 'Barren Red Bed' play of the Silver Pit area, Southern North Sea*, volume 4. Geological Society of London, 1993.
- [3] M.A. Biot. Mechanics of deformation and acoustic propagation in porous media. *Journal of Applied Physics*, 33(4):1482–1498, 1962.
- [4] S.J. Bourne, K. Maron, S.J. Oates, and G. Mueller. Monitoring reservoir deformation on land-evidence for fault re-activation from microseismic, InSAR, and GPS data. In *68th EAGE Conference and Exhibition incorporating SPE EUROPEC 2006*, 2006.
- [5] R.B.J. Brinkgreve, S. Kumarswamy, and W.M. Swolfs. Plaxis 2017 2D. Technical report, P.O. Box 572, 2600 AN Delft, Netherlands, 2017. Consists of multiple parts: General Information, Tutorials, Reference, Material Models and Scientific Manual.
- [6] J.D. Collinson. Dinantian and namurian depositional systems in the southern north sea. *Carboniferous Hydrocarbon Geology: The Southern North Sea and Surrounding Onshore Basins. Yorkshire Geological Society, Occasional Publications*, 7:35–56, 2005.
- [7] J.C. Doornenbal and H.J.M. Pagnier. Geological atlas of the subsurface of The Netherlands - onshore. *Netherlands Institute of Applied Geoscience TNO*, 2004.
- [8] G. Eason, B. Noble, and I.N. Sneddon. On certain integrals of Lipschitz-Hankel type involving products of Bessel functions. *Philosophical Transactions of the Royal Society of London A: Mathematical, Physical and Engineering Sciences*, 247(935):529–551, 1955.
- [9] R.M.H.E. Van Eijs, F.M.M. Mulders, M. Nepveu, C.J. Kenter, and B.C. Scheffers. Correlation between hydrocarbon reservoir properties and induced seismicity in The Netherlands. *Engineering Geology*, 84(3–4):99 – 111, 2006.
- [10] E.A. Eissa and A. Kazi. Relation between static and dynamic young's moduli of rocks. *Elsevier*, 25(6): 479–482, 1988.
- [11] E. Fjær, R.M. Holt, P. Horsrud, A.M. Raaen, and R. Risnes. *Petroleum Related Rock Mechanics, No. 53. Amsterdam, The Netherlands: Developments in Petroleum Science*. Elsevier, 2008.
- [12] Baker RDS for NAM. Dynamic geomechanical modelling to assess and minimize the risk for fault slip during reservoir depletion of the Groningen field: 1D geomechanical model (confidential report). Technical report, NAM; project reference: NAM0001, January 2014.
- [13] J. Geertsma. Land subsidence above compacting oil and gas reservoirs. *Journal of Petroleum Technology*, 25(06):734–744, 1973.
- [14] J. Geertsma and G. Van Opstal. A numerical technique for predicting subsidence above compacting reservoirs, based on the nucleus of strain concept. *Verhandelingen Kon. Ned. Geol. Mijnbouwk. Gen*, 28(s 63):78, 1973.
- [15] Schlumberger Oilfield Glossary. Leakoff test, October 2017. URL [http://www.glossary.oilfield.slb.com/Terms/1/leakoff\\_test.aspx](http://www.glossary.oilfield.slb.com/Terms/1/leakoff_test.aspx).
- [16] J. R. Grasso. Mechanics of seismic instabilities induced by the recovery of hydrocarbons. *Pure and applied geophysics*, 139(3):507–534, September 1992.

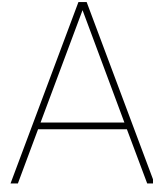
- [17] W. Hazel. On the impact of reservoir overburden heterogeneity on subsidence modelling. Master's thesis, Delft University of Technology, 2017. URL <https://repository.tudelft.nl/islandora/object/uuid%3Aabbeaa1ae-c796-49d5-a840-3e673e870a02?collection=education>.
- [18] M.H.H. Hettema. Mechanics of fault reactivation in depleting reservoirs: Initiation pressure (state of knowledge 27.10.2017). *Draft paper, to be submitted to: Rock Mechanics and Rock Engineering*, 2018. EBN B.V., <http://ebnecm/OTCS/llisapi.dll?func=ll&objaction=overview&objid=6124128>.
- [19] M.H.H. Hettema, P.M.T.M. Schutjens, B.J.M. Verboom, and H.J. Gussinklo. Production-induced compaction of a sandstone reservoir: the strong influence of stress path. *SPE Reservoir Evaluation & Engineering*, 3(04):342–347, 2000.
- [20] Colorado Plateau Geosystems Inc. Deep Time Maps - Paleogeography Europe series, 2011. <http://deeptimemaps.com/>.
- [21] H. Kombrink. *The Carboniferous of The Netherlands and surrounding areas; a basin analysis*. PhD thesis, Utrecht University, 2008.
- [22] M. Kortekaas and B. Jaarsma. Improved definition of faults in the Groningen field using seismic attributes. *Netherlands Journal of Geosciences*, 96(5):71–85, 2017.
- [23] S.P. Lele, J.L. Garzon, S.Y. Hsu, N.L. DeDontney, K.H. Searles, and P.F. Sanz. Groningen 2015 geomechanical analysis. Technical report, NAM, 2015.
- [24] G. Mavko, T. Mukerji, and J. Dvorkin. *The rock physics handbook: Tools for seismic analysis of porous media*. Cambridge university press, 2009.
- [25] E. Mechelse. The in-situ stress field in The Netherlands: Regional trends, local deviations and an analysis of the stress regimes in the north-east of The Netherlands. Master's thesis, Delft University of Technology, 2017. URL <https://repository.tudelft.nl/islandora/object/uuid%3Ab77fc7ef-c316-424f-928d-877947e9ef03?collection=education>.
- [26] I. Moeck, G. Kwiatek, and G. Zimmermann. Slip tendency analysis, fault reactivation potential and induced seismicity in a deep geothermal reservoir. *Journal of Structural Geology*, 31(10):1174–1182, 2009.
- [27] N. Morita, D.L. Whitfill, O. Nygaard, and A. Bale. A quick method to determine subsidence, reservoir compaction, and in-situ stress induced by reservoir depletion. *Journal of petroleum technology*, 41(01):71–79, 1989.
- [28] F.M.M. Mulders. *Modelling of stress development and fault slip in and around a producing gas reservoir*. PhD thesis, Delft University of Technology, 2003. URL <http://repository.tudelft.nl/islandora/object/uuid:be742135-10d7-4d69-bdee-f808b5926065?collection=research>.
- [29] P.K. Nacht, M. De Oliveira, D.M. Roehl, and A.M. Costa. Investigation of geological fault reactivation and opening. *Mecánica Computacional, Buenos Aires, Argentina*, pages 15–18, 2010.
- [30] A.C.G. Nagelhout and J.P.A. Roest. Investigating fault slip in a model of an underground gas storage facility. *International Journal of Rock Mechanics and Mining Sciences*, 34(3-4):212–e1, 1997.
- [31] NAM. Technical addendum to the Winningsplan Groningen 2013: Subsidence induced earthquakes and seismic hazard analysis in the Groningen field. Technical report, NAM, November 2013.
- [32] International Commission on Stratigraphy. International chronostratigraphic chart, 2016. <http://www.stratigraphy.org/index.php/ics-chart-timescale>.
- [33] B. Orlic and B.B.T. Wassing. A study of stress change and fault slip in producing gas reservoirs overlain by elastic and viscoelastic caprocks. *Rock Mechanics and Rock Engineering*, 46(3):421–435, 2013.
- [34] B. Orlic, B.B.T. Wassing, and C.R. Geel. Field scale geomechanical modeling for prediction of fault stability during underground gas storage operations in a depleted gas field in the netherlands in 47th us rock mechanics/geomechanics symposium. *American Rock Mechanics Association*, 2013.

- [35] J.A. Plant, A. Whittaker, A. Demetriades, B. De Vivo, and J. Lexa. The geological and tectonic framework of Europe. *Geochemical Atlas of Europe*, 1, 2003.
- [36] J.P.A. Roest and W. Kuilman. Geomechanical analysis of small earthquakes at the Eleveld gas reservoir. *Society of Petroleum Engineers*, 1994.
- [37] C. H. Scholz. *The mechanics of earthquakes and faulting*. Cambridge university press, 2002.
- [38] P. Segall. Earthquakes triggered by fluid extraction. *Geology*, 17(10):942, 1989.
- [39] J.C.M. Taylor. *Upper Permian—Zechstein in Petroleum Geology of the North Sea*, pages 174–211. Blackwell Science Ltd, 2009.
- [40] P. Tempone, E. Fjær, and M. Landrø. Improved solution of displacements due to a compacting reservoir over a rigid basement. *Applied Mathematical Modelling*, 34(11):3352 – 3362, 2010.
- [41] TNO-NITG. Geological atlas of the subsurface of the netherlands: Explanation to map sheet 3 rot-tumeroog - groningen. *Geological Survey of the Netherlands*, 1995.
- [42] J.M. Van Buggenum and D.G. den Hartog Jager. Silesian. *Geology of The Netherlands. Royal Netherlands Academy of Arts and Sciences (Amsterdam)*, pages 43–62, 2007.
- [43] P.A.J. van den Bogert. Impact of various modelling options on the onset of fault slip response using 2-dimensional finite-element modelling, restricted report no. sr.15.11455,. Technical report, Shell Global Solutions International B.V., Rijswijk, 2015.
- [44] G. Van Opstal. The effect of base-rock rigidity on subsidence due to reservoir compaction. *Proc. 3rd Congr. Int. Soc. Rock Mech*, 2:1102–1111, 1974.
- [45] J.D. Van Wees, B. Orlic, R.M.H.E. Van Eijs, W. Zijl, P. Jongerius, G.J. Schreppers, M. Hendriks, and T. Cornu. Integrated 3D geomechanical modelling for deep subsurface deformation: a case study of tectonic and human-induced deformation in the eastern Netherlands. *Geological Society, London, Special Publications*, 212(1):313–328, 2003.
- [46] B.B.T. Wassing, L. Buijze, and B. Orlic. Modelling of fault reactivation and fault slip in producing gas fields using a slip-weakening friction law in 50th us rock mechanics/geomechanics symposium. *American Rock Mechanics Association*, 2016.
- [47] J.P. Watt, G.F. Davies, and R.J. O’Connell. The elastic properties of composite materials. *Reviews of Geophysics*, 14(4):541–563, 1976.
- [48] J.D. Van Wees, L. Buijze, K. Van Thienen-Visser, M. Nepveu, B.B.T. Wassing, B. Orlic, and P.A. Fokker. Geomechanics response and induced seismicity during gas field depletion in The Netherlands. *Geothermics*, 52(Supplement C):206 – 219, 2014. Analysis of Induced Seismicity in Geothermal Operations.
- [49] P.A. Ziegler and Shell International Petroleum Company ltd. *Geological Atlas of Western and Central Europe*. Number v. 1 in Geological Atlas of Western and Central Europe. Shell Internationale Petroleum Maatschappij B.V., 1990.
- [50] M.D. Zoback. *Reservoir geomechanics*. Cambridge University Press, 2010.



# Appendices





# Appendix

## A.1. Additions to Chapter 2

**Table 2.1.1** Relationships among elastic constants in an isotropic material (after Birch, 1961).

$K$	$E$	$\lambda$	$\nu$	$M$	$\mu$
$\lambda + 2\mu/3$	$\mu \frac{3\lambda+2\mu}{\lambda+\mu}$	—	$\frac{\lambda}{2(\lambda+\mu)}$	$\lambda + 2\mu$	—
—	$9K \frac{K-\lambda}{3K-\lambda}$	—	$\frac{\lambda}{3K-\lambda}$	$3K - 2\lambda$	$3(K - \lambda)/2$
—	$\frac{9K\mu}{3K+\mu}$	$K - 2\mu/3$	$\frac{3K-2\mu}{2(3K+\mu)}$	$K + 4\mu/3$	—
$\frac{E\mu}{3(3\mu-E)}$	—	$\mu \frac{E-2\mu}{(3\mu-E)}$	$E/(2\mu) - 1$	$\mu \frac{4\mu-E}{3\mu-E}$	—
—	—	$3K \frac{3K-E}{9K-E}$	$\frac{3K-E}{6K}$	$3K \frac{3K+E}{9K-E}$	$\frac{3KE}{9K-E}$
$\lambda \frac{1+\nu}{3\nu}$	$\lambda \frac{(1+\nu)(1-2\nu)}{\nu}$	—	—	$\lambda \frac{1-\nu}{\nu}$	$\lambda \frac{1-2\nu}{2\nu}$
$\mu \frac{2(1+\nu)}{3(1-2\nu)}$	$2\mu(1 + \nu)$	$\mu \frac{2\nu}{1-2\nu}$	—	$\mu \frac{2-2\nu}{1-2\nu}$	—
—	$3K(1 - 2\nu)$	$3K \frac{\nu}{1+\nu}$	—	$3K \frac{1-\nu}{1+\nu}$	$3K \frac{1-2\nu}{2+2\nu}$
$\frac{E}{3(1-2\nu)}$	—	$\frac{E\nu}{(1+\nu)(1-2\nu)}$	—	$\frac{E(1-\nu)}{(1+\nu)(1-2\nu)}$	$\frac{E}{2+2\nu}$
$M - \frac{4}{3}\mu$	—	$M - 2\mu$	$\frac{M-2\mu}{2(M-\mu)}$	—	—

Figure A.1: Relationships among elastic constants in isotropic materials by Mavko et al. (2009)

### A.2. Additions to Chapter 3

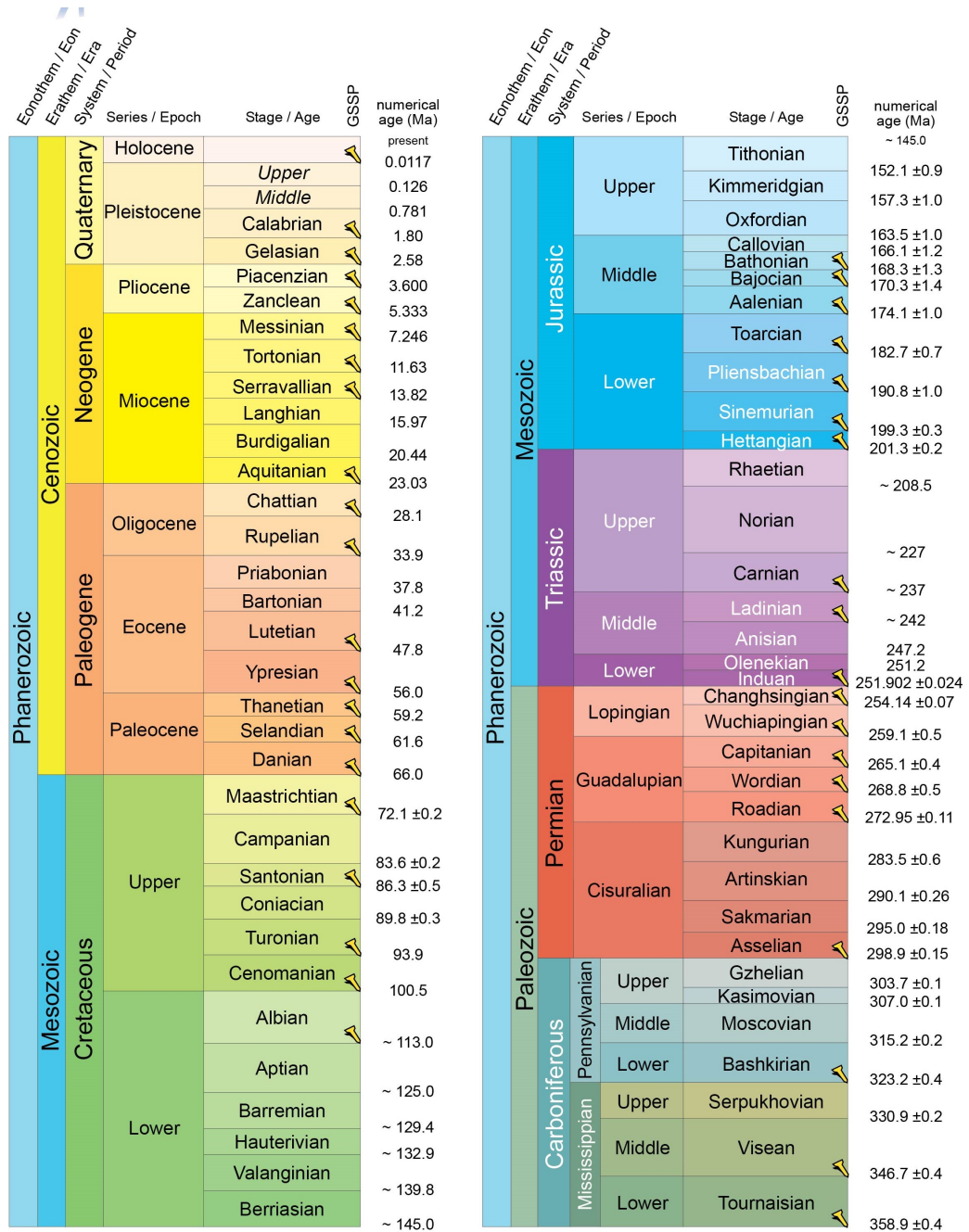
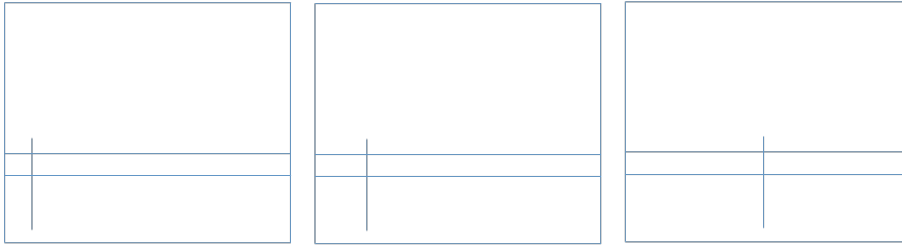


Figure A.2: Chronostratigraphic chart by on Stratigraphy

### A.3. Additions to Chapter 4

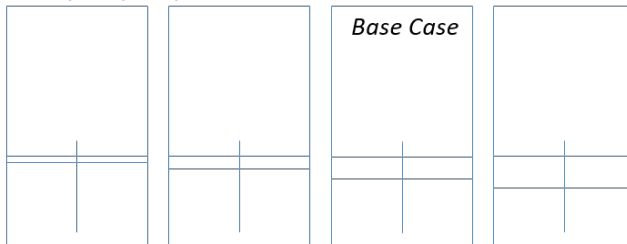
Radius:

$R = 500, 1000, 3000m$



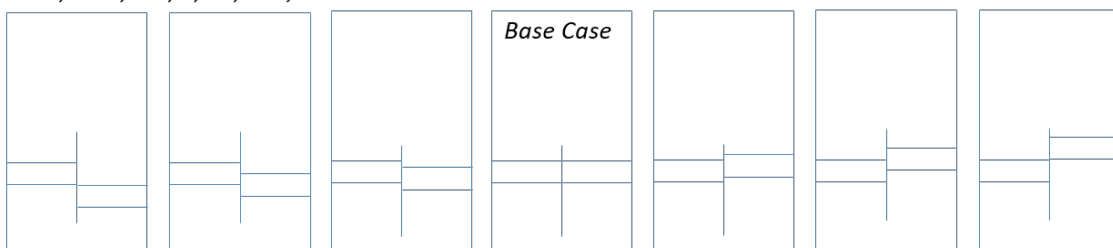
Thickness:

$h = 50, 100, 200, 300$



Throw:

$t = -h, -100, -30, 0, 30, 100, h$



Angle:

$\beta = 60, 79, 90, 101, 120$

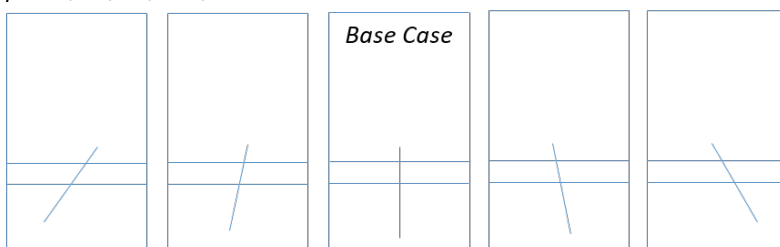


Figure A.3: Schematics of all varied geometries used in the sensitivity study.

First, a model so large (figure A.4) is built that the boundaries should have no influence on the movement within the model and especially to assess the influence range of horizontal displacement  $u_x$ . This way the model can be approximated by a plane strain model which allows for only vertical movement along  $x_{min}$  and  $x_{max}$ , a fixed boundary at  $y_{min}$  and a free boundary at  $y_{max}$  (surface). In the figure the reservoir section to the left of the fault is depleted from  $p_{in} = 35MPa$  to  $10MPa$  whereas on the right it is left at  $p_{in}$ . In the zoomed-in section it can be seen that the influence distance lies well between  $x = 30$  and  $60km$ . Outside that range the deformation is zero.

So preferably, a model of these dimensions should be run. Here, however, the limits of the software are reached. While meshing a numerical width parameter, the virtual interface thickness (VIT), is given to the interface. The VIT is directly linked to the target element dimensions  $l_e$  generated while meshing. The element

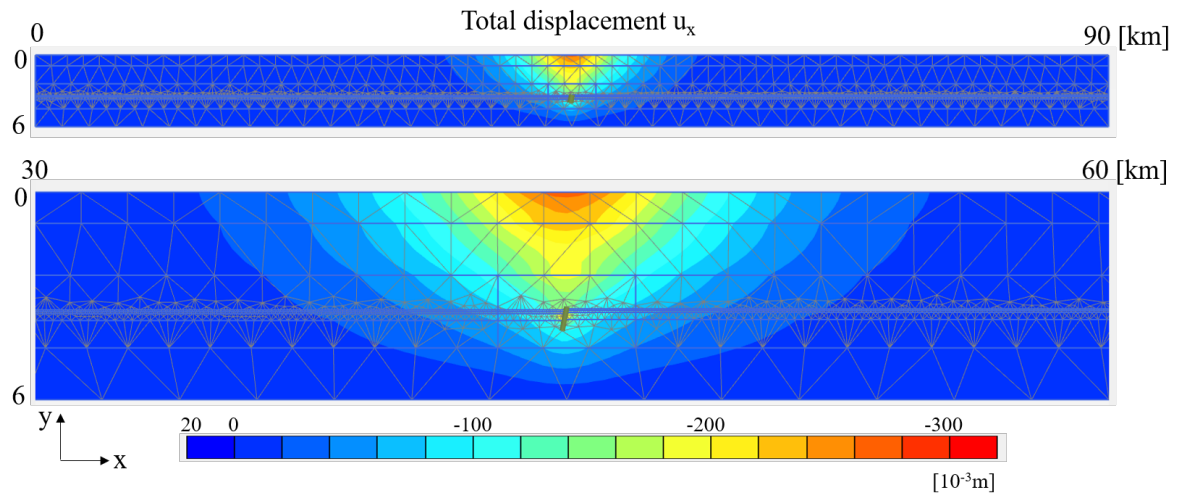


Figure A.4: Model with "infinite" boundaries and zoomed-in section to assess the influence range of horizontal displacement around a depleting reservoir.

size is again linked to the relative element size factor  $r_e$  and the general dimensions of the model as follows:

$$I_e = r_e * 0.06 * \sqrt{(x_{max} - x_{min})^2 + (y_{max} - y_{min})^2} \quad (\text{A.1})$$

The VIT is then  $I_e * \text{VIT-factor}$  with the VIT-factor set to its smallest value 0.01.

The VIT has a large influence on the elastic and plastic behaviour of a fault and since it is linked to the general model dimensions it has values of up to multiple meters thick given the model dimensions in figure A.4. The only way to reduce the VIT in Plaxis is to reduce the size of the model. This, however, might cause boundary effects to influence the output of the simulations.

To check for any such effects which might have influence on fault reactivation a smaller model was run ( $x_{max} = 6km$  instead of  $10km$ , listed in table A.1) with the same VIT to check for differences. Figure A.5b shows that there is no difference between these axisymmetrical models.

Analysis of multiple axisymmetrical simulations in which the radial extent was varied from  $10km - 6km$  shows that large values of the VIT (which occurs for larger models) reduces plasticity of the fault significantly and thus failure cannot be predicted accurately. Figure A.5a shows the relative shear stress on the fault for a model with large model dimensions (blue line) and for one with smaller model dimensions (yellow line). It shows that when the VIT is smaller, so for the model with the smaller radius, plasticity occurs quicker. From this it can be concluded that the VIT does definitely have an effect and that a smaller value will predict failure quicker.

Table A.1: Various model dimension to test influence of VIT.

$x_{max}$ [km]	Mesh Nr.	Rel. element size	Element Dimensions [m]	VIT [m]
10 (fault at 3)	0.03	0.5	349.857	3.49
10 (fault at 3)	0.01998	0.333	233.005	2.33
6 (fault at 3)	0.02748	0.458	233.005	2.33
6 (fault at 3)	0.01998	0.333	169.536	1.69
3 (fault at 1.5)	0.03	0.5	150	1.5
3 (fault at 1.5)	0.01998	0.333	99.9	1

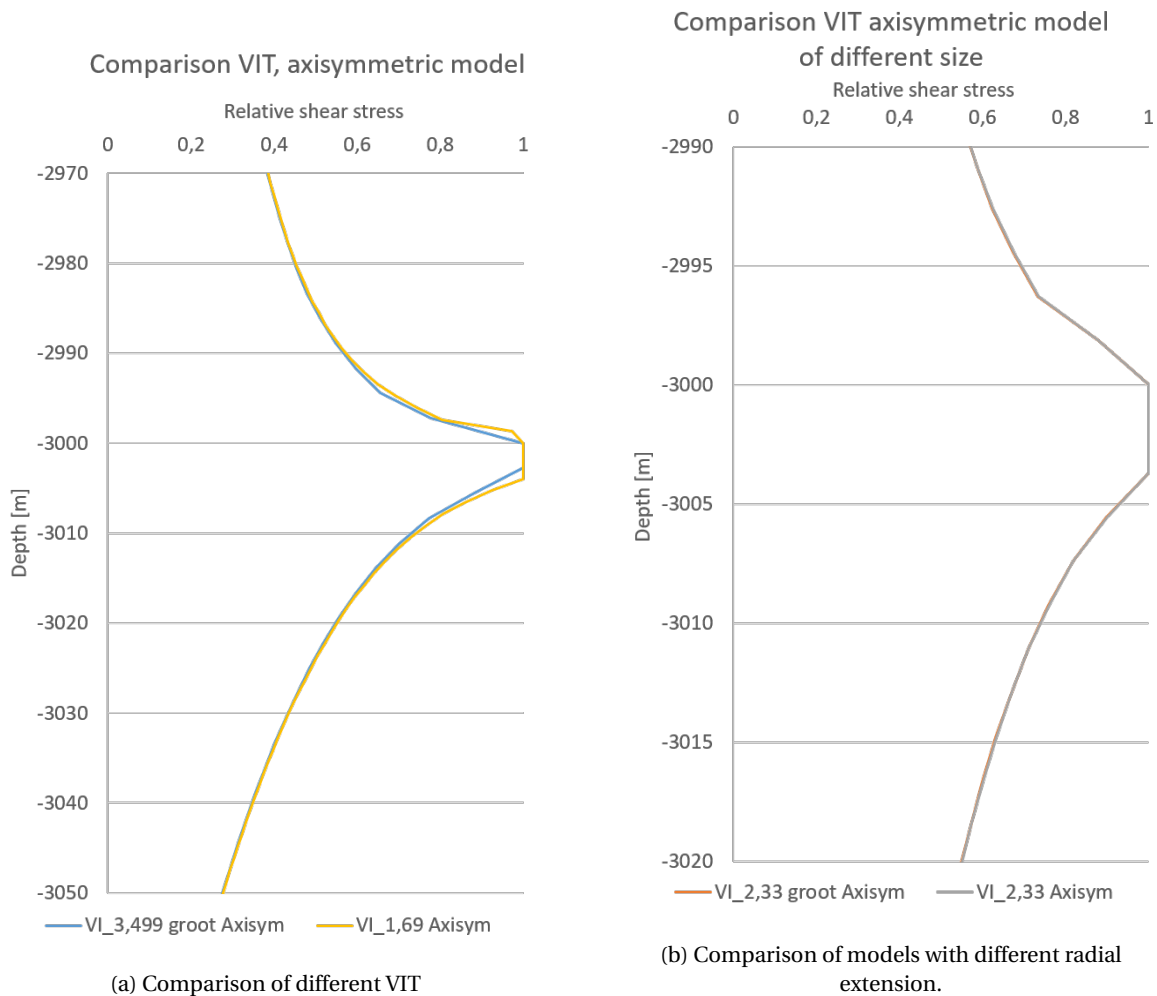


Figure A.5: Comparison of different virtual interface thicknesses for models of different extension. This allows for the checking of the influence of boundary effects.

Because the models looked into so far are all axisymmetrical, as this is easier when comparing to the analytical approach, it is not possible to reduce the size of the model much more than a  $x_{max}$  of around  $6km$ . As with this  $x_{max}$  the VIT is still  $1.69m$ , it is necessary to check fault failure behaviour with an even smaller VIT. As the size of the VIT is linked to the global model size the model dimension needs to be reduced. In order for the model to take on the wanted dimensions it needs to be designed as plane strain.

Other research projects (Wassing et al. (2016)) have used plane strain models as it is known that such models represent reality very well. To investigate which is best, a few tests were performed, comparing the results of an axisymmetrical model with those of a plane strain model. To see the differences between axisymmetric and plane strain, two models were run with the same dimensions for each model design. The results show that there is little difference between the results for each design (figure A.6).

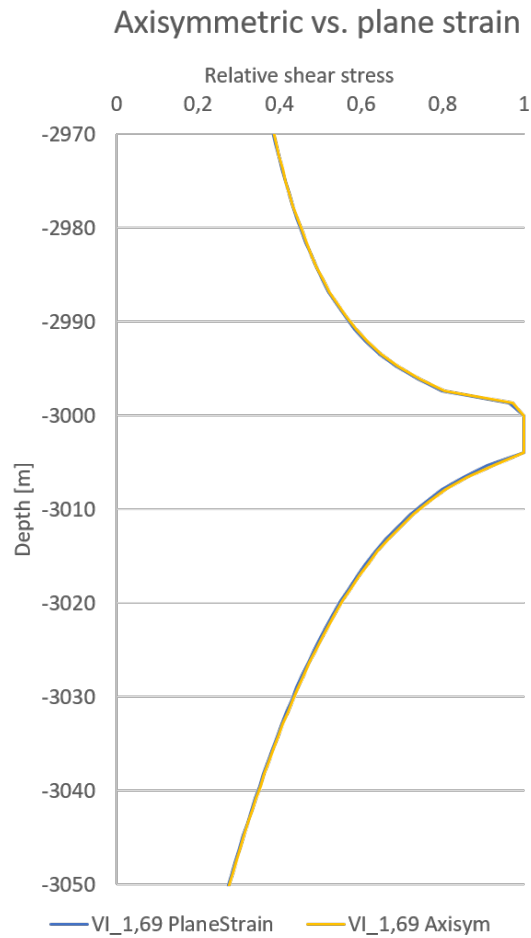


Figure A.6: Comparison of an axisymmetrical model with plane strain model.

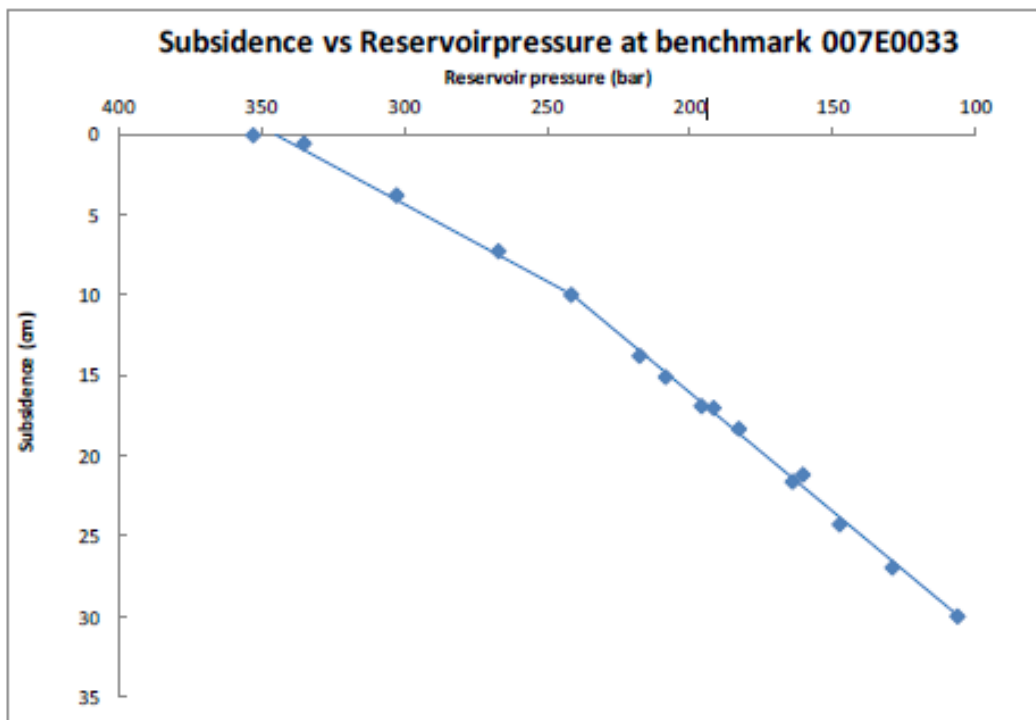


Figure 4.9 Comparison of subsidence measurements (blue dots) with reservoir pressure for Benchmark 007E0033. The lines show a bi-linear compaction when starting linear compaction for start and one from the end.

Figure A.7: Measured subsidence for reservoir pressure in the Groningen gas field after [31]

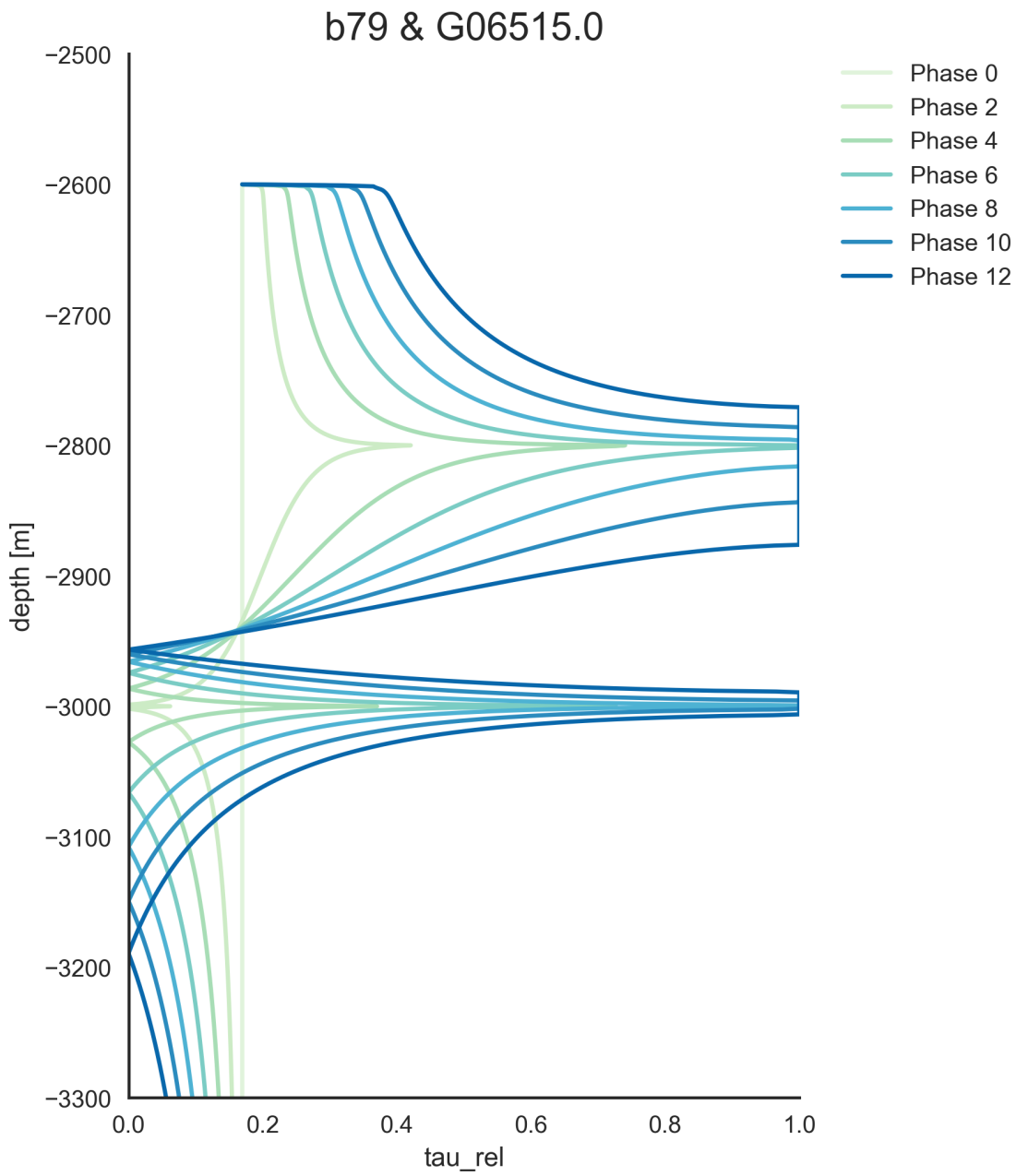
**A.4. Additions to Chapter 5**

Figure A.8: Relative shear stress on a fault with angle of  $79^\circ$ . It can be seen that the point of zero shear stress is in the lower half of the reservoir.